



Veröffentlichungen

der DGK

Ausschuss Geodäsie der Bayerischen Akademie der Wissenschaften

Reihe C

Dissertationen

Heft Nr. 822

Sujata Goswami

**Understanding the sensor noise in the GRACE range-rate
observations by analyzing their residuals**

München 2018

Verlag der Bayerischen Akademie der Wissenschaften

ISSN 0065-5325

ISBN 978-3-7696-5234-5



Veröffentlichungen

der DGK

Ausschuss Geodäsie der Bayerischen Akademie der Wissenschaften

Reihe C

Dissertationen

Heft Nr. 822

Understanding the sensor noise in the GRACE range-rate observations by analyzing their residuals

Von der Fakultät für Bauingenieurwesen und Geodäsie

der Gottfried Wilhelm Leibniz Universität Hannover

zur Erlangung des Grades

Doktor-Ingenieur (Dr.-Ing.)

genehmigte Dissertation

Vorgelegt von

M.Tech. Sujata Goswami

Geboren am 16.07.1990 in Modinagar, India

München 2018

Verlag der Bayerischen Akademie der Wissenschaften

ISSN 0065-5325

ISBN 978-3-7696-5234-5

Adresse der DGK:



Ausschuss Geodäsie der Bayerischen Akademie der Wissenschaften (DGK)

Alfons-Goppel-Straße 11 • D – 80 539 München
Telefon +49 – 331 – 288 1685 • Telefax +49 – 331 – 288 1759
E-Mail post@dgk.badw.de • <http://www.dgk.badw.de>

Prüfungskommission:

Vorsitzender: Prof. Dr.-Ing. Udo Nackenhorst

Referent: Prof. Dr.-Ing. Jürgen Müller

Korreferenten: Prof. Dr.-Ing. Torsten Mayer-Gürr
Prof. Dr.-Ing. Christian Heipke

Tag der mündlichen Prüfung: 12.07.2018

© 2018 Bayerische Akademie der Wissenschaften, München

Alle Rechte vorbehalten. Ohne Genehmigung der Herausgeber ist es auch nicht gestattet,
die Veröffentlichung oder Teile daraus auf photomechanischem Wege (Photokopie, Mikrokopie) zu vervielfältigen

The Gravity Recovery and Climate Experiment (GRACE) mission has successfully used the inter-satellite ranging technology to determine the time-variable gravity field of the Earth. After staying in orbit for more than 15 years, the mission has been decommissioned in October 2017. However, the requirements to meet the GRACE baseline accuracy have not yet been achieved due to the presence of various error sources. One of the major sources partially is mis-modeled errors of the sensor observations. Such errors can be seen in the post-fit range-rate residuals. Our goal is to understand the errors in the range-rate observations and analyze the corresponding residuals to identify mis-modeled sensor errors. Specifically, an analysis of the attitude, ranging and accelerometry errors in the GRACE satellite observations and in the corresponding range-rate residuals is presented. By analyzing the range-rate residuals the knowledge of systematic effects of the sensors affecting the measurements are gained.

In this work, it is shown that the range-rate residuals are highly dominated by high frequency (>20 mHz) system noise. In particular, phase errors of the K-band frequencies of both spacecraft lead to the noise in the high frequencies of the range-rate residuals. The error contribution due to such effects may reach up to 30 % of the total error. Further, while analyzing the range-rate residuals, it has been found that the highest attitude error contributors in the range-rate observations are the range-rate antenna phase center offset corrections. The contribution of those attitude errors can be as high as 25 % of the total error. The analysis of low frequency residuals (≈ 1 CPR to 30 CPR) shows the dominance of instrument temperature fluctuations, satellite maneuvers dependent errors and errors due to spacecraft shadow transitions propagated via the accelerometers. Range-rate residuals in these frequencies also contain a considerable amount of errors of the geophysical background models and of the attitude. As the range-rate residuals are dominated by systematic errors from the sensors, there is still a scope of improvement in the modeling of observation noise and in the instrument re-calibration approaches in order to minimize the error contribution. A similar strategy will be helpful for the analysis of the Laser Ranging Instrument and K-Band Ranging residuals of the recently launched GRACE-Follow On mission.

Zusammenfassung

Die satellitenmission “Gravity Recovery and Climate Experiment” (GRACE) wurde erfolgreich zur Bestimmung des zeitlich variablen Erdschwerefeldes mittels Satelliten-Abstandsmessung verwendet. Die Mission wurde im Oktober 2017 beendet, nachdem die Satelliten mehr als 15 Jahre im Orbit waren. Dennoch konnte die vorgesehene Genauigkeit aufgrund verschiedener Fehlerquellen bisher nicht erreicht werden. Eine der wichtigsten Fehlerquellen sind fehlerhafte Modelle der Messdaten verschiedener Sensoren. Diese Fehler sind sichtbar in den post-fit Residuen der Abstandsänderungsraten (“range-rates”). Unser Ziel ist es, die Fehler in diesen range-rate Messungen zu verstehen und die entsprechenden Residuen zu analysieren, um Fehler in den Sensor-Modellen zu identifizieren. Insbesondere präsentieren wir eine Analyse der Fehler im Zusammenhang mit der Ausrichtung der Satelliten, der Abstands- sowie der Akzelerometermessungen, sowohl in den Messdaten als auch in den entsprechenden Residuen. Durch die Analyse der range-rate Residuen kann Information über systematische Effekte der Sensoren, welche die Messungen beeinflussen, gewonnen werden.

In dieser Arbeit wird gezeigt, dass die range-rate Residuen dominiert werden von hochfrequentem (> 20 mHz) Systemrauschen. Insbesondere wird das Rauschen in hohen Frequenzen durch Phasenrauschen des K-Band Instruments (auf beiden Satelliten) verursacht. Diese Art von Fehler macht bis zu 30% des Gesamtfehlers aus. Ferner wurde festgestellt, dass der größte Teil des Fehlers in den range-rate Residuen, der von der Ausrichtung der Satelliten abhängt, durch die Korrekturterme des Phasenzentrums (“antenna offset corrections”) verursacht wird. Dieser Fehler kann bis zu 25% des Gesamtfehlers aus. Die Analyse der Residuen im Niederfrequenzbereich (etwa 1 bis 30 CPR) zeigt drei dominierende Fehler, verursacht durch Temperaturschwankungen, Satellitenmanöver und Licht-Schatten-Durchgänge via Akzelerometermessungen. Die Residuen enthalten außerdem Fehler in den geophysikalischen Hintergrundmodellen sowie von der Ausrichtung der Satelliten abhängige Fehler. Da die Residuen von systematischen Fehlern der Sensoren dominiert werden, gibt es Verbesserungsmöglichkeiten durch bessere Modellierung des Instrumentenrauschens und durch erweiterte Ansätze zur Rekalibrierung der Instrumente. Eine ähnliche Strategie wird auch hilfreich sein für die Analyse der Laser Ranging und K-band Ranging Residuen der GRACE-Follow On mission, die im Mai 2018 gestartet wurde.

Acknowledgements

I would like to thank Prof. Jakob Flury for giving me the opportunity to work on this topic. I am highly thankful to Prof. Torsten Mayer-Gürr not only for being my second supervisor but also for providing me the access to necessary computational resources due to which my work pace improved tremendously. I am also thankful to Dr. Matthias Weigelt for agreeing to be my ancillary supervisor and helping me from time to time in my research. He was also a very nice friend during my Ph.D. whose moral support was of great help.

Dear Balaji and Jayani, I could not have made it without both of you. You two were a big moral support during my good as well as bad times in Hannover. Balaji, I thank you so much for being an excellent collaborator. I found your doors always open for discussions. Those discussions helped me a lot in improving me as a scientist and my work, both.

Dear Tamara, this work would not have had come to this end without you. Discussions with you helped me alot in kicking off my work. Your help in patiently explaining the complex data characteristics in an easy way were of big help. Not only just scientific help, you were also a great moral supporter during my tough times in Ph.D. A big thanks to all of you.

I am highly thankful to Prof. Karsten Danzmann, Fumiko Kawazoe, Prof. Jürgen Müller and all the IfE members for being so generous to me in the time of need. I could not see myself writing this draft without the support I got from all of them. Although, Hannover had been my main work place, I was also visiting the group of Prof. Torsten Mayer-Gürr in TU Graz time to time. I owe a big thanks to the Graz team - Matthias Ellmer, Beate Klinger, Saniya Behzadpour, Andreas Kvas and Norbert Zehentner for being such nice hosts at TU Graz and always patient in replying to my emails.

In the last but always first, I am grateful to God who gave me such lovely and supportive parents and siblings. It was just so lucky to have my partner Saurabh by my side all the time during the Ph.D. He was always my pillar of strength during the tough research times.

Hannover, August 2018

Sujata Goswami

Contents

Abstract	1
Zusammenfassung	3
Acknowledgements	5
I <i>Introduction</i>	11
1 Introduction	13
1.1 State of the art	14
1.2 Objectives	21
2 Gravity Recovery And Climate Experiment Mission	23
2.1 Introduction	23
2.2 Applications	23
2.3 The GRACE observation system	24
2.4 Global gravity field parameter estimation from GRACE observations	28
2.4.1 Gravity field representation	28
2.4.2 Gravity field modeling	28
2.5 Analysis kit used for studying the residuals	35
2.5.1 Degree amplitudes	35
2.5.2 Power Spectral Density (PSD)	35
2.5.3 Time-series analysis	36
2.5.4 Argument of latitude	37
2.5.5 Satellite ground tracks	39
II <i>Analysis of K-band range-rate residuals</i>	41
3 Inter-satellite pointing errors in range-rate residuals	43
3.1 What is inter-satellite pointing?	43
3.2 GRACE attitude - its characteristics and errors	46

3.3	Attitude error propagation into the range-rate observations	54
3.3.1	Error propagation via antenna offset corrections	54
3.3.2	Error propagation via linear accelerations	58
3.4	Post-fit residual analysis with focus on attitude errors	60
3.5	How do attitude errors affect gravity field solutions?	65
3.5.1	Simulation scenario	65
3.6	Summary	71
4	Inter-satellite ranging errors in range-rate residuals	73
4.1	Inter-satellite ranging	73
4.2	Inter-satellite ranging errors	75
4.3	Post-fit residual analysis with focus on ranging errors	78
4.4	Impact of high-frequency errors on the gravity field solutions	89
4.5	Summary	92
5	Accelerometer errors in range-rate residuals	93
5.1	GRACE accelerometer	93
5.2	Errors and characteristics of GRACE accelerometer observations	94
5.3	Range-rate residual analysis with focus on accelerometer errors	104
5.4	Summary	117
III	<i>Conclusions</i>	121
6	Conclusions	123
	Appendices	127
A	Inter-satellite pointing angles and the satellite panels	129
A.1	Computation of GRACE inter-satellite pointing angles	129
A.2	Satellite panels	132
	Bibliography	144

Curriculum Vitae	145
------------------	-----

I

Introduction

The study of features of the gravity field of the Earth has always been one of the primary interests of geodesy. The Earth's gravity field and changes in it reflect mass changes inside and on the surface of the Earth.

As an example, Earth's gravity measurements are used to get information about the shape of the geoid. Variations of the gravity field reflect continental water storage changes, ice mass balance changes, glacial isostatic adjustment and sea level changes. All these phenomena influence the human life on the Earth, directly or indirectly, and their accurate knowledge depends on the accuracy of the gravity measurements. Therefore, precise knowledge of the gravity field is not only necessary for geodetic science but also an important requirement for climate science.

In the beginning of the 20th century, gravity measurements were carried out on ground using instruments called *gravimeters*. These instruments were capable of measuring gravity changes as point observations. A major limitation of the gravimeters was and still is, that they could not be used over a large region or on a global scale. This goal was first accomplished later in the 20th century with the use of satellites. Use of artificial satellites for geodetic purposes was introduced during 1950s after the launch of Sputnik in 1957 and Explorer in 1958. These missions allowed the successful determination of the flattening of the Earth, e.g. Heiskanen and Moritz (1967).

The first dedicated geodetic satellite was ANNA-1B launched on 31 October 1962 by National Aeronautics and Space Administration (NASA) and the Department of Defense which led to an accurate determination of the very low-degree spherical harmonic coefficients of the geopotential, the general shape of the geoid. The first decade of the 21st century was dedicated to measure the Earth's gravity field with satellite missions, e.g., Satellite Laser Ranging (SLR) missions, CHAMP, GRACE and GOCE.

GFZ-1 (GeoForschungsZentrum Potsdam) is an example of satellites launched to determine the gravity field of the Earth along with the determination of its rotation and the precise position of the spacecraft. These satellites were equipped with retro-reflectors to be illuminated from the ground by the global network of the SLR system (GeoForschungsZentrum, 2018).

CHAMP (CHallenging and Minisatellite Payload) was the first dedicated and successful mission launched aiming at the measurement of the gravity field. It was based on orbit tracking and accelerometry. CHAMP was also used for magnetic field recovery and atmospheric research. The mission was launched in July 15, 2000 from Cosmodrome Plesetsk, Russia and ended on September 19, 2010.

GRACE (Gravity Recovery And Climate Experiment) was launched on March 17, 2002 from cosmodrome Plesetsk, Russia. The mission was based on orbit tracking, satellite-to-satellite tracking and precise accelerometry to measure the gravity field of the Earth. The mission consisted of twin low Earth satellites tracking each other by observing mutual distance variations which are caused by changes in the Earth's gravity field. An unprecedented accuracy of the time-variable gravity field was a remarkable achievement made by the GRACE mission (Tapley et al., 2004a). The mission has been ended in late 2017, after delivering science results for 15 years, more than 3 times of its planned lifetime.

GOCE (Gravity Field And Steady-State Ocean Circulation Explorer) was launched on March 17, 2009 from Plesetsk, Russia and ended on November 11, 2013. The mission was dedicated to measuring the global static gravity field of the Earth using a highly sensitive gravity gradiometer. GOCE brought new insight in the behavior of ocean circulation. The combination of its data with altimetry missions made it possible to track geostrophic ocean currents at a better spatial resolution than ever before. Highest spatial resolution of the static field was a great achievement of the GOCE mission to realize a global geoid with 1 cm accuracy. Gravity measurements of GOCE and GRACE complemented each other very well. Data of these two missions have been combined successfully to compute a static gravity field model of the Earth up to degree and order 250 which is named as GOCOS (Pail et al., 2010). EIGEN 6C4 is another improved static gravity field model computed up to degree and order 2190 by combining data of many satellites together with terrestrial data (Förste et al., 2014).

1.1 State of the art

The GRACE mission is based on inter-satellite ranging measurements. The range (ρ_{KBR}) between the two satellites is influenced by non-gravitational forces and grav-

itational forces acting on the satellite. It is described as

$$\boldsymbol{\rho}_{\text{KBR}} = \boldsymbol{\rho}_{\text{Gravitational Forces}} + \boldsymbol{\rho}_{\text{Non-gravitational Forces}} + \boldsymbol{\epsilon}, \quad 1.1$$

where $\boldsymbol{\rho}_{\text{KBR}}$ represents the range observations from the K-Band Ranging (KBR) instrument,

$\boldsymbol{\rho}_{\text{Gravitational Forces}}$ are the measurements due to all gravitational forces,

$\boldsymbol{\rho}_{\text{Non-gravitational Forces}}$ represent measurements due to non-gravitational forces and $\boldsymbol{\epsilon}$ refers to the *errors* from all the sources.

The gravitational and non-gravitational forces include

$$\begin{aligned} \text{Gravitational Forces} &= \begin{bmatrix} \text{static gravity field} \\ \text{tides (ocean, pole) and} \\ \text{astronomical tides due to sun and moon} \\ \text{non-tidal high-frequency mass variations, etc.} \end{bmatrix}, \\ \text{Non-gravitational Forces} &= \begin{bmatrix} \text{solar radiation pressure} \\ \text{Earth infrared albedo} \\ \text{air drag, etc.} \end{bmatrix}. \end{aligned}$$

1.2

The effects of the known forces mentioned in Eq. 1.2 are reduced from the range observations to get the tiny changes caused due to the hydrological, ice and solid Earth mass variations in and on the surface of the Earth. Also, an imperfection in the knowledge of the models of the above-mentioned forces and systematic effects in the sensors remain in the range observations which limits their precision. Therefore, the reduced range-rates contain all corrections. Since these observations are the fundamental part of the entire global gravity field recovery chain, their limited precision in turn affects the precision of the estimated global gravity field parameters.

To understand these *errors* is of interest due to following reasons:

- The level of precision which was predicted by Kim (2000) before the launch of the mission has not yet been achieved. There is an offset present between the predicted baseline accuracy and the achieved level of precision (cf. top panel of Fig. 1.1). If the baseline accuracy can be reached, the time-variable signal will be obtained more precisely than the current solutions. This will certainly

15

be helpful in improving our understanding of the time-variable gravity field and in its applications.

- In order to improve the performance of current and future gravity field missions, the precision of their input observations and the approach of modeling the observations' noise certainly needs to be improved. This is possible if and only if the limiting factors in the current scenario are known.

With the goal of understanding these *errors*, various studies have been carried out in order to investigate the potential of the sensors onboard, their limitations, and the accuracy of the existing background models, even before the launch of the mission. For example, Thomas (1999) studied the potential of the microwave ranging instrument onboard the GRACE satellites and possible errors (cf. bottom panel of Fig. 1.1). The microwave ranging system uses K- and Ka-band frequencies to precisely measure the *range* and its change between the two satellites. Kim (2000) studied the expected performance of the gravity field solutions computed from GRACE, prior to its launch. Full-scale simulations were carried out with the aim of computing the expected precision of the time-variable gravity field, under the consideration of expected errors in the *range* observations. The gravity field computed from those simulations is referred to as the GRACE baseline. Today, when every data processing center computes a gravity field model from the GRACE observations, they refer their models to this baseline, shown in top panel of Fig. 1.1.

After the launch of the mission, knowing that the real GRACE gravity field solutions are not as precise as their predicted BASELINE, numerous studies were published focusing on:

- understanding the individual error sources and their contribution to the gravity field models,
- improvement of data preprocessing, data and noise modeling approaches.

A selection is listed in Table 1.1 with the description of their focus areas.

These studies certainly improved the knowledge of the noise in the range observations, data processing and modeling strategies which resulted in an improved gravity field model (reducing the differences between the BASELINE and the obtained gravity field solutions). Since the baseline has not been reached yet, the quest to

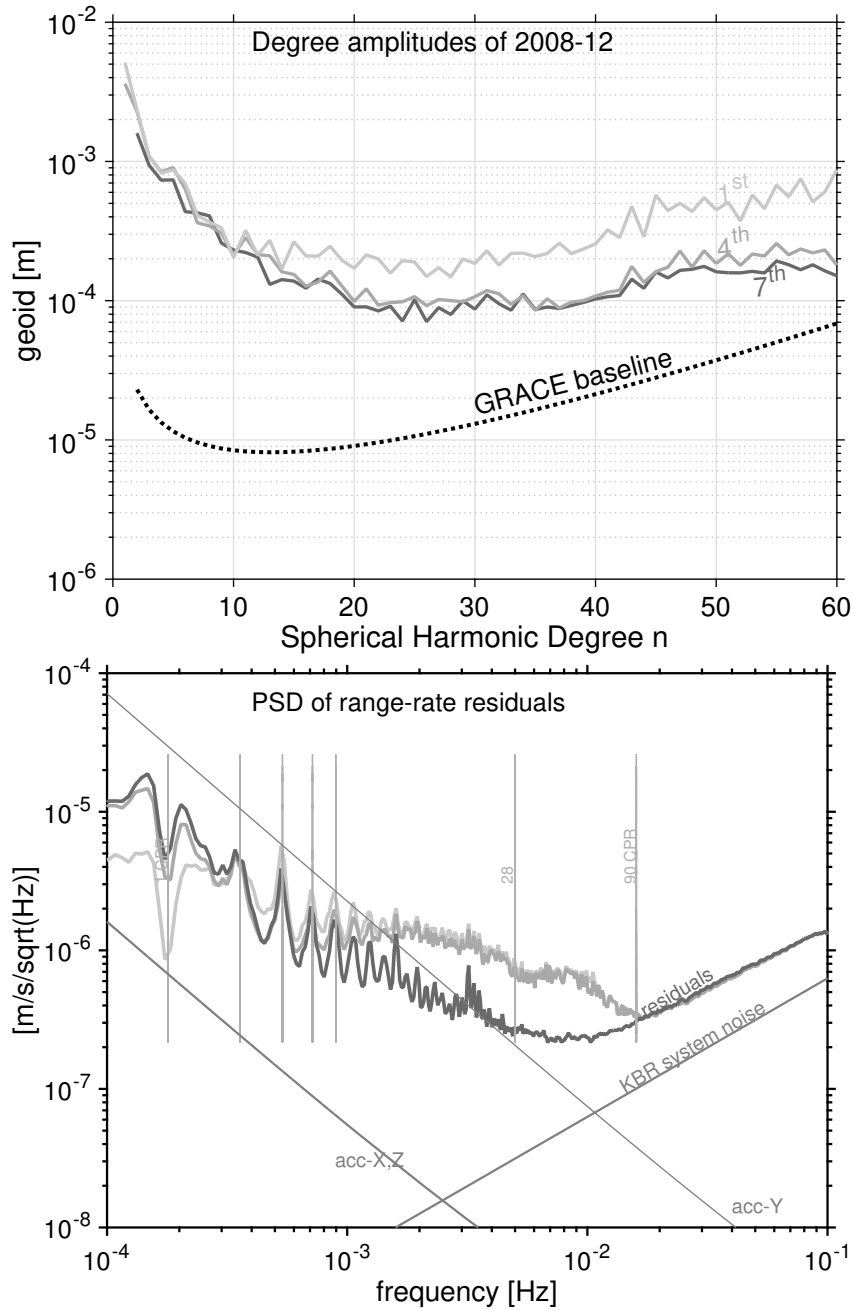


Figure 1.1: *Top panel: Status of the ITSG-2014 solutions as compared to the GRACE baseline for December 2008 are shown in terms geoid degree amplitudes. The differences (ITSG-2014) are plotted with respect to the static field GOCO 05s. The numbers 1, 4, 7 represent the status of the gravity field solutions computed in an iterative least-squares approach. Bottom panel: Power Spectral Density (PSD) of postfit range-rate residuals compared with the available sensor noise models for December 2008 at every iteration step of the iterative least-squares parameter estimation approach. CPR refers to the cycles per revolution.*

Table 1.1: *Some studies published after the launch of GRACE with focus on the errors in the gravity field solutions.*

Studies by	Research Focus
Ko (2008); Ko et al. (2012)	KBR microwave ranging system
Flury et al. (2008); Hudson (2003); Peterseim (2014); Peterseim et al. (2012)	GRACE Accelerometer
Bandikova et al. (2012); Horwath et al. (2011); Inácio et al. (2015); Ko and Eanes (2015)	Star camera, inter-satellite pointing
Ditmar et al. (2012)	Error in GRACE gravity field models
Bonin and Chambers (2011); Chambers and Bonin (2012)	Atmosphere and Ocean De-aliasing errors
Han et al. (2004); Knudsen et al. (2001)	Ocean model errors

investigate the noise in the observations is still ongoing. It is a primary objective to achieve the desired precision of the gravity field solutions. The GRACE-Follow On mission has been launched recently and similar problems might be faced by the science community due to lack of knowledge about the precision of the observations. Thus, it is an urgent requirement to achieve a better understanding of the noise behavior in the observations in order to fully exploit them to obtain precise gravity field solutions.

The global gravity field parameters are estimated in the least-squares sense where the observation set-up is as follows (Koch, 1990)

$$\mathbf{l} - \mathbf{A}\hat{\mathbf{x}} = \hat{\mathbf{e}}, \quad 1.3$$

where \mathbf{l} is the vector of the reduced range-rate observations which are computed by removing all the perturbations mentioned in Eq. 1.2 from the K-band measurements, \mathbf{A} is the design matrix, $\mathbf{A}\hat{\mathbf{x}}$ represents the vector of fitted observations obtained after estimating the parameters $\hat{\mathbf{x}}$, and $\hat{\mathbf{e}}$ refers to the residuals computed by subtracting the range-rate observations and the fitted observations. The parameter estimation approach aims to determine the parameters with the best fit to the original observations, which means, the residuals ($\hat{\mathbf{e}}$) must be minimized. Besides being small, the residuals must be random in nature. That means, they should not be predictable or

correlated with any other variable of the system of equations which would otherwise indicate an insufficiency of the modeling approach. Also, the Power Spectral Density (PSD) of the residuals ($\hat{\epsilon}$) obtained after GRACE parameter estimation shows that they are larger than the expected sensor noise level (cf. bottom panel of Fig. 1.1). The expected sensor noise level was predicted by Kim (2000) and has been plotted for the accelerometer (ACC) and the K-band ranging (KBR) instrument noise in the bottom panel of Fig. 1.1. Not only the residuals ($\hat{\epsilon}$) are large, they also contain signal characteristics such as 1 CPR (cycles per revolution) or 2 CPR signals which certainly does not represent a random noise behavior.

This work focuses on the characterisation of such behavior of the range-rate residuals. Their characterisation is important due to following reasons:

- To understand the deterministic and stochastic behavior of the range-rate residuals. The deterministic characteristics depend on other observations and can be modeled, whereas the stochastic characteristics represent the random behavior, which can not be predicted, and change randomly. Knowing the deterministic part will be helpful to implement the realistic empirical parameters to be estimated along with the global gravity field parameters. Knowledge of the stochastic part will be helpful in implementing a realistic stochastic noise model.
- The fitted range-rate residuals are used to compute the variance factor which is further used to determine the covariance matrix in the least-squares parameter estimation. The errors in the residuals propagate to the solution via covariance information applied to the observations. Therefore, minimizing the errors in the residuals will reflect an improvement in the precision of the estimated gravity field solutions. It is also shown in Fig. 1.1 where the reduced values of residuals (bottom panel) improve the gravity field solutions (top panel) in an iterative least-squares fit approach. This is only possible by gaining knowledge about the characteristics and behavior of the residuals. A similar study was presented earlier by Ditmar et al. (2006), the authors where they modeled the noise based on frequency-dependent weights of the observations and improved the precision of the gravity field solutions from the observations of CHAMP. Note that due to the non-linearity of the observation set up, large differences

are seen between the PSD of the residuals at 4th and 7th iteration in the bottom panel of Fig. 1.1.

- The analysis of the residuals of the observations serves as a quality assessment criteria which presents the quality of the parameters estimated during the least-squares fit. The residuals obtained after the least-squares fit represent an approximation of the true errors in the range-rate observations. Hence, their PSD shown in Fig. 1.1 represents an approximation of the true error and can be used to describe the precision of the estimated gravity field solutions. For example, a study by Pail (2004) presented an analysis of the spectral behavior of the gradiometer residuals to assess the quality of gravity field solutions derived in a simulation scenario like GOCE. They further emphasized the use of residual quantities to identify the outliers, and reducing the residuals by outlier removal, filtering and using those reduced residuals to re-estimate the gravity field parameters iteratively to ultimately obtain an improved gravity field model. Xianping and Yanc-Yuanxi (2005) showed an assessment of the quality of the CHAMP derived gravity field solutions by comparing the fitted residuals computed using two different approaches.

Due to the high relevance of these fitted residuals in determining and assessing the accuracy of estimated gravity field parameters, this study focuses on their detailed analysis and gives a comprehensive overview of the systematic errors present in them.

Since the estimated residuals include a portion of the errors and signal which has been partially mapped or aliased into the estimated global gravity field parameters, their analysis can provide a good picture of the errors. However, the residuals alone do not allow us to get an absolute quantification of the errors present in the gravity field solutions. As this study solely addresses the analysis of residuals of GRACE range-rate observations, an absolute error budget is not presented. However, attempts to quantify the investigated errors have been made and are presented accordingly.

As it has been shown in the bottom panel of Fig. 1.1, the range-rate residuals are one order of magnitude above the sensor noise level. This shows that the potential of the GRACE sensor data has not been fully exploited, yet. There remains room

to understand the limitations from the sensor side. This led to define the focus of the work presented in this thesis which is, *analyzing the residuals with focus on the sensor errors' contribution in them.*

1.2 Objectives

The objectives of this thesis are defined as:

- Analysis of the range-rate residuals with focus on the attitude errors. The identification of errors is helpful in improving the gravity field modeling procedure:

In the range-rate observations, the attitude errors mostly propagate via the star cameras on the GRACE satellites. In Chapter 3, the attitude errors present in the residuals due to star camera data are analyzed and discussed. Further, taking advantage of the different reprocessed datasets computed by Klinger and Mayer-Gürr (2014) and Bandikova and Flury (2014), the impact of attitude errors on the gravity field solutions are investigated.

- Analysis of the range-rate residuals with focus on the KBR instrument noise. The knowledge of KBR instrument noise is helpful in reducing those errors from the GRACE gravity field models. It is presented in Chapter 4:

Here, an analysis of the range-rate residuals is presented with focus on the spectra where the KBR instrument noise dominates. The dominating KBR system noise in the range-rate residuals has been studied in detail with the focus on possible error sources. The impact of this noise on the gravity field solutions is also discussed considering various simulation scenarios.

- Analysis of the range-rate residuals with focus on the accelerometer errors. The identified errors coming from the accelerometer are helpful in reducing them during the gravity field modeling:

In Chapter 5, systematic errors of the accelerometers which can be seen in the residuals are studied. Since the accelerometer errors in the frequency range 0.1 - 0.9 mHz are higher than in the frequency range 1 - 4 mHz, the analysis considers the two frequency bands separately. In the frequency band 1 - 4 mHz,

the errors of the geophysical background models and star camera errors overlap and are also addressed.

The objectives discussed in this work are based on the GRACE data analysis of two years, i.e. 2007 and 2008. During this time period, GRACE data benefitted from low impact of solar activity affecting the satellites and their observations (Meyer et al., 2016). Hence, it serves as a good candidate for the systematic error analysis of the residuals of the range-rate observations.

Chapter 2: Gravity Recovery And Climate Experiment Mission

2.1 Introduction

The GRACE mission was launched on 17 March 2002 from Plestes, Russia (Tapley et al., 2004a) and has been decommissioned in October 2017. It was a joint mission between NASA, United States, and DLR, Germany. The mission consisted of two satellites following each other. It was operated by German Space Operations Center (GSOC) in Darmstadt, Germany. It was the first dedicated mission launched to map the global time-variable gravity field of the Earth.

The GRACE mission was launched to an altitude of ≈ 500 km with 220 ± 70 km along track separation between the two satellites. Due to the separation, the trailing satellite passes 28 seconds later over the same area through which the leading passes. The satellite orbit is inclined with an inclination angle of 89° which leads to near-global coverage. It takes about 93 minutes for GRACE to complete one revolution around the Earth, resulting in about 15.5 revolutions per day. The mission was originally planned for a period of minimum 5 years. However, it provided science results until mid-2017, which is more than 15 years. The next mission, GRACE Follow-On (G-FO) has been launched on 22 May 2018 to continue the Earth's gravity field measurements from space.

2.2 Applications

Global gravity field solutions computed from GRACE have a wide number of applications, such as in hydrology, in sea level rise studies, understanding the nature of ocean currents and ocean heat storage phenomena. In terrestrial hydrology, the GRACE data has been used to determine the regional total water storage content. The global measurements from GRACE provide information on seasonal and inter-annual river basin water storage changes (Rodell and Famiglietti, 2002; Steitz et al., 2002). Some of the recent and important contributions of GRACE include the study of ground water discharge in the states of Punjab, Rajasthan and Delhi, India

(Chinnasamy et al., 2015; Rodell et al., 2009). The California drought has also been studied using GRACE data (Famiglietti, 2014).

Knowledge about melting of the glaciers is essential to study and keep track of the sea level rise. Since from GRACE data, the rate of mass change can be derived, one can study the rate of melting of big glaciers, loss of mass of big polar ice sheets and thermospheric effects in the oceans (Hsu and Velicogna, 2017). These factors contribute to the budget of sea level rise which is an important concern today for scientists and society.

GRACE data has been successfully used in oceanographic studies, e.g. Kuo et al. (2008) studied the ocean currents. Boening et al. (2012); Kanzow et al. (2005); Landerer et al. (2008) studied temperature-dependent phenomena in the oceans such as El-Nino, La-Nina and ocean bottom pressure changes. Recently, an achievement has been made by the detection of climate driven polar motion changes by Adhikari and Ivins (2016). Overall, GRACE being the first satellite-to-satellite tracking mission has been really successful in terms of technology as well as in science applications.

2.3 The GRACE observation system

The GRACE mission is based on low-low Satellite-to-Satellite Tracking (LL-SST). This principle uses two satellites following each other while moving around the Earth. The two satellites serve as test masses which are sensitive to the mass distribution and its changes inside and on the surface of the Earth. The spatial distribution of mass causes variations in the relative distance between the center of masses (COM) of the two satellites. Observing the relative distance requires the establishment of a satellite-to-satellite tracking (SST) technique. Realizing this SST principle needs the knowledge of precise orbit and inter-satellite ranging. These requirements are fulfilled by the GRACE payload which consisted of (major components):

1. GPS space receiver for orbit determination,
2. Accelerometer (ACC),
3. K-band Ranging Microwave Assembly (KBR),
4. Star Camera Assembly (SCA).

1. GPS Receiver – The GRACE GPS space receiver was provided by JPL, NASA (see Fig. 2.1a). The receiver is used for Precise Orbit Determination (POD) with

cm-accuracy, time-tagging of all payload data, and atmospheric and ionospheric profiling. To compute the precise orbit of GRACE, satellite-to-satellite tracking between the GRACE and the high-altitude orbiting GPS satellites is applied (Flechtner, 2000). The absolute positions of the satellites provided by the GPS measurements are also important for gravity field parameter estimation. They are required to geo-reference the KBR observations. In other words, the orbit of the GRACE satellites, computed from the inter-satellite range (SST) measurements only, suffers a singularity problem. The inter-satellite ranges being relative measurements are not sufficient to measure the absolute position of each satellite. This singularity problem is alleviated by the GPS measurements which are necessary to obtain a well-conditioned solution (Kim and Tapley, 2002).

2. Accelerometer – Each GRACE spacecraft carries an electrostatic 3-axis accelerometer at its center of mass which measures the electrostatic force necessary to maintain the accelerometer proof mass motionless with respect to the sensor cage (see Fig. 2.1b). The electrostatic force is proportional to the acceleration of the spacecraft due to non-gravitational forces acting on the satellite, i.e. the atmospheric drag, solar radiation pressure and Earth’s albedo (Touboul et al., 1999b).

The accelerometers are used in gravity field recovery. The effects of non-gravitational forces, observed by the accelerometer, are reduced from the inter-satellite ranging measurements to isolate the gravity field information. Thus, the accuracy of the accelerometer observations directly affects the recovered gravity field (more details are discussed in the following sections and later in Chapter 5).

3. K-Band Ranging (KBR) Microwave Assembly – The K-band microwave ranging assembly system is the key science instrument of GRACE which measured the dual one-way range change between both satellites with a precision better than $1\text{ }\mu\text{m/s}$. The system uses a single horn antenna for transmission and reception of the dual-band K- (24 GHz) and Ka-band (32 GHz) microwave signals. Each satellite transmits carrier phase signals on the two frequencies. The linear combination of the sum of those phase measurements at each frequency gives an ionosphere-corrected measurement of the range between the satellites (Flechtner, 2000; Thomas, 1999).

4. Star Camera Assembly (SCA) – The star camera assembly provided by Denmark Technical University consists of two star cameras onboard each spacecraft (see Fig. 2.1c). These sensors are used for the precise pointing between the two

satellites. The attitude of the satellite is determined from the stars in the field of view of the star camera (Dunn et al., 2002). Once the attitude of a spacecraft is obtained, it is compared with the requirements necessary to maintain the pointing between the two satellites. The attitude is then corrected using the attitude control sensors, i.e. thrusters and magnetic torquer rods.

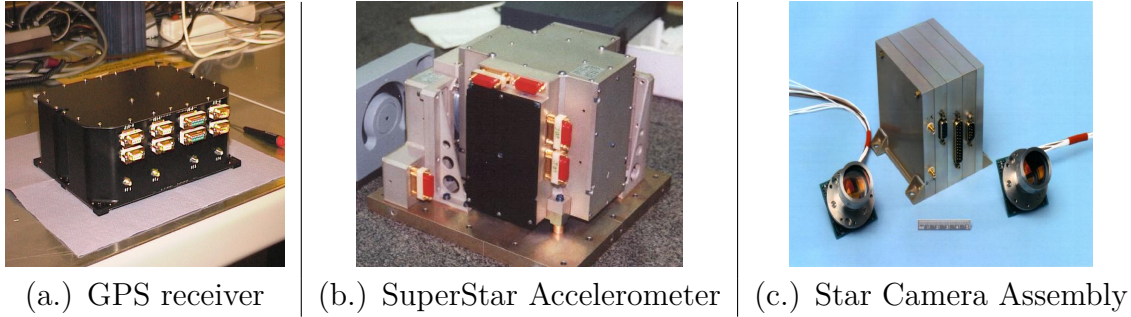


Figure 2.1: *GRACE Payload*, ©Flechtner (2000)

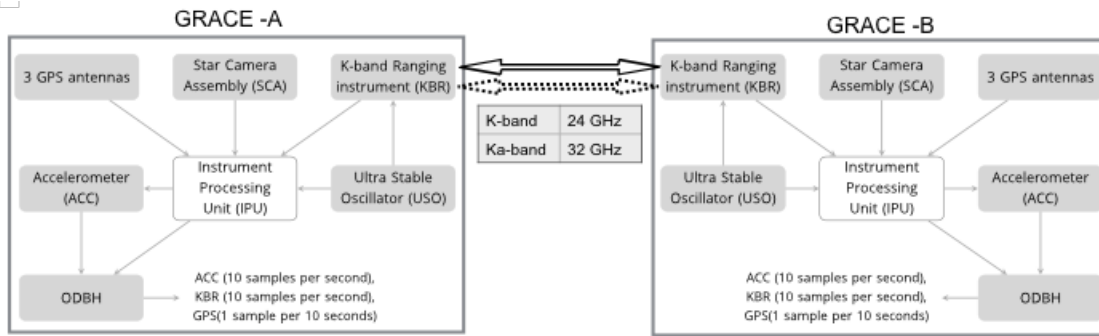


Figure 2.2: *Instrument system of the GRACE satellites*

The twin GRACE satellites work as a single scientific instrument measuring the range and its changes between the two satellites (cf. Fig. 2.2). The two spacecraft transmit and receive the signal through the microwave link. They both have their own instrument system which are identical in terms of their design. As shown in Fig. 2.2, the heart of the satellite is the Instrument Processing Unit (IPU) which has a Signal Processing Unit (SPU) as sub-component. The IPU extracts the observables from the Radio Frequency links (GPS and K-band) and spacecraft attitude from the images recorded by the star cameras. It digitizes the KBR and GPS signals. The accelerometer data is time-tagged by the IPU and then sent to the On Board Data

handling (ODBH) computer to be telemetered to the ground. Thus, IPU serves as a data interface to ODBH (Dunn et al., 2002).

The telemetry data is received on-ground and tagged as Level 0 data. This Level 0 binary data is converted to the so-called Level 1A data readable format. Then, this raw Level 1A data is processed to get the Level 1B data which is available with the sampling rate shown in Table 2.1. The Level 1A data sampling rates is 10 Hz. The processed Level 1B data, which are used for gravity field recovery, is provided

Table 2.1: *The Level 1B datasets along with their sampling rates obtained from the Level 1A datasets. These are used in global gravity field parameter estimation.*

Level 1B product	Data content	sampling frequency (Hz)
K-BAND RANGING DATA		
KBR1B	Range, range-rates, light-time and antenna offset corrections	0.2
ACCELEROMETER		
ACC1B	Linear and angular accelerations	1
STAR CAMERA		
SCA1B	Star camera quaternions	0.2
REDUCED DYNAMIC ORBIT		
GNV1B	Position and velocity of the spacecraft	0.2

with sampling frequencies of 0.2 Hz and 1 Hz respectively (see Table 2.1). The data processing from Level 0 to Level 1B is done by the Jet Propulsion Laboratory, NASA, USA. Details of the data processing from Level 1A to Level 1B are given in Wu et al. (2006).

2.4 Global gravity field parameter estimation from GRACE observations

The range-rate measurements are the main observables used to estimate the global gravity field parameters. The estimated parameters are the Stokes coefficients which represent the variations in the global gravity field of the Earth. Here, first the representation of the global gravity field from the Stokes coefficients is discussed. Later, the full parameter estimation chain is described which has been used to estimate these Stokes coefficients from the range-rate observations.

2.4.1 Gravity field representation

The gravity field of the Earth is represented as an expansion series of harmonic functions which is expressed as (Heiskanen and Moritz, 1967)

$$V(r, \Theta, \lambda) = \frac{GM}{R} \sum_{l=0}^{\infty} \left(\frac{R}{r} \right)^{(l+1)} \sum_{m=0}^l \left(\bar{C}_{lm} \cos m\lambda + \bar{S}_{lm} \sin m\lambda \right) \bar{P}_{lm}(\cos \Theta), \quad 2.1$$

where G is the gravitational constant, M is the mass of the Earth, R is the radius, (r, Θ, λ) are the position coordinates at which the gravity field is calculated, \bar{P}_{lm} the normalized Legendre functions, \bar{C}_{lm} and \bar{S}_{lm} are the normalized dimensionless Stokes coefficients, l and m are the degree and order of the expansion series.

In reality, the infinite sum of degrees (l) is truncated. In this thesis, the field is truncated to degree and order 60.

2.4.2 Gravity field modeling

A number of methods to compute the global gravity field parameters has been developed. Some of the important and frequently used approaches are: *the Energy balance approach*, *the Acceleration approach*, *the Variational equations approach*, *the Celestial mechanics approach*. After the launch of the GRACE mission, data processing centers started to estimate global gravity field solutions using these approaches. These gravity field models can be downloaded from: <http://icgem.gfz-potsdam.de/series>, an IAG service provided by GFZ (Barthelmes and Köhler,

2016).

The Energy balance approach of recovering the gravity field from inter-satellite range-rate observations was introduced by Jekeli (1999). A simple model was derived on the basis of energy conservation that relates the measured range-rates between two satellites to the gravitational potential difference. For more details, see Jekeli (1999).

The acceleration approach, which is based on Newton's second law of motion, links the acceleration vector to the gradient of the gravitational potential. According to Liu (2008), advantage of the acceleration approach is, the errors due to linearization are minimized whereas its limitation lies in the amplified noise in the range accelerations which are obtained by double differentiation of the range observations. The most traditional way of gravity field determination is the variational equations approach, e.g. (Reigber, 1989). It combines the problem of parameter estimation with the dynamic orbit determination. In this approach, the dynamic orbit integration is extended to determine the Stokes coefficients (\bar{C}_{lm} , \bar{S}_{lm}). Since the relation between the unknown parameters and the observations is non-linear, it is linearized to solve the problem of parameter estimation. This approach is computationally more challenging as compared to the other two. For details, see Montenbruck and Gill (2000); Tapley et al. (2004b).

A variant of the variational equations approach was further explored by Mayer-Gürr (2006) to recover the global gravity field parameters using short arcs. The approach was first applied to compute CHAMP gravity field solutions using kinematic orbits. The method was then further extended to compute gravity field solutions from the GRACE inter-satellite ranging measurements. A series of gravity field models from GRACE observations has been computed starting from ITG¹-GRACExx² (Mayer-Gürr, 2007; Mayer-Gürr et al., 2006) to ITSG³-yyyy⁴ (Klinger et al., 2016; Mayer-Gürr et al., 2014). Every model is an improved version of the previous one in terms of the estimation scheme, noise modeling, data processing and others.

The GRACE gravity field solutions and the corresponding range-rate residuals analyzed in this thesis are computed using the GROOPS software. It is a software

¹Institute of Theoretical Geodesy

²gravity model number, e.g. 01, 02, etc.

³Institute of Theoretical and Satellite Geodesy

⁴year

package Gravity Recovery using Object Oriented Programming Software (GROOPS) and was written by Torsten Mayer-Gürr and his colleagues from Bonn University, Germany. Processing standards of the ITSG-2014 global gravity field models are used here (Mayer-Gürr et al., 2014) with the following adaptations:

1. Dynamic orbit integration was adapted to the Encke's orbit integration approach explained by Ellmer and Mayer-Gürr (2016).
2. No K-band antenna offset corrections were estimated. In the standard ITSG-2014 solutions, the K-band antenna offset corrections were estimated once per month. But due to the unreliable characteristics of those estimates, they are not estimated here.

The steps of the ITSG-2014 data processing chain are as follows (Mayer-Gürr et al., 2014):

Data preprocessing – The GRACE Level 1B data as mentioned in Table 2.1 are preprocessed to be fed into the dynamic orbit integrator. The preprocessing includes:

- *resampling* of the star camera data (quaternions) and linear accelerations from the accelerometer. The linear accelerations are resampled from 1 s to 5 s sampling rate. The star camera data and the linear accelerations are synchronized.
- *rotation* of linear accelerations from the Science Reference Frame (SRF) to the Earth-Centered Inertial (ECI) Reference Frame using the quaternions (more details are provided in Chapter 3). The quaternions used in the ITSG-2014 processing are computed by combining the star camera data and angular accelerations from ACC1B data using a variance component estimation approach (Klinger and Mayer-Gürr, 2014).
- *data synchronization*: Synchronization of the orbit (GNV1B) and the linear accelerations along with the resampling of the kinematic orbits at 5 minute sampling rate. The kinematic orbits for GRACE-A and GRACE-B are processed by Zehentner (2016). Both GNV1B orbits are rotated from the Earth-Centered Earth-Fixed (ECEF) reference frame to the ECI reference frame using the IERS2010 conventions (Petit and Luzum, 2010) .

Dynamic orbit integration – The orbit for each satellite is integrated using Encke's orbit integration approach (Ellmer and Mayer-Gürr, 2016). The 24 hours

dynamic arc is computed by integrating all forces perturbing the orbit using a polynomial approach. The perturbing forces include gravitational and non-gravitational forces as mentioned in the Table 2.2. The integrated orbit is fitted to the kinematic

Table 2.2: *List of perturbation forces and their models which are applied during orbit integration.*

Forces	Models
Earth rotation	IERS 2010 (Petit and Luzum, 2010)
Direct tides (Moon, Sun and planets)	JPL DE421 (Folkner et al., 2009)
Solid Earth tides	IERS 2010 (Petit and Luzum, 2010)
Ocean tides	EOT11a (Savcenko and Bosch, 2012)
Pole tides	IERS 2010 (Petit and Luzum, 2010)
Ocean pole tides	Desai 2003 (Petit and Luzum, 2010)
Atmospheric tides (S1, S2)	Bode-Biancale 2003 (Bode and Biancale, 2006)
Atmosphere and Ocean Dealiasing	AOD1B RL05 (Flechtner et al., 2015)
Relativistic corrections	IERS 2010 (Petit and Luzum, 2010)
Permanent tidal deformation	includes (zero tide) (Petit and Luzum, 2010)
Non conservative forces	Accelerometer

orbits. Then this fitted orbit is used as a taylor point for further iterations. The differences between the coordinates of the successive iterations are used to assess the quality of the integrated orbit. After a few iterations, the difference between the two integrated orbits converges to the machine precision (typically within micro meters).

Parameter estimation – A schematic view for solving the problem of global gravity field parameter estimation based on the approach of Mayer-Gürr (2006) is shown in Fig. 2.3. The observation equation in Fig. 2.3 (b.) is a linearized overdetermined system of equations which are solved using the least-squares approach. The least-squares variance component estimation is used for the recovery of global gravity field parameters (Koch, 1990; Koch and Kusche, 2002).

In Fig. 2.3 (a.), the observation vector \mathbf{l} of size $(n \times 1)$ contains the *pre-fit range-rate residuals* along with the orbit parameters (\mathbf{r} and $\dot{\mathbf{r}}$) and the accelerometer scale and bias parameters. The *pre-fit range-rate residuals* are computed as:

$$\mathbf{l}_{n \times 1} = (\dot{\rho}_{\text{KBR}} - \dot{\rho}_0)_{n \times 1}, \quad 2.2$$

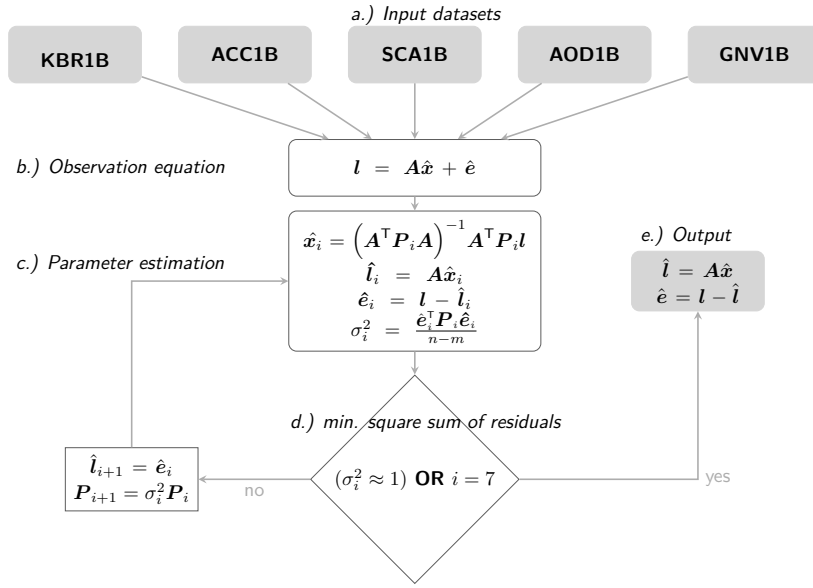


Figure 2.3: Diagrammatic representation of the chain followed for global gravity field parameter estimation from GRACE observations.

where $\dot{\rho}_0$ contains the reduced range-rate observations computed from the integrated dynamic orbit. In Fig. 2.3 (b.), $\mathbf{A}_{(m \times n)}$ is the information matrix (also called as design matrix), $\hat{\mathbf{x}}_{(n \times 1)}$ is the vector of parameters to be estimated (cf. Eq. 2.3) and $\hat{\mathbf{e}}_{(m \times 1)}$ contains the noise in the orbit and the range-rate observations,

$$\hat{\mathbf{x}}_i = \begin{bmatrix} C_{nm}, S_{nm} \\ \text{orbit parameters } (\mathbf{r}, \dot{\mathbf{r}}) \\ \text{accelerometer scale and bias} \end{bmatrix}, \quad (2.3)$$

$$\hat{\mathbf{e}}_i = \begin{bmatrix} \text{range-rate residuals} \\ \text{orbit residuals} \end{bmatrix}. \quad (2.4)$$

The estimation of $\hat{\mathbf{x}}$ is a correction to the a-priori solution. It is obtained in the normal equations approach as shown in Fig. 2.3(c.). This system of equations is solved using an iterative least-squares variance component estimation approach with an arc-length of 3 hours for each day. The Cholesky decomposition method is used to solve for the system of normal equations and the covariance matrix in order to reduce the computational costs. In order to minimize the noise from the observations, a weight matrix (\mathbf{P}) (cf. Fig. 2.3 (c.)) is introduced in which relative weights are

assigned on the basis of the noise content of the observations. The weight matrix is

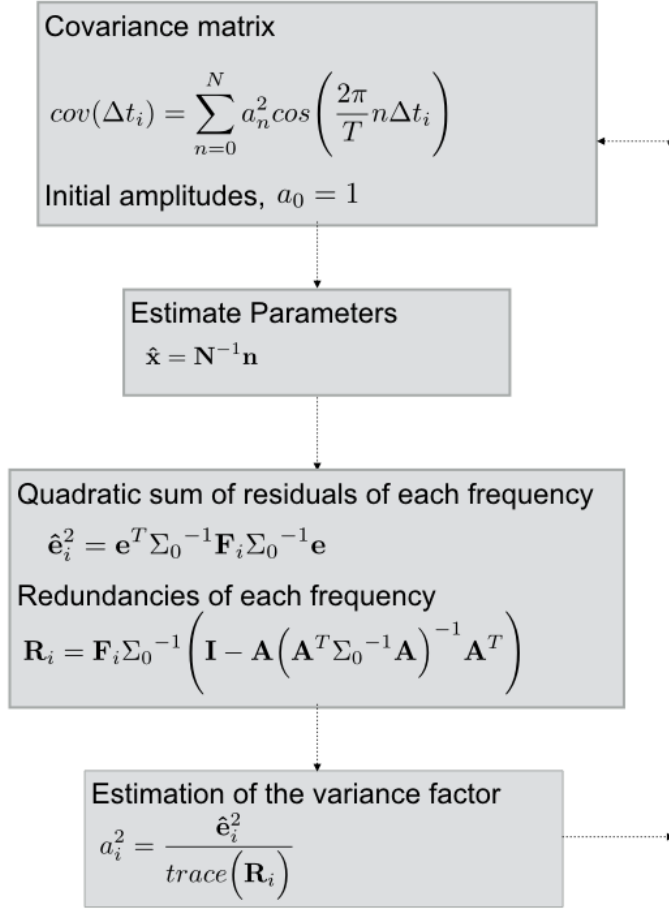


Figure 2.4: A schematic flow of the computation of the covariance matrix in ITSG-2014 model from the estimated residuals in an iterative least-squares variance component estimation approach, after Mayer-Gürr (2015).

computed from the covariance information of the noise in the observations. Thus, it is also called as the covariance matrix. In the ITSG-2014 gravity field solutions, the covariance matrix $\left(\Sigma\right)$ is estimated on the basis of a noise model described by the observation noise in the frequency domain as

$$\Sigma = a_1^2 \mathbf{F}_1 + a_2^2 \mathbf{F}_2 + \cdots + a_N^2 \mathbf{F}_N, \quad (2.5)$$

where, $\mathbf{F}_N = \left(\cos\left(\frac{2\pi}{T} n (t_i - t_k)\right) \right)$.

In the Eq. 2.5, $a_1^2 \cdots a_N^2$ are the amplitudes of N frequencies, $(t_i - t_k)$ are the differences between two adjacent time epochs.

The noise information is taken from the set of residuals $(\hat{\mathbf{e}}_i)$ obtained after each fit as shown in Fig. 2.3 (c). The content of the residual vector is given in Eq. 2.4.

During each iteration, the noise covariance information is computed from the residuals of the fitted observations in the frequency domain. The covariance matrix is updated with that information where Σ_0 is initialised as an identity matrix (cf. Fig. 2.4) (Mayer-Gürr, 2015). This approach helps to improve $\hat{\mathbf{x}}$ as observations are weighted according to their accuracy (in frequency domain). After the full parameter estimation, the estimated unknown parameters, i.e. $\hat{\mathbf{x}}$, are obtained (cf. Eq. 2.3).

Although the set of residuals $\hat{\mathbf{e}}$ contain orbit and range-rate residuals (cf. Eq. 2.4) the range-rate residuals are referred to as $\hat{\mathbf{e}}$ in the rest of the work for the ease of the reader. It is also because the analysis of other sets of residuals is out of the scope of this work. Since the range-rate residuals analyzed in this work are computed after full parameter estimation, they are referred to as *post-fit range-rate residuals*, also in short *postfits* or *post-fit residuals*.

As shown in Fig. 1.1, the Power Spectral Density (PSD) of the range-rate residuals should be at the level of the predicted sensor noise. In the current scenario, there is still a gap of one order of magnitude between the PSD of the expected sensor noise and the obtained range-rate residuals. At the same time, it is easily visible that the PSD of the range-rate residuals contains typical signal type characteristics (example 1, 2, ... CPR). This clearly indicates the insufficiency of the current modeling approach which is not fully able to exploit the GRACE measurement accuracy. It also indicates that the residuals may contain some noise which is predictable, i.e., it is not just random. As mentioned previously, the gap in the PSD of the range-rate residuals and the expected sensor noise also indicate that the potential of the sensors is not fully exploited yet and thus, it could be one of the factors limiting the accuracy of the gravity field solution. When the estimated solutions are compared with the anticipated GRACE accuracy baseline, the existing gap between the two curves make this implication even stronger (cf. top panel of Fig. 1.1). Therefore, a good understanding of the noise characteristics from all input data is essential to understand the reasons behind the limitations in the accuracy of the GRACE solutions.

In the following chapters, noise in the three main input datasets will be discussed i.e., star cameras, accelerometer and K-band microwave ranging measurements along with their error contribution in the range-rate residuals.

2.5 Analysis kit used for studying the residuals

In this thesis, an analysis of the post-fit range-rate residuals is carried out in the following chapters. These residuals are computed after estimating the global gravity field parameters using the ITSG-2014 processing chain described in the previous sections. In the following subsections, the methods and representations used to study the error characteristics of the observations and the error analysis of the gravity field solutions are introduced.

2.5.1 Degree amplitudes

The errors of the recovered global gravity field spherical harmonic coefficients is determined as their 1-D spectra. The error degree variances are given as (Kaula, 1967; Sneeuw, 2000)

$$\sigma_l^2 = \sum_{m=0}^l (C_{lm}^2 + S_{lm}^2), \quad 2.6$$

where l, m are the *degree* and *order* of the Stokes coefficients or spherical harmonic coefficients. Eq. 2.6 represents the total signal power of the coefficients. In this thesis, results are investigated for the parameters estimated up to degree and order 60. The investigated results are represented as the geoid degree amplitudes which is obtained as

$$\sqrt{\sigma_l^2} \times R, \quad 2.7$$

where R is the radius of the Earth which is 6.378136×10^6 meters.

A representation of geoid amplitudes vs degree for example is shown in top panel of Fig. 1.1 of Chapter 1.

2.5.2 Power Spectral Density (PSD)

It describes how the power of a time-series is distributed with frequency. A PSD is also defined as the fourier transform of the autocorrelation sequence of a time-series (Heinzel et al., 2002). A PSD of a time-series $y(t)$, where t is the time, is

defined as

$$\phi(\omega) = \sum_{k=-\infty}^{\infty} r(k)e^{-i\omega k}, \quad 2.8$$

where $\omega = 2\pi f$, f is frequency.

$r(k)$ is the autocovariance sequence given as

$$r(k) = E\{y(t)y^*(t - k)\}, \quad 2.9$$

where E is the expectation operator and k represents the lag factor which is 0 for the autocovariance function.

PSDs of the continuous segments of the satellite observations are computed using the “lpsd” method provided in the LTPDA toolbox (Hewitson, 2007). For example, the PSD of residuals is shown in the bottom panel of Fig. 1.1. In all cases, a *Hanning Window* has been used with 50 % overlap with a Peak SideLobe Level¹(PSLL) of 31.5 dB. More details about the implementation of the “lpsd” method are provided in Heinzel et al. (2002).

2.5.3 Time-series analysis

The time-series representation gives the observations (on y-axis) and their variations with respect to time (on x-axis) (for example, Fig. 4.3). It is helpful for understanding the variations in the characteristics of the satellite observations with respect to time such as the systematics related to the satellite-orbit maneuvers.

For the statistical analysis of the time-series, the correlations are also exploited further. The *correlation coefficients* of two random variables define the linear dependence between them. The *Pearson correlation coefficient* used in this work is

¹The window function in the frequency domain contains the central peak which is the desired one alongwith many side peaks at regular intervals. These side peaks are called ‘sidelobes’. The aim is to reduce the amplitude of these sidelobes without widening the noise bandwidth. The widening of the noise bandwidth causes spectral leakage. Hence, a compromise between the sidelobe level and the noise bandwidth is important in designing the window function (Heinzel et al., 2002).

computed as (Press et al., 1992)

$$\rho(\mathbf{A}, \mathbf{B}) = \frac{cov(\mathbf{A}, \mathbf{B})}{\sigma_{\mathbf{A}} \sigma_{\mathbf{B}}}, \quad \text{where} \quad 2.10$$

$$cov(\mathbf{A}, \mathbf{B}) = \frac{1}{N-1} \sum_{i=1}^N (\mathbf{A}_i - \mu_{\mathbf{A}})^* (\mathbf{B}_i - \mu_{\mathbf{B}}). \quad 2.11$$

$\mu_{\mathbf{A}}, \mu_{\mathbf{B}}$ are the mean of the two variables or time-series \mathbf{A} and \mathbf{B} each of length N . $\sigma_{\mathbf{A}}$ and $\sigma_{\mathbf{B}}$ are the standard deviations of \mathbf{A} and \mathbf{B} . The symbol $*$ denotes the complex conjugate of the term $(\mathbf{A}_i - \mu_{\mathbf{A}})$.

Due to the large number of observations, the correlations computed between the two different sets of time-series are represented here in terms of *box-plots*. A sample box-plot figure is Fig. 2.5. The box-plots are used to show the range, median and quartile information of the correlation coefficients altogether for a period of time. In most cases, the correlation coefficients are computed on a daily basis for a month

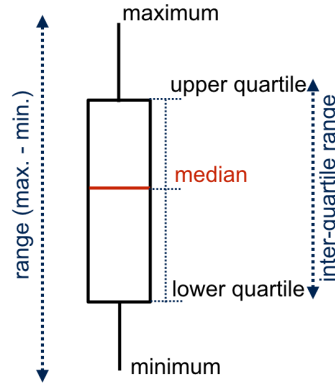


Figure 2.5: Representation of the distribution of a set of observations on a box-plot.

of observations. Thus, box-plots show the range, median and quartile information of the daily correlation coefficients over a month.

2.5.4 Argument of latitude

The argument of latitude (u) is an angular parameter which defines the angle between the ascending node and the moving body. It varies from 0 to 2π for a full orbit. A representation of the argument of latitude in the satellite orbit is shown in panel (a) of Fig. 2.6. It is the sum of the true anomaly (ν) and argument of perigee

(ω), given as (Seeber, 2003)

$$u = \nu + \omega. \quad 2.12$$

The argument of latitude used in this thesis is computed from the position \mathbf{r}_{sat} and velocity $\dot{\mathbf{r}}_{sat}$ of the satellite given in the Earth Centered Inertial (ECI) reference frame as

$$\mathbf{u} = \arctan \left(\frac{\mathbf{r}_z}{-\mathbf{r}_x \cdot \mathbf{h}_y + \mathbf{r}_y \cdot \mathbf{h}_x} \right), \quad 2.13$$

where

$$\begin{aligned} \mathbf{r}_{sat} &= (\mathbf{r}_x, \mathbf{r}_y, \mathbf{r}_z) \\ \dot{\mathbf{r}}_{sat} &= (\dot{\mathbf{r}}_x, \dot{\mathbf{r}}_y, \dot{\mathbf{r}}_z) \end{aligned} \quad 2.14$$

and

$$\mathbf{h} = (\mathbf{h}_x, \mathbf{h}_y, \mathbf{h}_z) = \frac{\mathbf{r}_{sat} \times \dot{\mathbf{r}}_{sat}}{|\mathbf{r}_{sat} \times \dot{\mathbf{r}}_{sat}|}. \quad 2.15$$

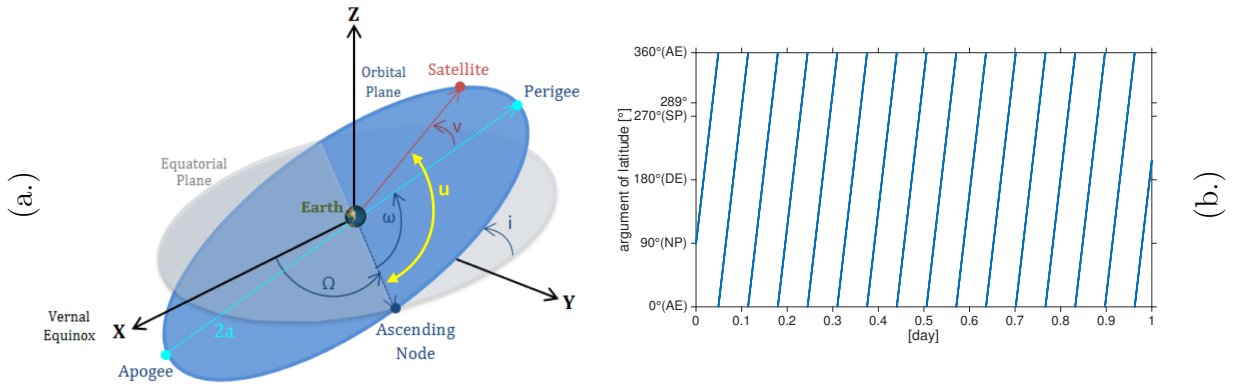


Figure 2.6: (a.) Argument of latitude (\mathbf{u}) for the satellite at an epoch shown in an orbit after <https://www.gsc-europa.eu/system-status/orbital-and-technical-parameters>. (b.) GRACE orbit for the length of 1 day shown along the argument of latitude and time.

The plots of the satellite observations along the *argument of latitude* vs *time* (cf. Fig. 2.6 (b.)) are helpful in studying their long-term systematic effects varying with time and orbit. Therefore, they are often used in this thesis. Such plots are also

helpful in finding the dependencies between two sets of observations which sometimes are not captured by, for example, correlation coefficients. These dependencies describe the possible causal effects of one observation to another. A knowledge of these causal effects is important as such dependencies can be used to model errors and hence reduce them in the estimated gravity field parameters.

2.5.5 Satellite ground tracks

The projection of the orbit of a satellite onto the surface of the Earth is called ground track (Curtis, 2005; Seeber, 2003). When the direction of the ground track of a satellite is from the south to the north pole, the path covered is called *ascending arc*, whereas the *descending arc* is the ground track covered by the satellite from the north to the south pole. In Fig. 2.7, an *ascending arc* of the ground track covered by the GRACE satellites is plotted for 7 days. The ground track of a satellite

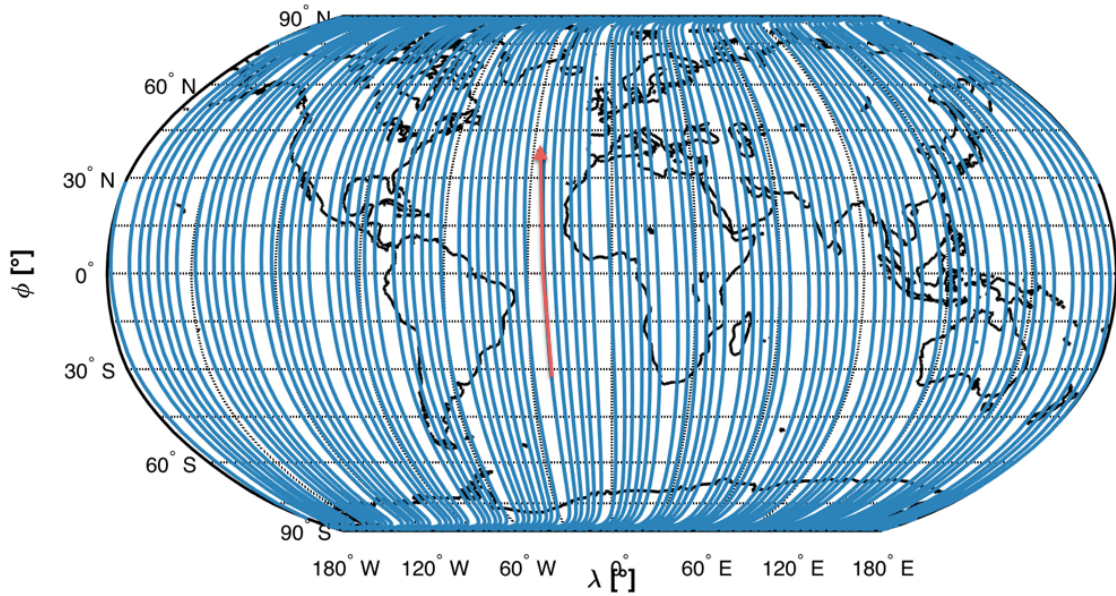


Figure 2.7: Ground-track coverage of the Earth by the GRACE satellites from December 1st to 7th 2008. The ground-track is plotted for the ascending orbit (upward direction of flight) of the spacecraft.

is given by its geographical coordinates (λ, ϕ, h) . The geographical coordinates are computed from the cartesian coordinates of the satellites $(\mathbf{r}_x, \mathbf{r}_y, \mathbf{r}_z)$ given in the

Earth Centered Earth Fixed (ECEF) frame of reference as

$$\begin{aligned}\phi &= \tan \left(\frac{\mathbf{r}_z}{\sqrt{\mathbf{r}_x^2 + \mathbf{r}_y^2}} \right), \\ \lambda &= \tan \left(\frac{\mathbf{r}_y}{\mathbf{r}_x} \right), \\ h &= \frac{\sqrt{\mathbf{r}_x^2 + \mathbf{r}_y^2}}{\cos(\phi)}.\end{aligned}\tag{2.16}$$

For an *ascending arc*, the change in ϕ , i.e. $(d\phi)$, for two consecutive epochs must be $> 0^\circ$. For a *descending arc*, $d\phi$ for any two consecutive epochs must be $< 0^\circ$. Analyzing the observations on the ground-track representation is helpful when their geographical variations are of interest. Here, it is useful to analyze weekly, fortnightly or monthly observations. For the analysis of long-term geographical variations, it is advised to chunk the observations into small time intervals, otherwise too much overlap of information can be misleading in the interpretation of the analysis results.



Analysis of K-band range-rate residuals

Chapter 3: Inter-satellite pointing errors in range-rate residuals

In this chapter, an analysis of the range-rate residuals is presented with focus on the satellite pointing errors. The two spacecraft need pointing information in order to measure the precise range changes as well as for the gravity field determination. Due to the use of pointing information in the gravity field recovery process, related errors also propagate to the gravity field solutions through range-rate information. In this chapter, these pointing errors are studied by analyzing the attitude data (used to derive pointing information). Further, the range-rate residuals are analyzed to identify the pointing errors present in them.

3.1 What is inter-satellite pointing?

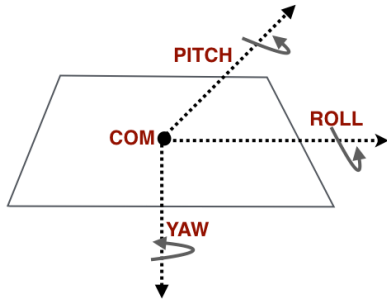
Inter-satellite pointing is a part of the Attitude and Orbit Control System (AOCS). The AOCS is responsible for the attitude determination and its control in the satellite. The sensors used for determination of the attitude in GRACE are the Star Camera Assembly (SCA), the Inertial Measurement Unit (IMU) and the Coarse and Earth Sun sensors (CESS), where main attitude determination sensors in GRACE are the star cameras.

The CESS are used for the initial acquisition of the attitude but they are not as accurate as the star cameras. The accuracy of the CESS ranges between $\approx 5^\circ - 10^\circ$ for the Earth-vector and $\approx 3^\circ - 6^\circ$ for the Sun-vector depending on the orbit geometry (Herman et al., 2004). IMUs provide the angular rates of the spacecraft along three axes and angular accelerations are provided as a side-product by the accelerometer along with the linear accelerations. Attitude of a spacecraft is controlled by the thrusters and the magnetic torquer rods used along the three pointing axes roll, pitch and yaw (see Fig. 3.1 (a.)).

The pointing between the two satellites is a fundamental requirement of a satellite-to-satellite tracking mission. Perfect pointing is required to measure the precise range between the two satellites. In GRACE, the range between the two satellites is defined as *the distance between the phase centers of the K-band ranging assembly*

of the two satellites. For precise range measurements, the phase center should be aligned with the line-of-sight (LOS), but in reality there is an offset between the phase center and the LOS (see Fig. 3.2). This could be due to external and internal perturbations on the satellite. Therefore, the measured range and range-rate observations are corrected to get their values along the LOS vector (Herman et al., 2004). These corrections are called antenna phase center offset corrections (AOC) which are discussed in detail in Section 3.3.

The maintenance of the pointing between the two satellites in their orbit is one of the most difficult and important tasks. The variations in the pointing angles should be kept minimum as they directly affect the measured range observations. There are dead bands defined for the maximum allowed pointing variations between the two satellites. These dead bands are defined for the roll, pitch and yaw axis, respectively, see Table 3.1 (b.).



(a.)

Pointing angles	dead band limit (mrad)
Roll	2
Pitch	4
Yaw	4 (since 2002)
	4.4 (since October 2007)
	4.8 (since June 2008)
	5.2 (since January 2012)

(b.)

Figure 3.1: (a.) Depiction of roll, pitch and yaw axes in the GRACE spacecraft. (b.) The dead band limits for the three pointing angles in GRACE (Herman et al., 2004; Herman and Steinhoff, 2012)

Since the pointing information of the satellites is derived from the attitude data, the precision of the attitude data is crucial for precise pointing. The precision of the attitude is also important for the gravity field determination because it directly affects the precision of the range observations in two ways. *First*, the range observations are corrected for these pointing imperfections, so called AOC, using the attitude data (see Fig. 3.2). These corrections are applied to the range observations in post-processing to get these observations along the LOS of the two spacecraft. *Second*, the range observations are also corrected for the effects of the non-gravitational accelerations acting on the satellite. Accelerometers are used to measure the non-

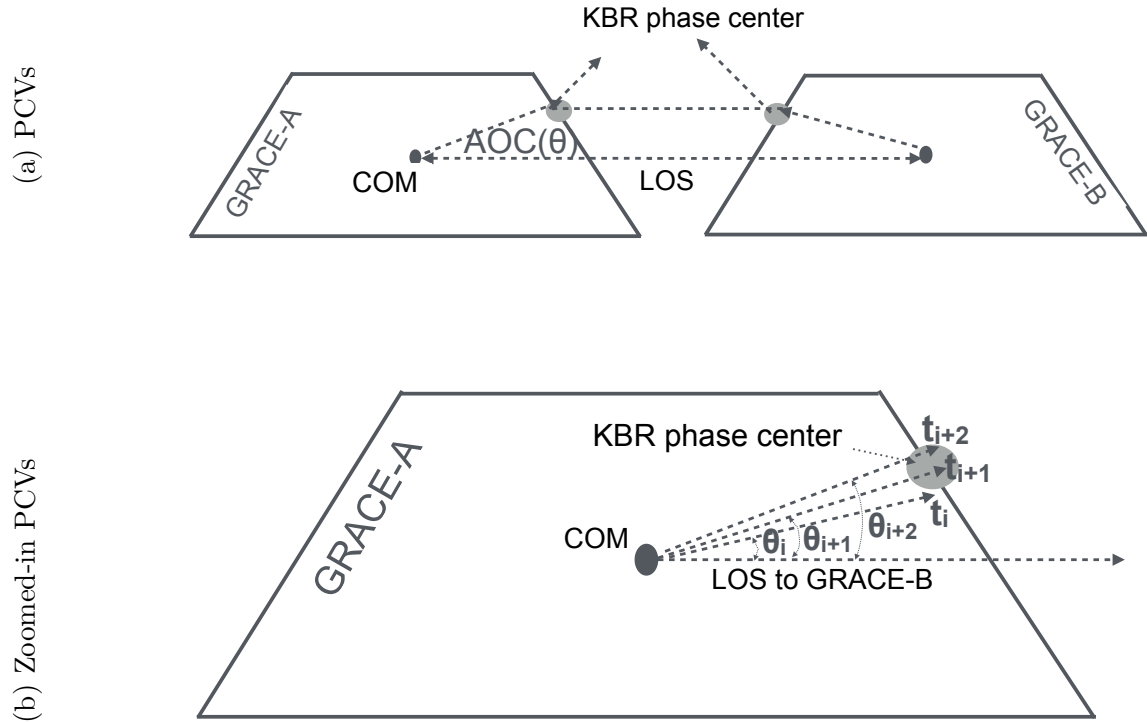


Figure 3.2: (a.) The antenna phase center offset (AOC) is defined by the angle (Θ) between the two KBR phase centers and the center of mass (COM) of the two satellites. (b.) Variations in angle (Θ) at every epoch because the angle varies with the change of satellite orientation.

gravitational accelerations acting on the satellites. The accelerometer observations, which are provided in the instrument frame (here it is the Accelerometer frame), are rotated into the ECI frame of reference using the attitude data. Then, the orbit is corrected for the effect of non-gravitational forces acting on the satellites. Therefore, an understanding of the precision of the attitude is important in order to understand the effects of pointing on the range observations.

3.2 GRACE attitude - its characteristics and errors

For GRACE gravity field processing, star cameras are the main sensors for providing attitude information due to their high accuracy. Currently, the main gravity field processing centers (JPL, CSR, GFZ) derive the attitude from the two star camera data sets. The derived attitude data is available as SCA1B product to the GRACE science community. As it is one of the many input datasets used in the gravity field computation, an understanding of its characteristics is important for *the attitude error analysis of the GRACE mission*. Also, there is no attitude or star camera error model available till today. Thus, full understanding of the attitude errors is highly required as it might be one of the major error contributions. During the lifetime of GRACE, studies had been carried out with focus on the quality of the star camera data, their characteristics and errors (Bandikova, 2015; Bandikova et al., 2012; Horwath et al., 2011; Inácio et al., 2015). Thanks to these contributions, a significant improvement was achieved in the understanding of star camera data characteristics and the importance of their accuracy in GRACE.

Horwath et al. (2011) has shown evidence of a bias in the antenna phase center corrections and its impact on the gravity field. This investigation led to updated antenna phase center coordinates with reprocessed antenna phase center offset corrections. The reprocessed antenna phase center offset corrections are provided in the version 2 KBR1B data since 2012.

Bandikova et al. (2012) presented an analysis of the star camera data characteristics and their systematic errors. Later, Bandikova and Flury (2014) reprocessed the GRACE star camera data (SCA Level 1A to SCA Level 1B processing) by combining the star camera data as described in Romans (2003) and Wu et al. (2006). Their results showed that the standard SCA1B data was erroneous due to an incorrect implementation of the star camera processing routines. Systematic errors in the star camera data were reduced significantly. The differences between the recovered gravity field from the SCA1B star camera data and the reprocessed star camera data were in millimeters in terms of geoid height. The reprocessed data is also used in this work to analyze the range-rate residuals with respect to attitude errors.

Ko and Eanes (2015) further investigated the star camera errors' impact on the gravity field solutions by experimenting with different filter bandwidths applied during star camera data processing (L1A to L1B processing) and compared their results with the correct implementation of the star camera data combination as presented by Bandikova and Flury (2014). The comparisons showed that the correctly implemented star camera data combination based gravity field solution was the best among all.

Inácio et al. (2015) has studied the attitude errors and their impact on the gravity field in order to compute the budget of the attitude errors. The study showed that the attitude errors were dominant in the frequency band of 3 - 10 mHz. This band is also important for the GRACE gravity field solutions as most of the geophysical signals lie in the same range. Hence, the authors concluded that an improvement in attitude would improve the accuracy of the gravity field.

Harvey (2016) investigated the entire star camera data processing software onboard GRACE and concluded that there are bugs even in the onboard star camera processing software. The stellar aberration correction applied to the star camera quaternions was computed on the basis of the ECEF velocity rather than the ECI velocity. This produces twice-per-revolution inter camera biases. The once-per-revolution star camera noise was found to be dependent on the number of stars in the field-of-view of the star cameras along with the thermal conditions of the spacecraft. For details see Harvey (2016). As a result of these findings, the reprocessing of star camera data including the combination of star camera data with the angular accelerations from the accelerometers has been decided by JPL, NASA. The reprocessed attitude data (SCA1B) and antenna phase center offset corrections (KBR1B) will be provided as version 3 L1B data product.

On the basis of the previous work, the following reasons for the limited accuracy of the star camera based attitude solution have been found:

(1.) In one GRACE spacecraft, there are two star cameras mounted on each of the lateral sides of the spacecraft (see Fig. 4.9). Ideally they both should provide attitude information of the satellite at any instant of time but, due to the orbital configuration, there are time periods when one of the star cameras is blinded by Sun for a period of 161 days and by Moon for every 26 days. These effects are called as *Sun and Moon intrusions*. Examples are given in Fig. 3.4 (D). Thus,

one of the main limitations is the unavailability of the data of both star cameras simultaneously. Due to the periodic blinding of one of the star cameras by Sun or Moon, attitude is obtained from one star camera only for significantly large periods of time.

Star camera data (SCA1B) is computed by an optimal combination of the data of the two star cameras (Romans, 2003) (here, they are referred to as *head#1* and *head#2*). But due to the intrusions there are periods when the data of only a single star camera is available, hence no combination is possible. The disadvantage of the single star camera solution is that it suffers from anisotropic errors (especially in the pitch and yaw axes) which increases the errors in the attitude observations. The combined solution from the two star cameras reduces these errors significantly, hence, increases the accuracy of the attitude observations (Bandikova, 2015).

(2.) As mentioned by Herman et al. (2004), another limitation of the star camera based attitude solution is the different accuracies of each of the two star camera heads. The accuracy of the attitude reduced when it is estimated from the less accurate single star camera head ('worst'). However, the accuracy of the 'worst' star camera head did not reach below the mission requirements. Bandikova (2015) analyzed the performance of each star camera head for the year 2008 and showed that on both satellites, the accuracy of star camera *head#2* was better than *head#1*. The accuracy analysis was performed for four star camera heads. The measurement accuracy was measured as the mean noise level of rotation about the star camera frame axis (ϵ_x , ϵ_y and ϵ_z) in the frequency band 0.1 - 0.5 Hz. Their comparison is shown in Table 3.1. Note that the nominal accuracy for x and y axes was $30 \mu\text{rad}$ and for z axis, it was $240 \mu\text{rad}$.

Overall, their performance was better than the mission requirements but when compared with each other, one head of each spacecraft was better than the other despite of their similar constructional geometry. Generally, the performance of the star cameras in the direction of the roll axis is precise. However, the accuracy of the pitch and yaw axes is affected most due to the differences in the accuracies of the two star cameras. Variations in the pitch angles of the two GRACE satellites for the year 2007 and 2008 are shown in Fig. 3.4 (B). Similar are the variations on the yaw angles, thus, they are not shown here. The systematic effects dependent on the differences in the accuracy of the star camera head can be seen in the pitch angle

Table 3.1: *Measurement accuracy of two star camera heads onboard GRACE-A and GRACE-B during 2008 as investigated by Bandikova (2015). Accuracies are given in the star camera frame of reference.*

	ϵ_x (μrad)	ϵ_y (μrad)	ϵ_z (μrad)
GRACE-A			
<i>head#1</i>	25	18	235
<i>head#2</i>	25	22	170
GRACE-B			
<i>head#1</i>	32	32	240
<i>head#2</i>	20	14	140

while comparing the panel (B) and (D) of Fig. 3.4.

(3.) Besides these two major error sources, the star camera performance is also affected by the onboard satellite maneuvers such as Center of Mass calibration (CoM), heating set point related switching events which are referred to as DSHL events (Kruizinga, 2004), and the attitude control activation events from the thrusters and magnetic torquer currents. Comparison of the plots (A) and (B) of Fig. 3.4 reveal the impact of high thruster activities on the pitch angle observations, for example, between day 500 and 600 on GRACE-B and from day 350 to 500 on GRACE-A. The pitch angle is mainly controlled by the currents flowing through the three magnetic torquer rods. The roll and yaw angles are mainly controlled by the thrusters as they are difficult to control by the magnetic torquer rod currents at the places where the magnetic field lines are parallel to the these pointing axes (Bandikova et al., 2012). Therefore, effects related to strong variations in the magnetic torquer rod currents (shown in Fig. 3.3) are also affecting the pitch variations. The current variations in magnetic torquer rods depend on the active star camera head. That is why the period of 161 days of similar current variations is seen in Fig. 3.3.

As shown by Bandikova and Flury (2014), the combination of the data of two star camera heads reduces the errors in attitude significantly. Thus, with the idea of combining all available attitude information, further approaches were developed to combine the data from other attitude sensors. For example, the IMU provides angular rates, the accelerometer provides angular accelerations along with the linear accelerations. The information from these two sensors can be combined with that

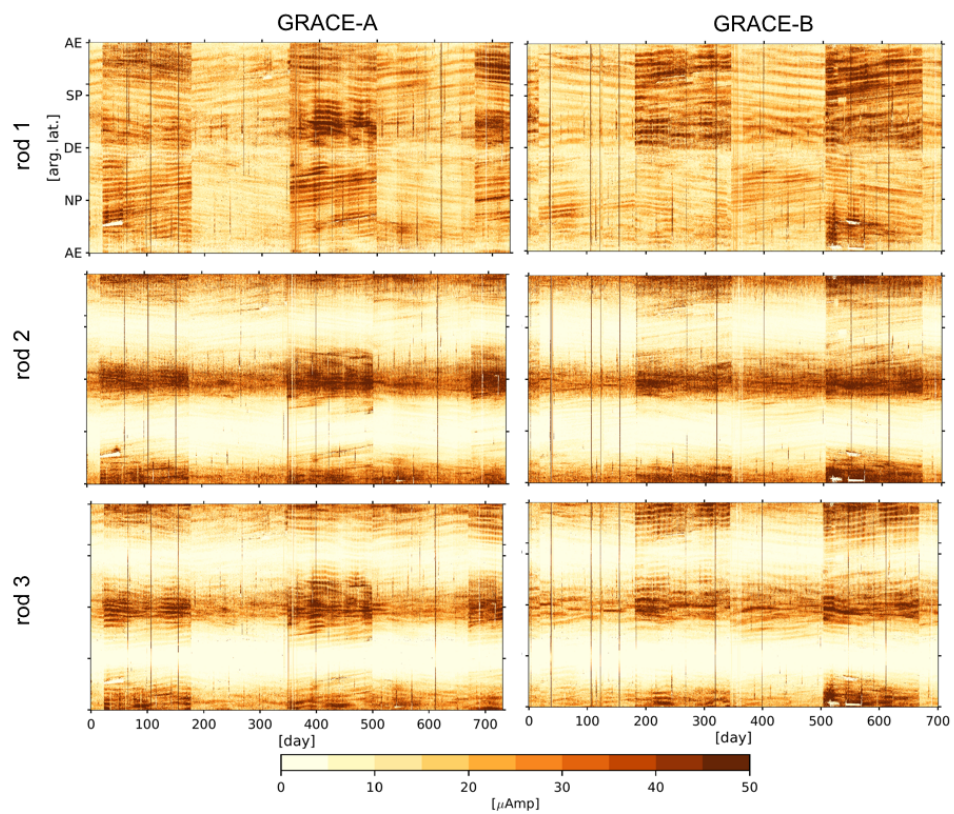


Figure 3.3: *Absolute magnitude of the magnetic torquer currents in the three rods of GRACE-A and GRACE-B in 2007 and 2008.*

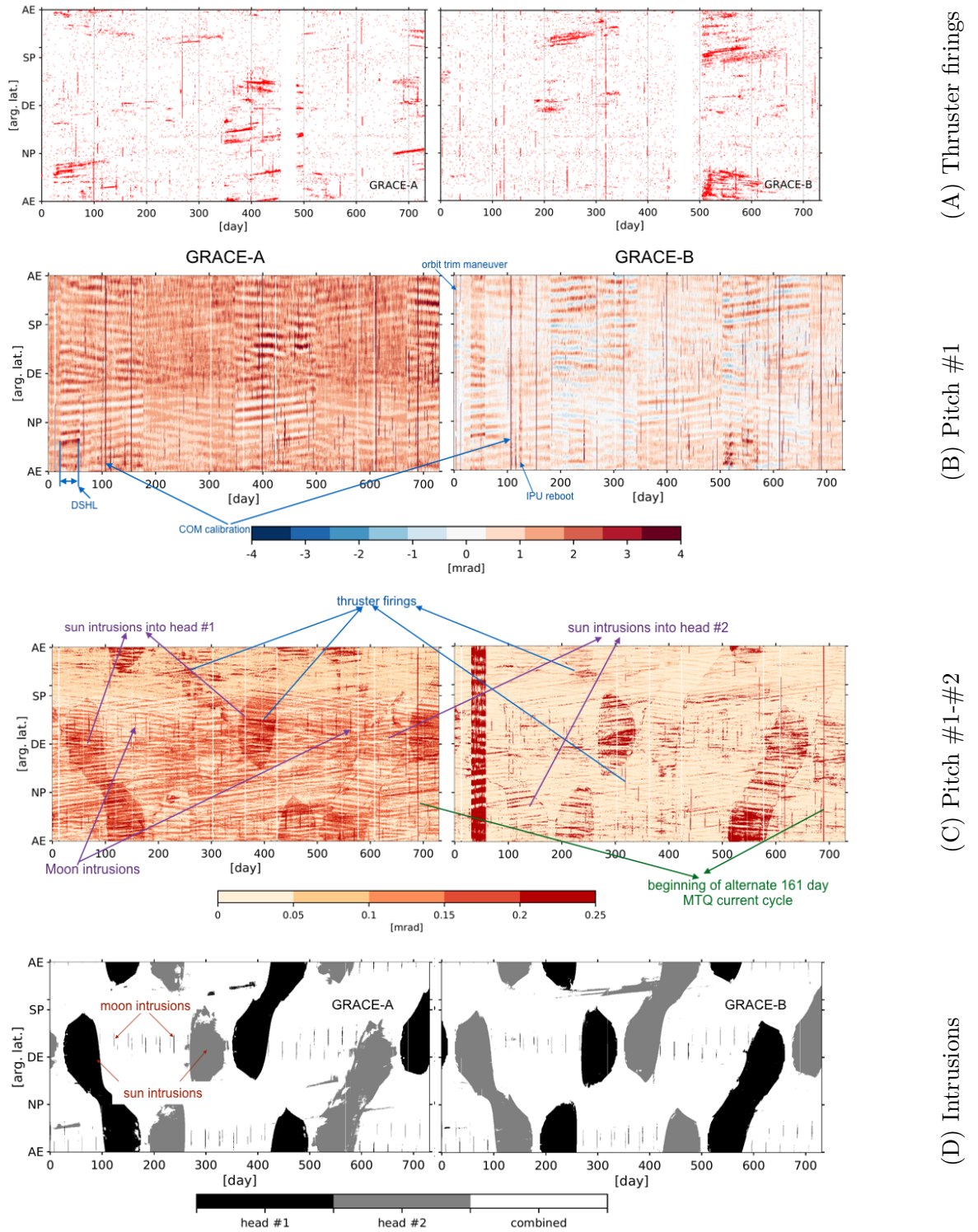


Figure 3.4: An illustration of pointing variations in (B) and the effects of the attitude control sensors (A) on them in 2007 and 2008. In (C) differences between the pitch angles from data #1 and #2 are shown (cf. Table 3.2) along with their dependency on the star cameras availability shown in (D).

of the star camera quaternions to get improved attitude data. Unfortunately, IMUs failed 1.5 hours after launch of the satellite, so their data is not available, but angular accelerations from the accelerometers are available (Dunn et al., 2002).

Klinger and Mayer-Gürr (2014) attempted to combine the star camera data with the angular accelerations from the accelerometers and investigated its impact on the gravity field solutions (ITSG-2014) computed up to degree and order 90. Their results showed slight improvements in geoid height for degrees above 30. The replacement of the SCA1B data by the combined attitude data was one of the many improvements in the ITSG-2014 processing chain. The other improvements were outlier detection and removal from the accelerometer data, updated background models, covariance modeling of noise and co-estimation of daily solutions up to degree and order 40. Therefore, it is difficult to say whether the improvement was mainly achieved by the combined attitude data or by the overall contribution of all above mentioned processing steps in the parameter estimation. This fused attitude data has been used in computing the gravity field model ITSG-2014, the residuals of which are used in this work. Thus, this data is analyzed in this work for the identification of attitude errors in the range-rate residuals. The reprocessed attitude data computed by Klinger and Mayer-Gürr (2014) was estimated from the combination of star camera quaternions and angular accelerations using a least squares variance component estimation approach. Since the attitude is obtained by combining or fusing together the two different datasets, it is also called fused attitude dataset.

The attitude errors are analyzed by comparing the pointing angles computed from two different attitude datasets. As mentioned earlier, the error models of the star camera are unknown till today. Thus, it is difficult to analyze their errors. By taking advantage of reprocessed attitude results and comparing them, the characteristics of errors in the attitude datasets as well as in the residuals are studied in this thesis. Here, the used attitude datasets are JPL provided star camera attitude (SCA1B) which is represented as #1 and the fused attitude data which is represented as #2 (also listed in Table 3.2). The pointing angles are computed from both of them as explained in Appendix A. The comparison between the pointing angles show that the differences between the roll angles are very small as compared to the pitch and yaw angles (cf. Fig. 3.5). It is due to the fact that the roll angles obtained from the star cameras are very precise and their variations remained mostly within

Table 3.2: *Description of different attitude datasets used in this thesis. For details see text.*

Attitude data set	Description
#1	SCA1B (Standard JPL Product)
#2	SCA1B combined with angular accelerations of ACC1B
#3	Reprocessed SCA only attitude at IfE, Hannover
#4	Reprocessed SCA (#3) combined with angular accelerations of ACC1B

the dead band limits. On the other hand, pitch and yaw angles are less precise, hence their differences are large (cf. Fig. 3.5). The differences between the pitch

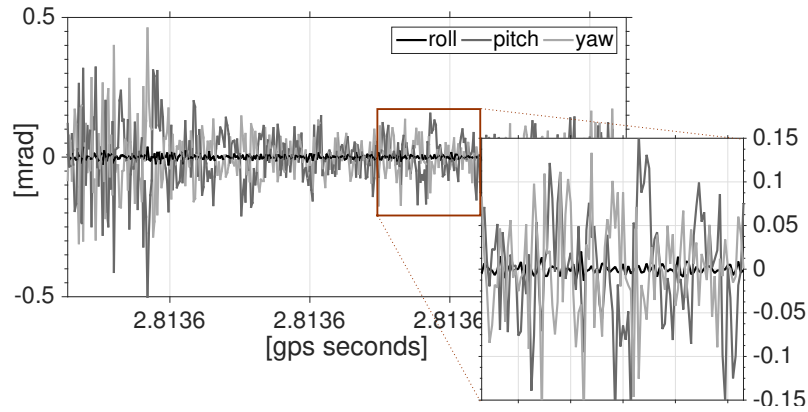


Figure 3.5: *Differences between roll, pitch and yaw angles of GRACE-A computed from attitude dataset #1 and #2 plotted for 5 minutes of December 1, 2008. Zoom-in plot shows differences for 1 minute.*

angles computed from two datasets are shown in Fig. 3.4 (C) for the two years 2007 and 2008. Their differences show the overall performance of the fused attitude data. For the time when the primary camera (*head#1*) was blinded and data from the secondary camera was used (see panel (4) of Fig. 3.4 for active star camera heads), high differences in the pitch angles indicate the significant improvements from the fused attitude data. When the data from the primary star camera was available and the secondary camera was blinded, the accuracy of the two pitch angles is equivalent as the differences are very small between the two. It means, the more accurate star camera leads to the smallest noise level in the attitude combination as compared to the combination with the less accurate star camera. The differences also indicate

improvements due to fused attitude during the times when thrusters were fired for attitude control.

These differences in the two pointing angles indicate the attitude errors which are reduced by using the fused attitude data. These errors propagate to the range measurements through AOC and linear accelerations and affect their precision. The details are studied in the following section.

3.3 Attitude error propagation into the range-rate observations

The attitude information is used in the data preprocessing for global gravity field parameter estimation. The KBR antenna phase center offset corrections (AOC), GPS phase center corrections, rotation of the linear accelerations of the accelerometers from Science Reference Frame (SRF) to ECI reference frame require attitude information. Therefore, the attitude errors are likely to be propagated through these observations. Here, the impact of attitude on the KBR AOC and on the linear accelerations of the accelerometers are investigated.

3.3.1 Error propagation via antenna offset corrections

The range-rate AOC are provided in the KBR1B data along with the range and range-rate observations. In the ITSG-2014 solutions, the AOC are computed as

$$\begin{aligned} \text{AOC} &= |\mathbf{PhC}| \cos \theta \\ &= [\mathbf{e}_{AB} \cdot (\mathbf{R}_{(\text{SRF} \rightarrow \text{ECI}),A} \mathbf{PhC}_A)] - [\mathbf{e}_{AB} \cdot (\mathbf{R}_{(\text{SRF} \rightarrow \text{ECI}),B} \mathbf{PhC}_B)], \end{aligned} \quad 3.1$$

where \mathbf{e}_{AB} is the normalised satellite position vector of GRACE-A w.r.t. GRACE-B. Angle θ is the angle between the line joining the satellite's center of mass and the line joining the K-band antenna horn as shown in Fig. 3.2. \mathbf{PhC} is the phase vector (provided in the VKB1B product) which has a length of ≈ 1.47 m for each satellite. $\mathbf{R}_{(\text{SRF} \rightarrow \text{ECI})}$ is the matrix representing the rotation from SRF to ECI frame of reference. The rotation matrix is computed from the attitude quaternions as given in Eq. A.6 of Appendix A.

The two sets of AOC re-computed from the two attitude datasets, namely #1 and #2, are compared by computing differences between them (see Table 3.2 for details). In Fig. 3.6 (a.) the comparison of the time-series of the two AOC and their differences show the reduction in high-frequency noise in AOC#2. The differences are large when attitude #1 is computed from the single star camera head solution whereby they are small when attitude #1 is computed from both star camera heads.

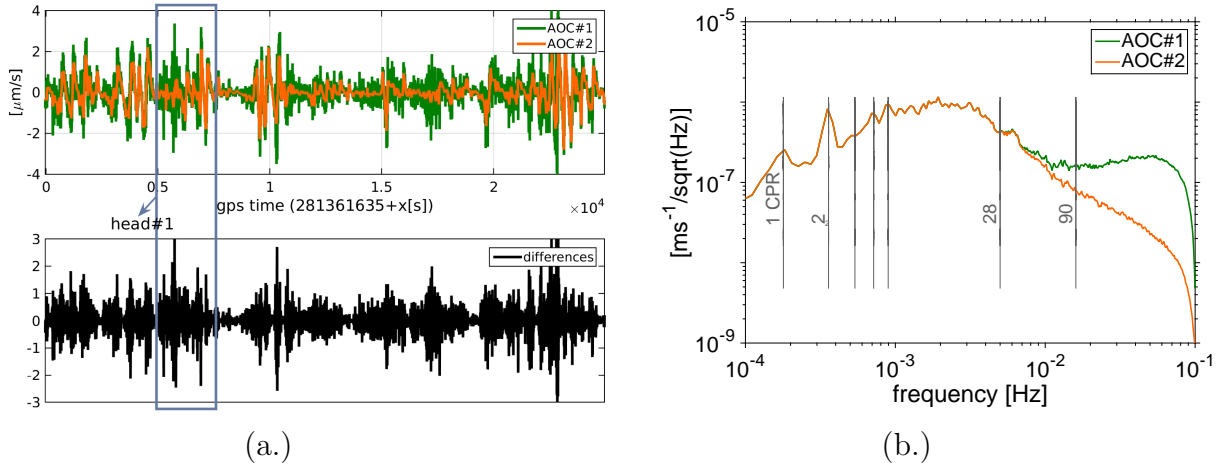


Figure 3.6: (a.) In the upper panel, AOC computed from SCA1B data #1 and fused data #2 are shown for 3 revolutions on December 1, 2008. The reduced high-frequency noise in AOC #2 is the reason for the large differences between the two shown in the lower panel. The high-frequency noise reduces specifically where the SCA1B is obtained from just one star camera head. Blue box highlighting ‘head#1’ in both panel shows that the head#1 was blinded during this time and SCA1B attitude is obtained from head#2 only. (b.) PSDs of the two AOC show that the AOC#2 has reduced high-frequency noise above 5.5 mHz or 28 CPR.

It means, the combination with the angular accelerations is like adding additional attitude information which reduces the errors due to inaccuracies in a single star camera solution. The PSDs of two AOC in Fig. 3.6 (b.) show that the AOC computed from the attitude data #2 significantly improves the observations above a frequency of 5.5 mHz. This is due to the better precision of the angular accelerations in high frequencies where the star cameras are limited.

The precision of the AOC is mainly affected by the imprecise pitch and yaw axes. They both are improved for frequencies above 5.5 mHz (28 CPR) when fused attitude data is used. For example, a comparison between the PSD of roll, pitch, yaw angles

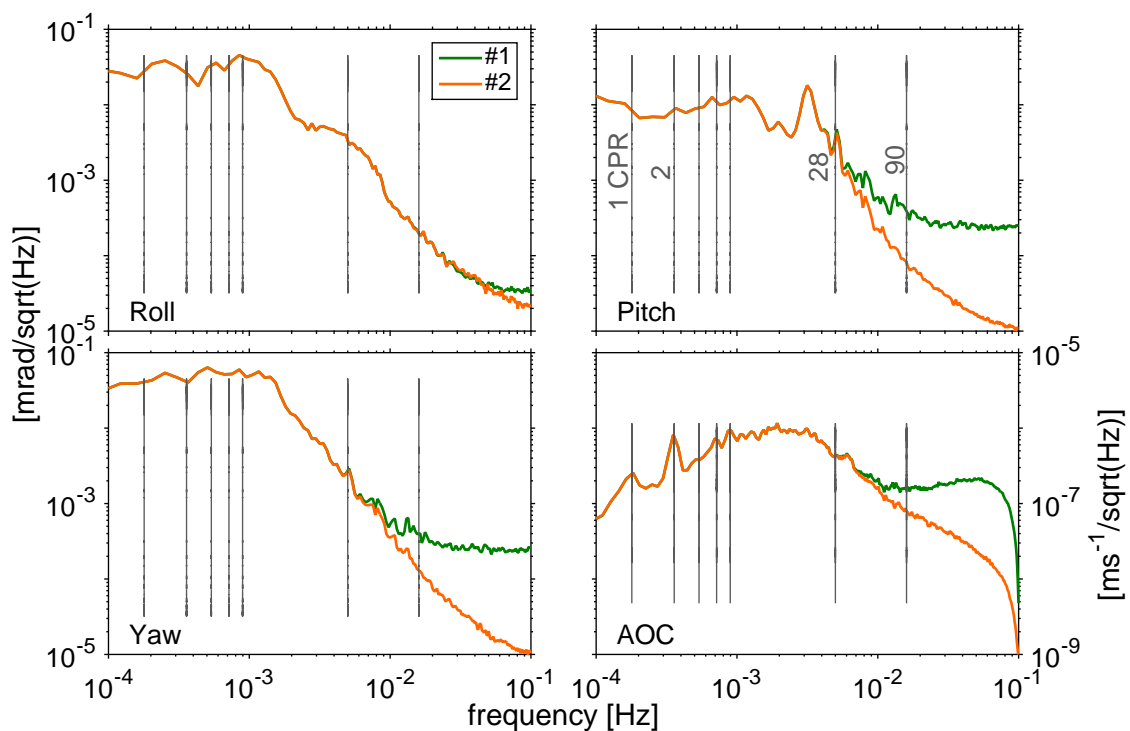


Figure 3.7: *PSDs of pointing angles compared with the AOC for December 1, 2008. They show the clear improvement in pointing along the pitch and yaw axes from attitude data #2, also improving AOC#2. The high-frequency noise is reduced above 5.5 mHz or 28 CPR due to the combined angular accelerations.*

and the AOC in Fig. 3.7 shows that the pitch and yaw angles both are improved due to attitude data #2 in frequencies above 5.5 mHz. Similar effects can be seen in the PSD of the two AOC. The roll axis measurements are already precise from the star camera only attitude. Thus there is only slight improvement in the frequencies above 50 mHz (Goswami et al., 2018b).

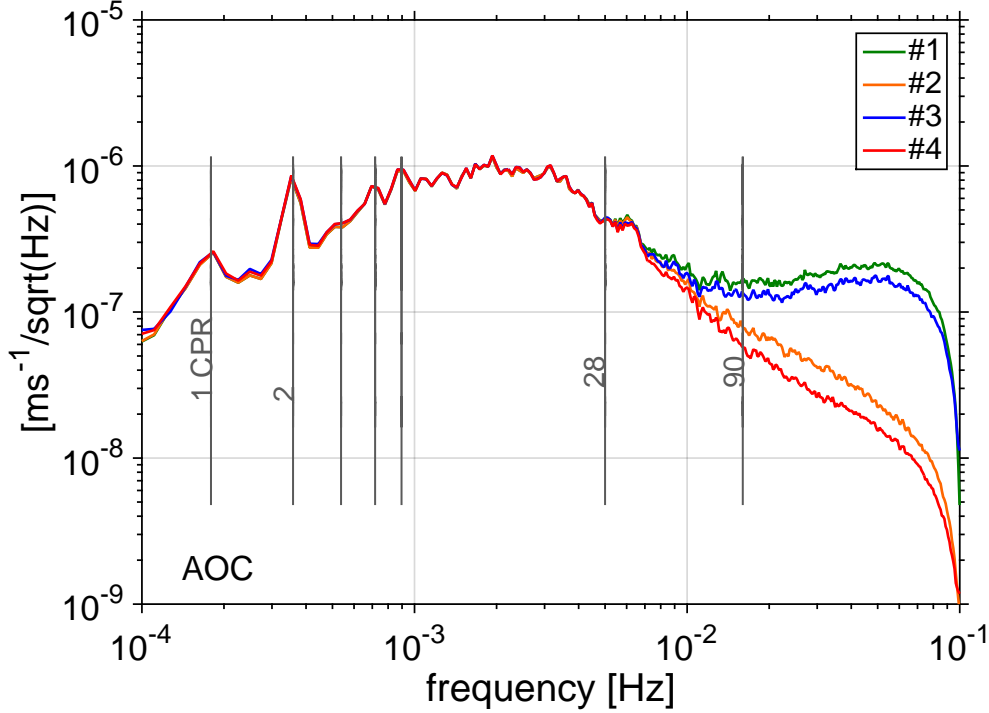


Figure 3.8: Comparison of the AOC based on the four attitude datasets for December 1, 2008 (cf. Table 3.2). The PSDs start to deviate after 28 CPR where deviations are significantly large after 112 CPR.

Similarly, the four AOC are computed for each attitude case as described in Table 3.2 and compared together for December 2008. Their PSDs (cf. Fig. 3.8) indicate the spectral behavior of all four cases. As mentioned in section 3.2, the attitude product SCA1B (#1) provided by JPL contains high anisotropic errors due to the implementation of an incorrect combination algorithm. The use of the correct combination algorithm improves the star camera attitude by minimizing its anisotropic errors. This correctly combined star camera data product is #3 here which reduces the high-frequency errors in the AOC measurements as compared to attitude #1.

The fusion of the correctly combined star camera attitude (#3) with the angular accelerations leads to a further significant reduction of high frequency errors in the AOC measurements. The AOC product #4 benefits significantly from the improved pitch and yaw axes information.

3.3.2 Error propagation via linear accelerations

The attitude errors are also likely to be propagated through the linear acceleration observations from the accelerometers. The linear accelerations provided in the ACC1B product are given in the SRF. They are rotated into the ECI frame of reference as

$$\begin{pmatrix} \ddot{x}_i \\ \ddot{y}_i \\ \ddot{z}_i \end{pmatrix}_{\text{ECI}} = \mathbf{R}_{\text{SRF} \rightarrow \text{ECI}} \begin{pmatrix} \ddot{x}_i \\ \ddot{y}_i \\ \ddot{z}_i \end{pmatrix}_{\text{SRF}}, \quad 3.2$$

where $i \in \text{GRACE-A, GRACE-B}$, $(\ddot{x}, \ddot{y}, \ddot{z})$ are the linear accelerations along the three axes and $\mathbf{R}_{\text{SRF} \rightarrow \text{ECI}}$ is the rotation matrix computed from attitude quaternions (Eq. A.6 of Appendix A). These linear accelerations in the ECI reference frame are used to reduce the effects of non-gravitational accelerations from the range-rate observations (see Eq. 1.1).

A comparison of the impact of the two attitude datasets (#1 and #2) on the individual accelerations from GRACE-A and GRACE-B is shown in Fig. 3.9. The linear accelerations shown in the Fig. 3.9 are given in the ECI frame of reference rotated using attitude data #1 and #2, respectively. The two sets of linear accelerations show very small impact of the different attitude results in their PSDs, mostly at very high frequencies (above 10/20 mHz).

The PSDs of their differences highlight the contribution of attitude errors into each axis of both accelerometers. The differences are compared with the expected sensor noise level for those individual axes (shown as ‘Error model’ in Fig. 3.9). Differences in the y -axes accelerations are always below or at the sensor noise level meaning that the impact of attitude errors on the y -axes is not significant. The differences in the x - and z -axes of GRACE-B accelerations are also lower than the noise level at frequencies below 3.5 mHz whereas the differences are higher almost by a factor of 10 at frequencies above 3.5 mHz. The differences in the x -axes of GRACE-A are always above the noise level and are significantly large at frequencies

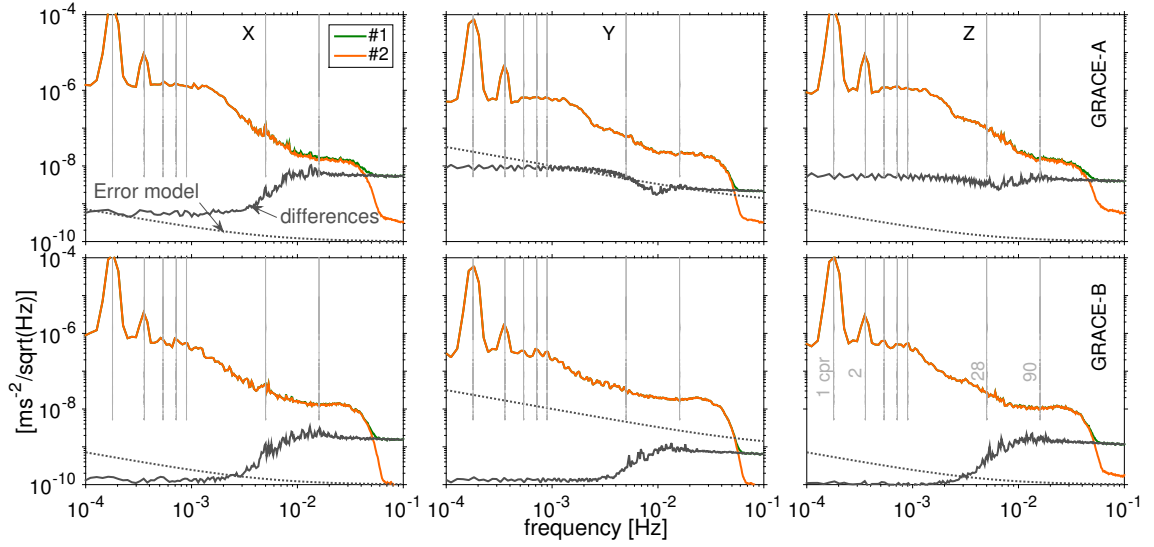


Figure 3.9: Comparison of the PSDs of the two sets of linear accelerations in the ECI frame of reference rotated using attitude #1 and #2 for December 1, 2008. In each case, differences are visible at very high frequencies (> 70 mHz) only. Also their differences are shown and compared with the noise models of corresponding axes.

above 3.5 mHz. Among all, the differences in the z -axes of GRACE-A are significantly higher, almost a factor of 10 at low frequencies and even more in high frequencies. Note that the large differences in the frequencies above 30 mHz does not affect the gravity field models because the accelerometer data is high-pass filtered above that frequency. However, large differences in the frequency range 3 to 10 mHz indicate that the attitude errors propagated through the accelerometer are also present in the range-rate observations along with the ones which are propagated through AOC. This is another reason behind the large differences between the sensor noise level and the current level of the range-rate residuals. Similar results are obtained for the four attitude datasets.

Improvements in the linear accelerations due to the attitude merely affect the global gravity field solutions computed up to degree and order approximately 100. It is due to two main reasons: first, as mentioned above, the accelerometer data is high-pass filtered and hence there remains no signal or error to be propagated to the range-rate observations. Second, in high frequencies, the GRACE is limited primarily by the system noise of the K-band microwave ranging system (see Chapter 4 for details). Thus, an impact due to the improved linear accelerations can hardly be seen.

3.4 Post-fit residual analysis with focus on attitude errors

In this section, the analysis of post-fit range-rate residuals is presented with focus on attitude errors which have been described in the previous sections. The analysis of the postfits discussed here is based on the two attitude data sets i.e., #1 and #2 (see Table 3.2 for data description). In order to analyze the attitude error characteristics in the post-fit residuals, first, monthly gravity field solutions are computed for each month of 2007 and 2008, along with their residuals. One set of solution and residuals is computed using the ITSG-2014 processing chain with the star camera product SCA1B, i.e. #1. Another set is computed using the fused attitude product #2. The processing chain of ITSG-2014 gravity field models is described in Chapter 1. The two sets of residuals computed from attitude data #1 and #2 are represented as $\hat{e}_{\#1}$ and $\hat{e}_{\#2}$. Second, the two sets of post-fit residuals are analyzed for each month. Since the post-fit residuals are obtained using the full processing chain of gravity field parameter estimation, it is possible that the attitude errors investigated in Section 3.3 may be absorbed by the estimated parameters. Otherwise, the range-rate residuals must contain them.

Analyzing the residuals ($\hat{e}_{\#1}$ and $\hat{e}_{\#2}$) by comparing their PSDs as shown in the upper panel of Fig. 3.10 indicates small differences between them. The differences are visible in the frequency range of 5.5 - 60 mHz (28 - 335 CPR). The frequency 5.5 mHz is related to AOC (as shown in the lower panel of Fig. 3.10). The AOC are significantly improved in the frequencies above 5.5 mHz when using the attitude data #2. The improvement is largely due to the reduced high-frequency noise in the pitch and yaw angles beyond this frequency. The PSD of the differences of the residuals $\hat{e}_{\#1}$ and $\hat{e}_{\#2}$ indicates the contribution of attitude errors (shown in the upper panel of Fig. 3.10). The differences are mostly below the sensor noise level except in frequencies between 5.5 to 20 mHz. The high differences in residuals between frequency 5.5 to 20 mHz come from the differences between the two set of AOC as shown in the lower panel of Fig. 3.10. The frequencies 5.5 and 20 mHz are highlighted with a red color arrow. It indicates that the attitude errors are largely propagated through the AOC. However, the proportion of errors propagated through

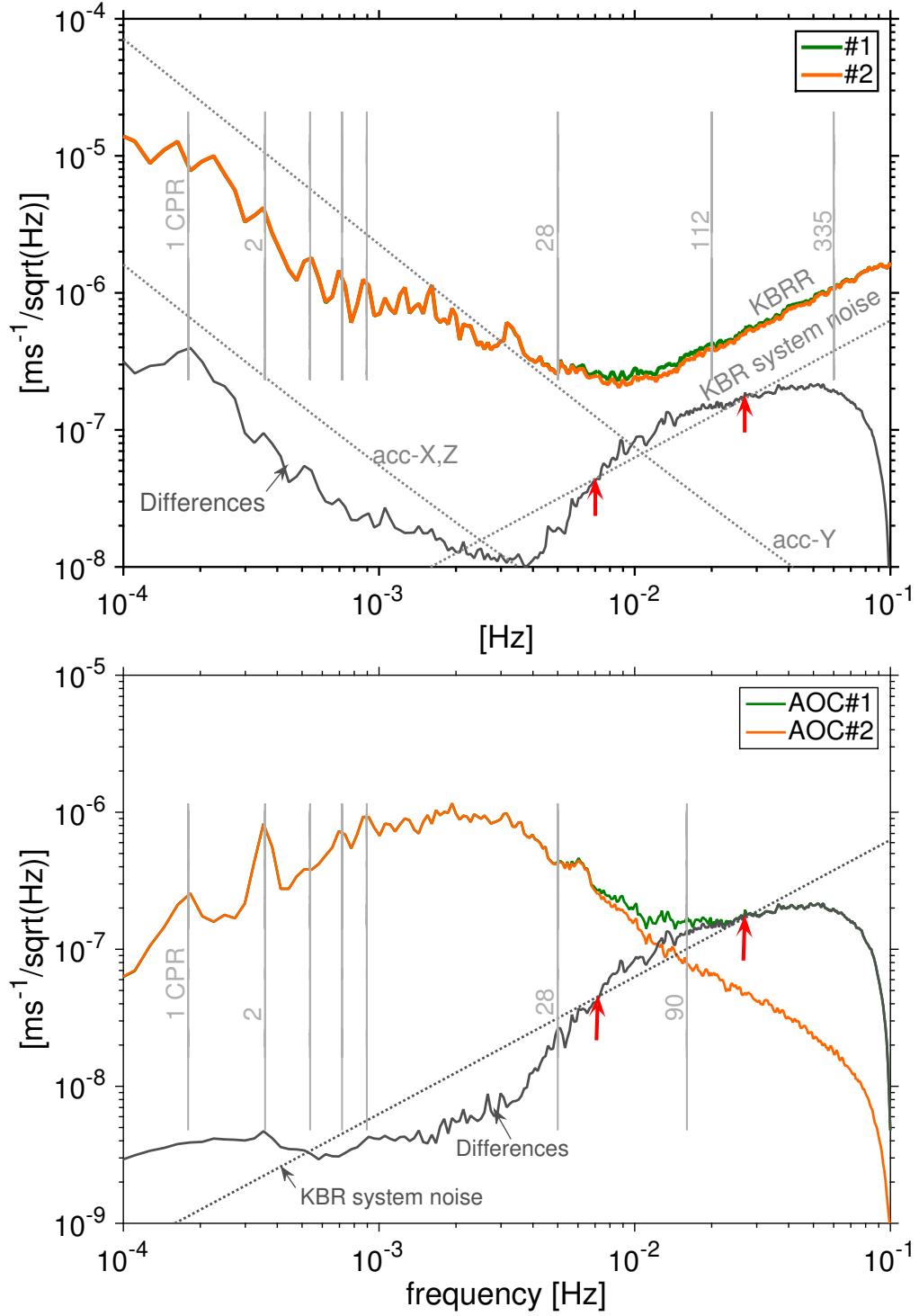


Figure 3.10: Upper panel: PSDs of post-fit residuals ($\hat{e}_{\#1}$ and $\hat{e}_{\#2}$) compared with the KBR and ACC noise models for December 2008. Lower panel: AOC from the attitude data ($\#1$ and $\#2$). The two PSDs of the residuals deviate at 5.5 mHz where the two AOCs deviate as well. This behavior indicates that attitude errors in the residuals propagate through AOCs.

the accelerometers can not be ignored as they are also prominent in this frequency band. But, no significant contribution of attitude errors propagated from linear accelerations are seen in the low frequencies. For example, large differences are seen in the low frequencies of x - and z -axes of the linear accelerations but the attitude errors in low-frequency residuals are below the sensor noise level (cf. Fig. 3.9).

As seen in the upper panel of Fig. 3.10, both PSDs are dominated by the accelerometer and K-band instrument noise on both ends. The magnitude of the residuals in the frequency range (5.5 - 60 mHz) where attitude data effects are visible, is very small compared to the accelerometer and K-band instrument noise. It renders it difficult to analyse the attitude errors propagated into those frequencies. Thus, the differences between residuals $\hat{e}_{\#1}$ and $\hat{e}_{\#2}$ are more appropriate to study the attitude errors present in them. Their differences would reduce all the accelerometer and KBR instrument noise from the residuals and highlight the attitude errors propagated to the residuals. But these differences can indicate the propagated attitude errors only if they are not absorbed by the estimated parameters (monthly gravity field parameters, daily orbit state parameters, periodic accelerometer scale and bias). Thus, the differences will indicate whether the attitude errors are propagated to the gravity field parameters or not.

The differences are analyzed on the argument of latitude and time plots as they are helpful in getting knowledge on the attitude error characteristics propagated into the post-fit residuals. Absolute differences between the residuals $\hat{e}_{\#1}$ and $\hat{e}_{\#2}$ are computed and compared with differences between the two sets of AOC in Fig. 3.11. It is interesting to note that the magnitude of the differences between the two AOC and the post-fit residuals is the same. It indicates that a large amount of attitude errors which propagate through the AOC measurements ends up in the post-fit residuals. Thus, their impact on the gravity field solutions must be negligible as they are not absorbed by the gravity field parameters, i.e. Stokes coefficients. The differences are large during the time when one star camera head was blinded by Sun and Moon intrusions in any of the two GRACE satellites. Note that the residual differences and the AOC differences contain pointing errors from the two GRACE satellites. The post-fit residuals also show the effect of pointing inaccuracies due to the availability of star camera heads with different accuracies. Analysis of the differences in the argument of latitude and time domain helps to understand the physical error characteristics

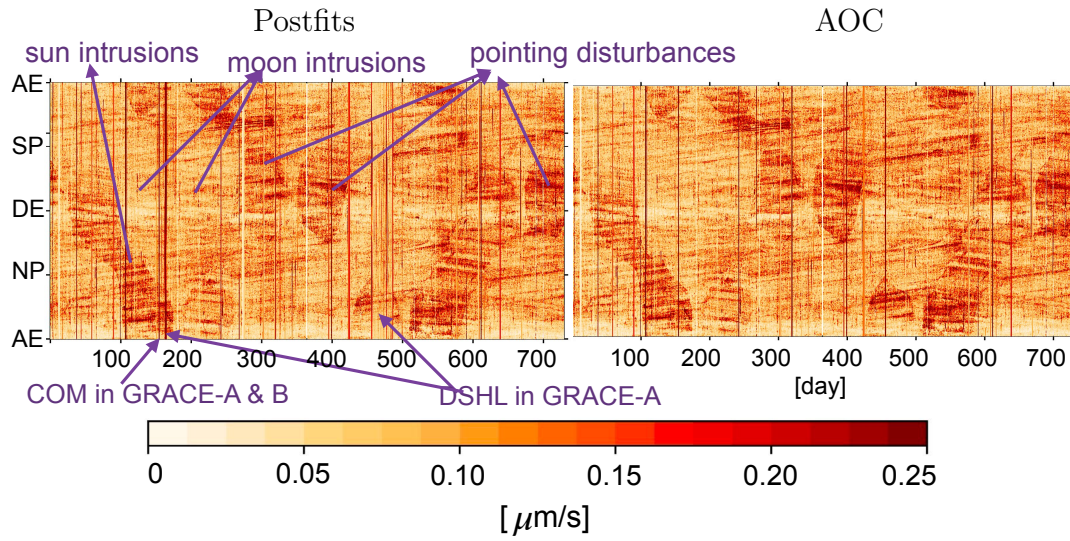


Figure 3.11: The absolute differences in $\mu\text{m/s}$ between range-rate residuals ($\hat{\mathbf{e}}_{\#1}$ and $\hat{\mathbf{e}}_{\#2}$) and the two sets of AOC ($\text{AOC}_{\#1}$ and $\text{AOC}_{\#2}$). Differences are shown for 2007 and 2008.

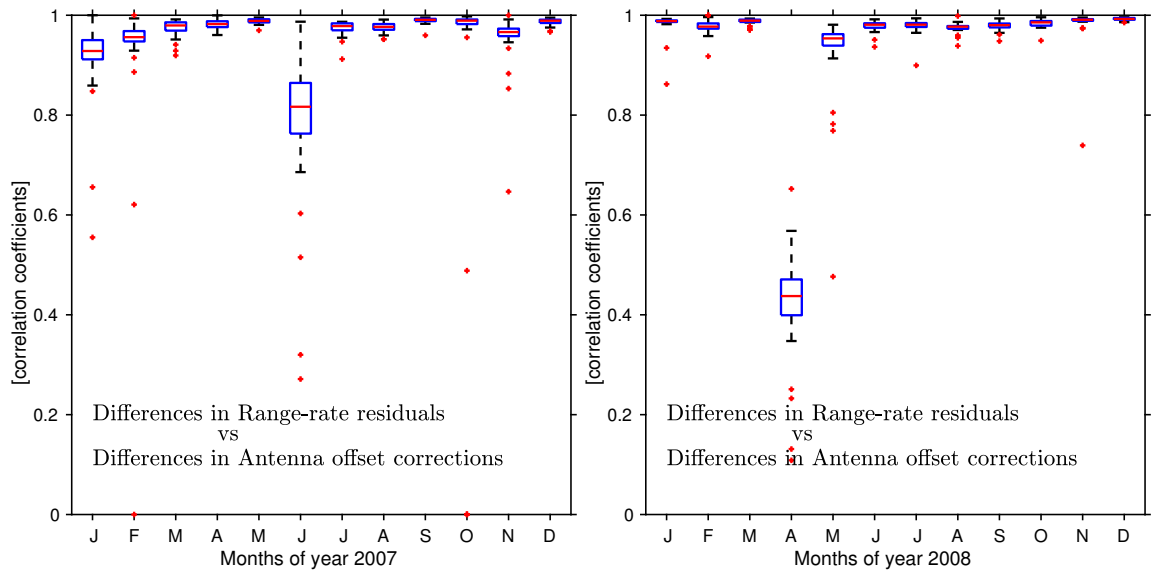


Figure 3.12: Monthly box plots showing the correlations between the two plots shown in Fig. 3.11 for the two years.

of the data. These errors are related to the differences between single star camera solutions, effects of attitude control sensors on the observations, etc. The error characteristics are illustrated in Fig. 3.11. It shows that a large amount of attitude related systematic errors are part of the residuals. Also, correlation coefficients are computed once per day, shown in Fig. 3.12 for each month of 2007 and 2008. The strong correlations between the differenced residuals and AOC also indicate that the major attitude error contributors to the range-rate observations are AOC and most of the attitude errors end up in the range-rate residuals (Goswami et al., 2018b).

Tamara Bandikova shared the attitude product #3 for December 2008 (Bandikova and Flury, 2014). The gravity field solutions were computed using this dataset and fusing this star camera data with angular accelerations from the accelerometer. The attitude product was combined and provided by Beate Klinger (TU Graz) which is referred to as #4 in this thesis. The individual sets of residuals (\hat{e}_3 and \hat{e}_4) are ob-

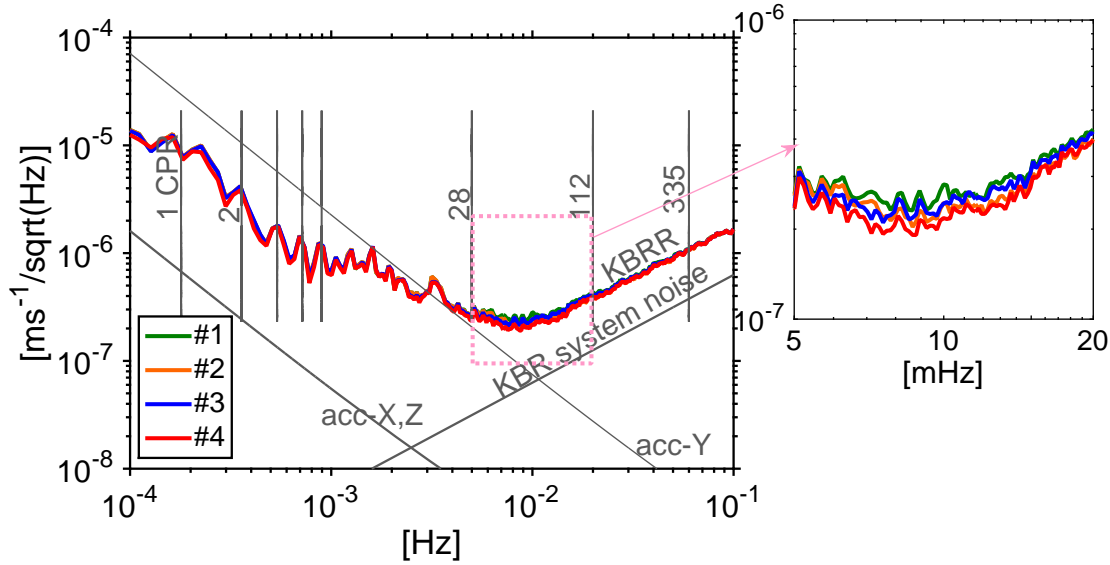


Figure 3.13: *PSDs of the post-fit residuals $\hat{e}_1, \hat{e}_2, \hat{e}_3, \hat{e}_4$ for December 2008. The four sets of residuals are compared with the accelerometer and K-band system noise models. Differences in the frequency range 5 - 20 mHz are shown as zoom-in plot in the side panel.*

tained by replacing only the attitude product in the gravity field processing chain. When the PSDs of four sets of residuals are compared together, they all indicate noticeable differences between 28 and 112 CPR (see Fig. 3.13). It means that atti-

tude errors in GRACE are largely present in the frequency range 5.5 - 10 mHz or 28 - 112 CPR.

3.5 How do attitude errors affect gravity field solutions?

In the previous sections, the error characteristics of the GRACE attitude has been discussed. The GRACE attitude errors are amplified in the pitch and yaw directions, especially in cases where the data from only one star camera head is available. These pitch and yaw errors propagate to the range-rates through the antenna offset corrections along with the linear accelerations.

In this section, the impact of the identified errors in the post-fit range-rate residuals on the gravity field solutions are investigated. It is quantified in closed loop simulation scenarios. Note that the star camera errors are not modeled, but the post-fit range-rate residuals are utilized here to determine the impact of attitude errors on the gravity field solutions. The attitude errors are computed by subtracting the two sets of residuals because it is helpful in separating them from the rest of the dominating errors in the residuals. The monthly gravity field solutions are computed for each month of 2007 and 2008.

3.5.1 Simulation scenario

The impact of the identified attitude errors on the gravity field solutions is investigated in closed loop simulation scenarios considering different cases.

Case 1: Gravity field solutions are computed with noise added to the noise-free range-rate observations ($\dot{\rho}$). The magnitude of the noise added to the observations is given in Table 3.3. The accelerometer noise and the ranging noise have spectral characteristics similar to the colored pink ($1/f$) and violet noise (f) (Keshner, 1982; Zhang and Schwarz, 1996). Thus, the colored noise terminologies are also used to refer to the noise of these instruments. The noisy range-rate observations ($\dot{\rho}_1$) are computed as follows:

First, the simulated pink noise representing the accelerometer noise is used to integrate the orbit. Then, the range-rates are computed from the integrated orbits

Table 3.3: *Description of the noise added to the observations in the simulation cases 1 and 2.*

Noise	noise type	magnitude of noise (σ)	units
orbit (\mathbf{r})	white noise	0.03	m
accelerometer	pink noise ($\sim 1/f$)		
	along-track	3×10^{-10}	m/s ²
	across-track	3×10^{-9}	m/s ²
	radial	3×10^{-10}	m/s ²
K-band ranging	violet noise ($\sim f$)	2.5×10^{-7}	m/s
star camera	white noise	5×10^{-5}	mrads

of both spacecraft. Simulated violet noise is added to the range-rates. The violet and the pink noise are derived by differentiating and double differentiating the white noise using a Charge Routing Network (CRN-) filter. White noise of the star camera is added via the simulated antenna center offset corrections. From the simulated orbits, kinematic orbits are derived by adding 3 cm positioning noise to each axis. The simulated noise in each case reflects the errors integrated over the relevant frequency bandwidth. Thus, the total noise ϵ contains the noise of orbit, star camera, ranging and the accelerometer noise. Hence the range-rate observations containing noise ϵ are represented as

$$\dot{\rho}_1 = \dot{\rho} + \epsilon. \quad 3.3$$

In order to determine the noise floor, different noise realizations were simulated which are denoted here as ϵ' for all noise sources mentioned in Table 3.3. The gravity field solutions are computed from the range-rate observations ($\dot{\rho}'_1$) containing different noise realizations each time,

$$\dot{\rho}'_1 = \dot{\rho} + \epsilon', \quad 3.4$$

where ϵ and ϵ' are obtained from the same noise distribution. Differences between

the gravity field solutions computed from different realizations define the noise floor which is plotted in *red* color in the left panel of Fig. 3.14.

In case 2, case 3 and case 4 which are discussed below, the differenced set of residuals are considered as the attitude errors. Differences are taken in order to extract the attitude errors from the post-fit range-rate residuals. As discussed earlier, these differences between the post-fit residuals computed from attitude dataset #1 and #2 reflect the attitude errors very well (cf. Fig. 3.11). Thus, they are considered as the error model and mapped on the gravity field solutions. The differences between various sets of residuals w.r.t. $\hat{\mathbf{e}}_{\#1}$ give the attitude errors with respect to the standard attitude data SCA1B, for example, shown in Table 3.4. The root mean square (RMS) values of the attitude errors for December 2008 show that the residual differences between $\hat{\mathbf{e}}_{\#1}$ and $\hat{\mathbf{e}}_{\#4}$ capture high attitude errors which are due to two reasons: incorrect implementation of the attitude data combination and large high-frequency errors which got reduced due to angular accelerations. Note that $\hat{\mathbf{e}}_{12}$ in Table 3.4 refers to the differences between post-fit residuals $\hat{\mathbf{e}}_{\#1}$ and $\hat{\mathbf{e}}_{\#2}$ and so on.

Table 3.4: *Statistical and physical description of the errors obtained from different sets of post-fit range-rate residuals for December 2008.*

Errors	RMS ($\mu\text{m/s}$)	origin of errors
$\hat{\mathbf{e}}_{12}$	0.0492	errors mainly of high-frequency star camera noise
$\hat{\mathbf{e}}_{13}$	0.1807	errors due to the incorrect data combination algorithm of star camera datasets
$\hat{\mathbf{e}}_{14}$	0.3814	combined errors due to incorrect data combination algorithm and angular acceleration errors due to its fusion

Case 2: The range-rate observations ($\dot{\boldsymbol{\rho}}_1$) computed in Eq. 3.3 for each month and the monthly set of differenced residuals are added together as

$$\dot{\boldsymbol{\rho}}_2 = \dot{\boldsymbol{\rho}}_1 + \hat{\mathbf{e}}_{12}.$$

3.5

67

The monthly set of residuals ($\hat{\mathbf{e}}_{12}$) is computed as

$$\hat{\mathbf{e}}_{12} = \hat{\mathbf{e}}_{\#1} - \hat{\mathbf{e}}_{\#2}, \quad 3.6$$

where $\hat{\mathbf{e}}_{\#1}$ and $\hat{\mathbf{e}}_{\#2}$ are the post-fit range-rate residuals obtained after gravity field estimation using star camera datasets $\#1$ and $\#2$, respectively. $\hat{\mathbf{e}}_{12}$ represents the attitude errors which are reduced due to the fusion of star camera data with the angular accelerations from the accelerometer.

The differences between the two gravity field solutions are computed using observations from case 1 and case 2 as

$$\begin{aligned} \delta C_{lm}^2 &= \left((C_{lm})_{\#1} - (C_{lm})_{\#2} \right)^2 \\ \delta S_{lm}^2 &= \left((S_{lm})_{\#1} - (S_{lm})_{\#2} \right)^2, \end{aligned} \quad 3.7$$

and, their geoid degree amplitudes are computed as

$$\begin{aligned} \text{geoid degree amplitudes} &= \delta\sigma_l \times R \text{ where,} \\ \delta\sigma_l &= \sqrt{\sum_{m=0}^l (\delta C_{lm}^2 + \delta S_{lm}^2)}. \end{aligned} \quad 3.8$$

R is the radius of the Earth. The geoid degree amplitudes are presented in the left panel of Fig. 3.14. The differences indicate the impact of the added attitude errors on the gravity field solutions. The differences are an order of magnitude below the predicted GRACE baseline, almost for all months of the years 2007 and 2008. Irregular differences are observed in the low degrees for all months. Possible reasons behind them could be due to *either* differences in the noise realizations used to compute the gravity field solution *or* due to the attitude errors added to them. In order to investigate these differences further, they are compared with the noise floor determined using Eq. 3.4. This comparison indicates that these differences are mainly caused by the different noise realizations added to the noise-free range-rate observations.

Further, two other sets of differences, $\hat{\mathbf{e}}_{13}$ and $\hat{\mathbf{e}}_{14}$, (case 3 and case 4) are also tested. The estimated gravity field solutions from the four cases are compared then for December 2008.

Case 3: Here, the differences between residual set $\hat{\mathbf{e}}_{\#1}$ and $\hat{\mathbf{e}}_{\#3}$ are computed for December 2008 and are added to the range-rate observations ($\dot{\boldsymbol{\rho}}_1$) as

$$\begin{aligned}\hat{\mathbf{e}}_{13} &= \hat{\mathbf{e}}_{\#1} - \hat{\mathbf{e}}_{\#3}, \\ \dot{\boldsymbol{\rho}}_3 &= \dot{\boldsymbol{\rho}}_1 + \hat{\mathbf{e}}_{13}.\end{aligned}\tag{3.9}$$

The $\hat{\mathbf{e}}_{13}$ represent the attitude errors reduced due to an incorrect combination of the two star camera datasets.

Case 4: Here, the differences between residual set $\hat{\mathbf{e}}_{\#1}$ and $\hat{\mathbf{e}}_{\#4}$ are computed for December 2008 and are added to the range-rate observations ($\dot{\boldsymbol{\rho}}_1$) as

$$\begin{aligned}\hat{\mathbf{e}}_{14} &= \hat{\mathbf{e}}_{\#1} - \hat{\mathbf{e}}_{\#4}, \\ \dot{\boldsymbol{\rho}}_4 &= \dot{\boldsymbol{\rho}}_1 + \hat{\mathbf{e}}_{14},\end{aligned}\tag{3.10}$$

$\hat{\mathbf{e}}_{14}$ represents the errors reduced due to incorrect combination of the two star camera datasets and the errors reduced due to the fusion with angular accelerations from the accelerometers.

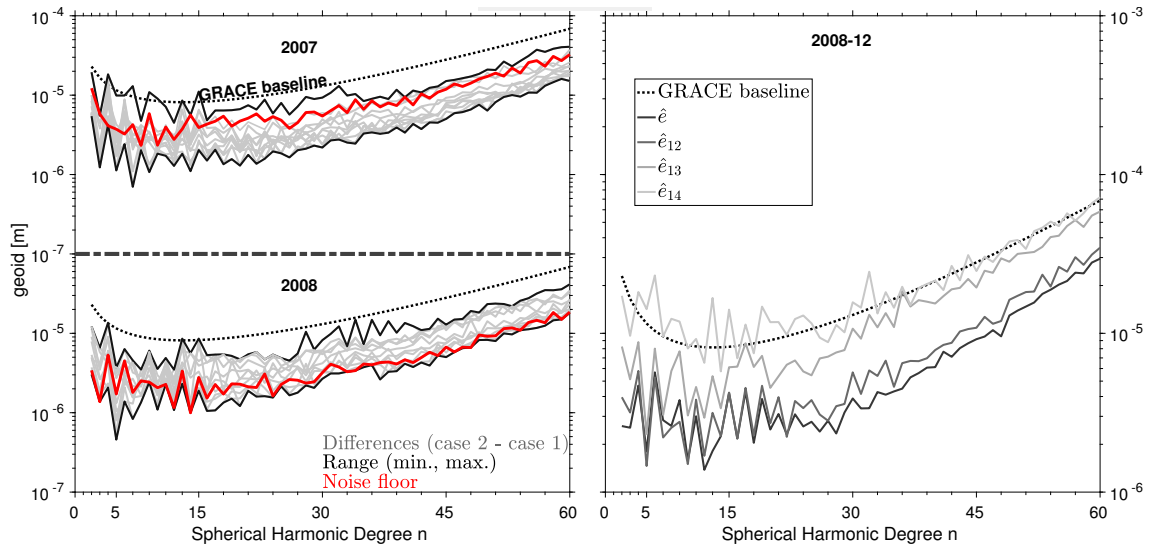


Figure 3.14: Left: *Differences between the monthly gravity field solutions of case 2 and case 1 for 2007 and 2008.* Right: *Degree amplitudes of gravity field solutions computed in all four error cases for December 2008.*

The gravity field solutions computed for December 2008 are compared together for the four cases and shown in the right panel of Fig. 3.14. The comparison of the

four solutions shows, how, step by step, improvements in the attitude errors impact the gravity field solutions.

The comparison between the four solutions is captivating because it explains how the various systematic attitude errors affect the gravity field solutions. The solution computed from $\hat{\mathbf{e}}_{12}$ indicates a small improvement to the solution obtained from case 1 computed from errors $\hat{\mathbf{e}}$. It is simply because $\hat{\mathbf{e}}_{12}$ contains mainly high-frequency errors reduced due to the fusion of angular accelerations. The very small effect in low frequencies is responsible for the small impact on the gravity field solutions computed up to degree 60. It also explains the reason why the differences shown in the left panel of Fig. 3.14 are close to the noise floor. The solution computed from $\hat{\mathbf{e}}_{13}$ contains the attitude errors due to the incorrect combination of data of two available star camera heads. The correct combination of the star camera heads improved the accuracy of the star camera attitude data which is prominent at low frequencies. Thus, the errors show significant impact on the gravity field in the considered simulation scenario especially after degree 15. The solution computed from $\hat{\mathbf{e}}_{14}$ contains errors due to incorrect star camera data combination along with high-frequency errors which are reduced by including angular accelerations from the accelerometers. The set of residuals $\hat{\mathbf{e}}_{14}$ and $\hat{\mathbf{e}}_{13}$ have biggest impact among all the cases when compared to the solution computed from $\hat{\mathbf{e}}$. Differences of one order of magnitude exists between the solutions obtained from $\hat{\mathbf{e}}_{14}$ or $\hat{\mathbf{e}}_{13}$ and $\hat{\mathbf{e}}$ which is a significant number in assessing the precision of gravity field solutions. The impact is significantly large such that it reaches the GRACE baseline. Effects up to degree 30 are observed when compared to the solution $\hat{\mathbf{e}}_{13}$. A large impact of the solutions from errors $\hat{\mathbf{e}}_{13}$ and $\hat{\mathbf{e}}_{14}$ indicates that the systematic attitude noise reduction from the range-rate observations has great potential for improving the gravity field solutions.

Recent findings by Harvey (2016) indicated that the attitude computed from star cameras contain other errors due to bugs present in the onboard data processing software. If those errors altogether will be corrected and investigated in similar simulations, it can be expected that the contribution of the attitude errors will reach above the baseline. Even in our case, the contribution reflected by the $\hat{\mathbf{e}}_{14}$ solution clearly indicates a large scope of reducing the systematic attitude errors in the gravity field solutions.

3.6 Summary

First, the attitude errors and their sources have been reviewed and discussed. Due to systematics present in the attitude determination, the pitch and yaw accuracies are affected the most. This has been studied by taking the advantage of reprocessed attitude data #2 which is computed by the combination of star camera and angular acceleration data. The comparison between attitude data #1 and #2 (cf. Table 3.2) reveals a significant reduction of errors in the pitch and yaw angles. The roll angles are similar in performance for both attitude datasets. A similar characteristics has been seen for the antenna phase center offset corrections.

Second, it is shown that the attitude errors propagate into the range-rate observations through the antenna phase center corrections and linear accelerations. Among the two, the error contribution by the antenna phase center corrections are significant (cf. Fig. 3.9 & 3.7). The almost equal amplitude of the antenna phase center correction errors and the post-fit residuals indicates that most of these errors are propagated to the residuals. The accelerometer observations are affected by attitude errors at very high frequencies (>35 MHz). Also, these errors propagate to the post-fit range-rate residuals.

Third, the impact of attitude errors on the gravity field solutions has been discussed. The investigated attitude errors remain below the GRACE baseline for almost all months. However, the attitude errors ($\hat{\mathbf{e}}_{14}$), which represent the improvements after combining the correctly implemented SCA data with the angular accelerations from the accelerometers, show a significant impact on the gravity field solutions which reaches the GRACE baseline (cf. Fig. 3.14). It clearly shows how crucial it is to further improve the attitude products in order to reduce the related errors in the gravity field solutions.

Chapter 4: Inter-satellite ranging errors in range-rate residuals

4.1 Inter-satellite ranging

The key science instrument of the GRACE mission is the K-band microwave ranging assembly which measures the phase modulated on the two frequencies namely K- (24 GHz) and Ka-band (32 GHz). The two phases are transmitted between the two spacecraft. These phase measurements are combined together to get the Dual One Way Range (DOWR) measurements (cf. Fig. 4.1 step 3). The change in the range depends on the changes in the gravity field of the Earth. The precision of these DOWR measurements is at the micrometers level (Steitz et al., 2002). The process of combining phase measurements to get the range observations is called the standard KBR1A to KBR1B processing (Ko, 2008; Wu et al., 2006). Steps of this processing are briefly described in Fig. 4.1. As shown in step 3, the DOWR is low-pass filtered (cut-off 0.1 mHz) and the biased range is obtained. The biased range measurements are the products provided in the standard KBR1B dataset and are used in the gravity field recovery. These range measurements represent the range change between the KBR phase centers (shown in Fig. 3.2 (a.)).

In order to estimate the gravity field parameters, however, the measurements must represent the range change along the line-of-sight (LOS) (cf. Fig. 3.2 (a.)). Ideally, the phase centers should co-incide with the LOS but, due to geometrical asymmetry of the GRACE spacecraft, they do not. Therefore, the Antenna Offset Corrections (AOC) are applied to the range measurements to represent the observations along LOS. More details about antenna offset corrections are explained in Chapter 3. Since one spacecraft is leading and another is trailing, their time of flight is different which also needs to be accounted for in the gravity field recovery. Therefore, the light time corrections¹ are applied to the range observations to reduce the errors

¹The dual one way ranging assumes the same time-of-flight (τ) for both satellite phase signals. Since the two satellites are always moving in a similar direction, the time-of-flight of the phase signal from the leading satellite is shorter than the time-of-flight of the trailing one. The actual range measurement derived from the dual one way ranging phase measurements contains both of these different times-of-flight. The correction is applied to get the instantaneous range at one specified epoch of time which is referred to as *light-time corrections*.

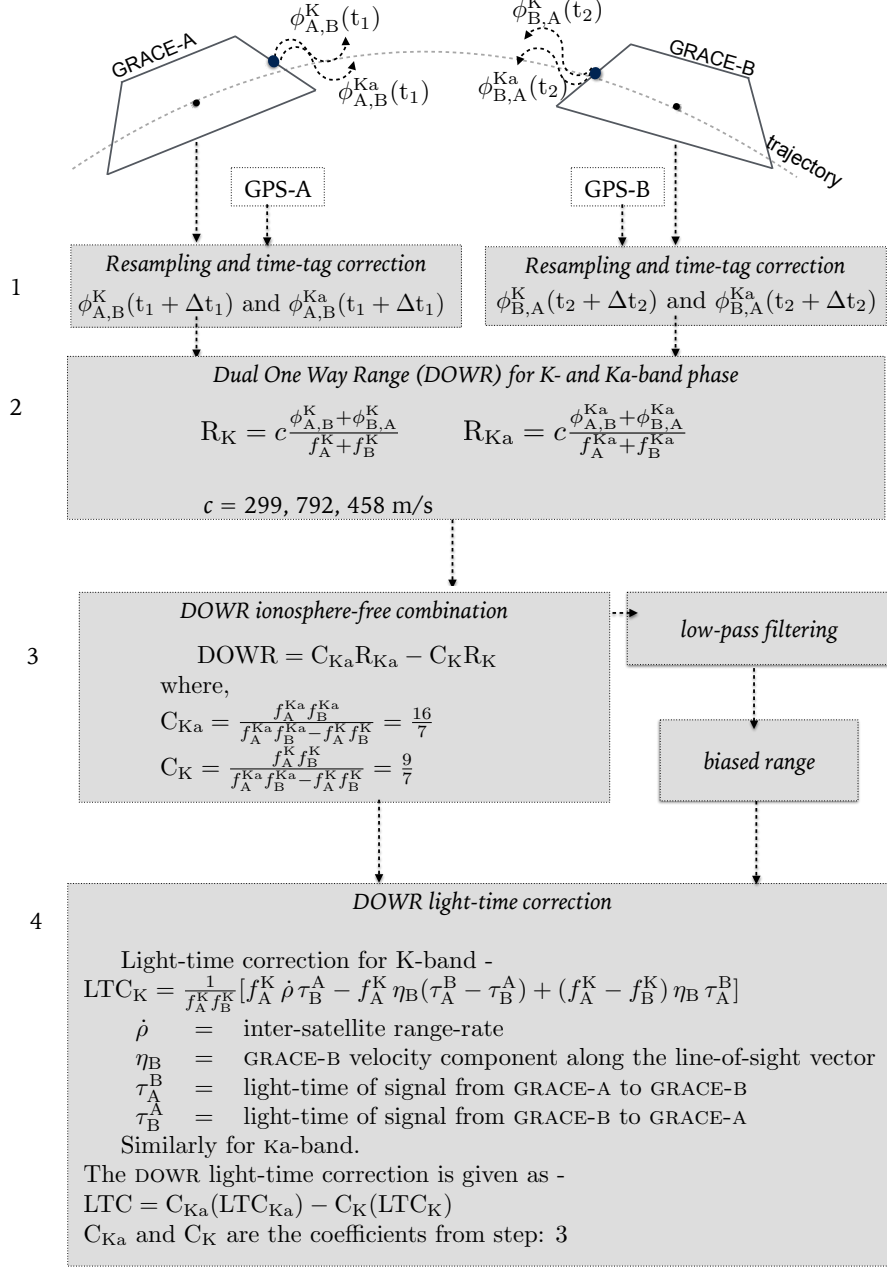


Figure 4.1: Computation of range observations from the K- and Ka-band phase observations of GRACE-A and GRACE-B (Ko, 2008; Wu et al., 2006).

due to different time of flights.

In the standard KBR1B products, range-rates are also provided which are computed by differentiating the biased instantaneous range observations using the CRN-filter (Wu et al., 2006). These range-rate measurements are then generally used to estimate the global gravity field parameters.

4.2 Inter-satellite ranging errors

Since the biased instantaneous range is computed from the four phase observations (K- and Ka-band frequency of GRACE-A and GRACE-B), it suffers from the ‘*phase errors*’ of each carrier frequency. Due to the differences in the unknown clock offsets of the two satellites, the observations also suffer from the ‘*time-tag error*’. The ‘*oscillator noise*’ depends on the frequencies of the microwave ranging system, drifts in the frequency measured by the ultra-stable oscillator (USO) and the time-of-flight (τ). While combining the two dual one way range (as shown in step 3 of Fig. 4.1) from each frequency, most of the oscillator noise cancels out due to the similar drifts in the frequencies. Similarly, most of the time-tag errors cancel out during the combination leaving the noise level $<1 \mu\text{m}$ (Ko, 2008; Xu et al., 2015). As mentioned above, due to the asymmetry in spacecraft geometry, the phase center of the K-band antenna horn does not co-incide with the LOS due to which indirect signals are reflected near the phase center. These indirect signals affect the carrier phase measurements which is called ‘*multipath noise*’. The knowledge about these noise types exists from the pre-launch mission studies by Kim (2000); Thomas (1999).

Kim (2000) provided the expected level of the various noise sources (cf. Fig. 4.2) and their impact on the gravity field solutions. He provided noise models of the accelerometers and the different ranging errors which are used to validate the level of noise obtained from the real gravity field solutions. Among all ranging errors, the oscillator noise is the biggest in the frequencies below 5 mHz. But accelerometer noise is still at least two orders of magnitude higher than the oscillator noise and five orders of magnitude higher than the multipath noise. Thus, the pre-launch simulations showed that the most dominating noise source at low frequencies would be the accelerometer noise. Similarly, at high frequencies (above 10 mHz), the system noise from the KBR microwave ranging instrument would dominate.

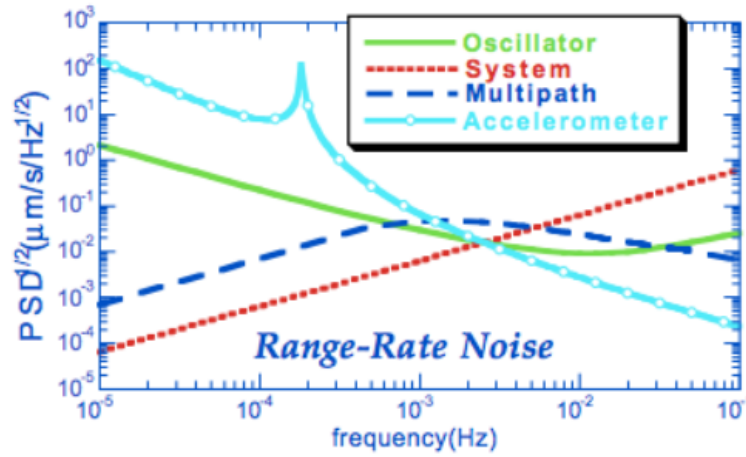


Figure 4.2: *Power Spectral Density (PSD) representation of the different noise sources in terms of range-rate observations, from Kim (2000)*

After the launch of the GRACE mission, investigations of the noise in its data continued. Ko (2008) investigated the ranging errors and showed that the oscillator noise, which is highly dependent on the frequency instability of the USO, was much less (i.e. $0.08 \mu\text{m}$) than the required measurement noise level of $10 \mu\text{m}$. Therefore, it dominates neither the low frequencies nor the high frequencies. The level of frequency instability of each oscillator was found to be approximately 1.5×10^{-13} in terms of Allan variance which is at the required level of frequency instability of 1×10^{-13} . Further, they showed that system noise dominates in the high frequencies, but the source of the noise was not established. Ko et al. (2012) showed that the errors were dependent on the low signal-to-noise ratio (SNR) of the frequencies of the K-Band ranging system. Low SNRs were correlated in particular with the high-frequency noise in the range observations. However, the factors responsible for the errors related to SNRs were not understood. The analysis was carried out on the residuals obtained after gravity field modeling done at the Center of Space Research, University of Texas, Austin, USA.

While analyzing the post-fit range-rate residuals of the ITSG-2014 gravity field model in this thesis, it is also found that the KBR system noise dominates in the high frequencies (above 10 mHz or 90 CPR) which is discussed in the following sections. In order to analyze the high-frequency errors in post-fit residuals, it is necessary to know the system noise and its characteristics first. Therefore, at first, the system

noise is discussed in detail and later the analysis of residuals is presented with focus on the system noise present in them.

According to Thomas (1999), system noise is specified in terms of the ratio $\frac{C}{N_0}$, where C is the received signal power and N_0 is the spectral noise density at the receiving satellite. Thus, $\frac{C}{N_0}$ is the power SNR in the form of input signal power divided by noise power in a 1 Hz bandwidth.

The expected $\frac{C}{N_0}$ ratio for an inter-satellite range of 200 km was 69 dB-Hz. The expected voltage SNR for a GPS BlackJack receiver operating in the quadrature down-conversion and sampling mode is given as

$$\text{SNR}_V \approx \left[\frac{C}{N_0} T_{\text{obs}} \right]^{\frac{1}{2}} \quad 4.1$$

where T_{obs} is the integration time to generate one observation.

The system noise for the GRACE mission is computed from the phase errors of four frequencies of the KBR microwave ranging assembly according to Eq. 3.16 of (Ko, 2008). The computed system noise indicates the deviation of the noise from its mean value, thus it is actually the standard deviation of the system noise (Personal communication, Torsten Mayer-Gürr on 15 May 2018). In order to be consistent with the definition of existing literature (Ko, 2008; Thomas, 1999), we refer to these deviations as the system noise. The $1\text{-}\sigma$ phase error is given in terms of SNR_V in units of cycles as (Thomas, 1999)

$$\sigma_{\phi,i}^{\text{K/Ka}} = \frac{1}{\text{SNR}_i^{\text{K/Ka}}} \quad 4.2$$

where $i \in \text{GRACE-A, GRACE-B}$.

That means, the SNRs describe the errors in the phase observations (phase errors). These values reflect the measure of signal strength and ranging measurement quality. The original values are given in units of dB-Hz but in the KBR1B product they are provided in units of (0.1)dB-Hz. The minimum SNR requirements for GRACE are 630 (0.1)dB-Hz or 63 dB-Hz. Low SNR values reflect high phase errors in the range observations. Thus, they are used as a quality control criteria to obtain a good quality of the range observations. The quality of the range observations in turn determines the quality of the gravity field.

During the combination of phase observations in KBR data processing, the phase observations with SNR values below 450 (0.1)dB-Hz are removed. Thus, either a gap or an interpolated value is obtained depending on the arc length (Wu et al., 2006). The SNRs of three frequencies (i.e. K-band of GRACE-A&B; K-band of GRACE-A) are used in removing the spurious phase observations. The Ka-band SNRs of GRACE-B were anomalous from year 2004 to 2011, thus, they are not considered during the data processing (personal communication Gerhard Kruizinga, 10 Oct. 2016). The time-series in Fig. 4.3 shows that the three valid SNR values vary periodically, whereas the Ka-band SNRs of GRACE-B vary randomly.

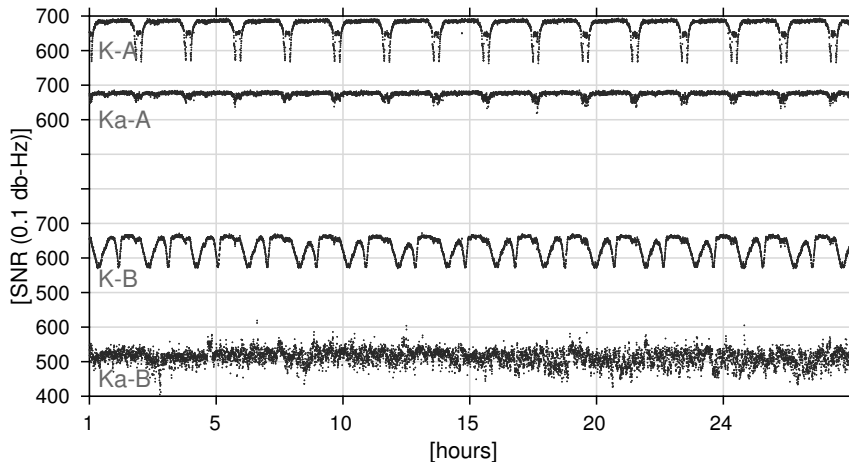


Figure 4.3: *SNRs of the four phase observations of the two satellites for December 1, 2008.*

These SNRs are a measure of the phase errors affecting the range observations. The combined four phase errors represent the system noise in the range observations. Hence, SNRs can be directly used to analyze the residuals for the presence of system noise in them. In the following section, the range-rate residual analysis is presented with focus on this noise.

4.3 Post-fit residual analysis with focus on ranging errors

In this section, the post-fit residual analysis is presented with focus on the ranging errors present in them. Based on previous analyses presented by Kim (2000) and

Ko et al. (2012), the range-rate residuals are dominated by system noise. Here, the range-rate residuals are analyzed for high-frequency (above 10 mHz) system noise in detail. As discussed already, the system noise is derived from the errors of the four phase observations (K- and Ka-band of GRACE-A & B). Correlations between system noise and the range-rate residuals should explain the presence of system noise in the range-rate observations. Ideally, the high-frequency post-fit residuals above 10 mHz should be correlated with the system noise. The correlations should be identifiable in their time-series as well as can be described by the correlation coefficients computed for the two. The analysis shows that their correlations with the system noise are not large which can be seen in the two time-series plotted in Fig. 4.4 (a.). Also, the correlation coefficient is very small, 0.002 on a scale of 0 to 1. It is because the system noise includes all the four phase errors and these phase errors are computed from the SNR values. As explained above, the SNR of the Ka-band of GRACE-B is anomalous which makes the derived system noise unreliable and hence no significant correlations with the post-fit residuals can be seen.

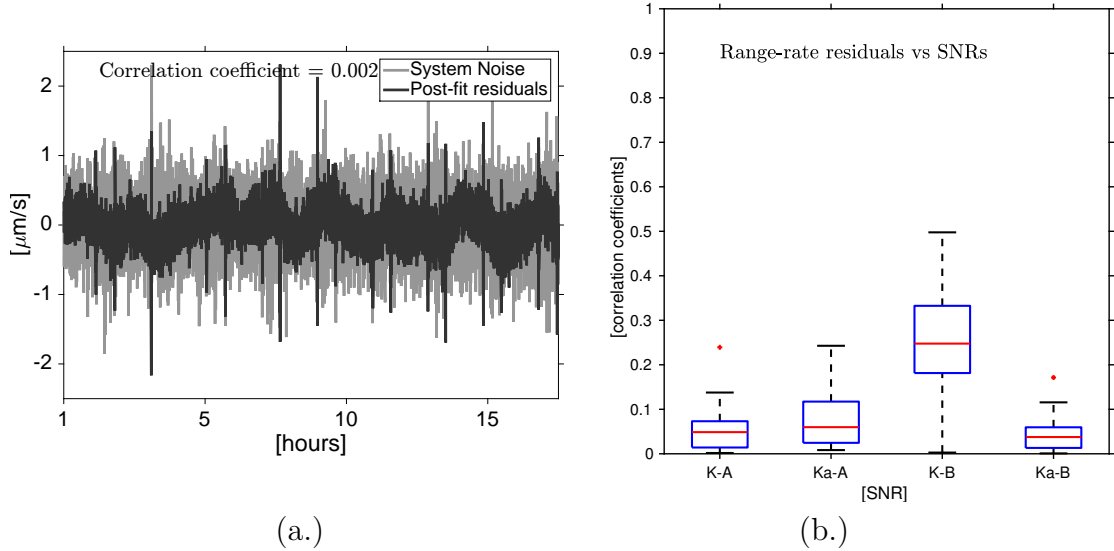


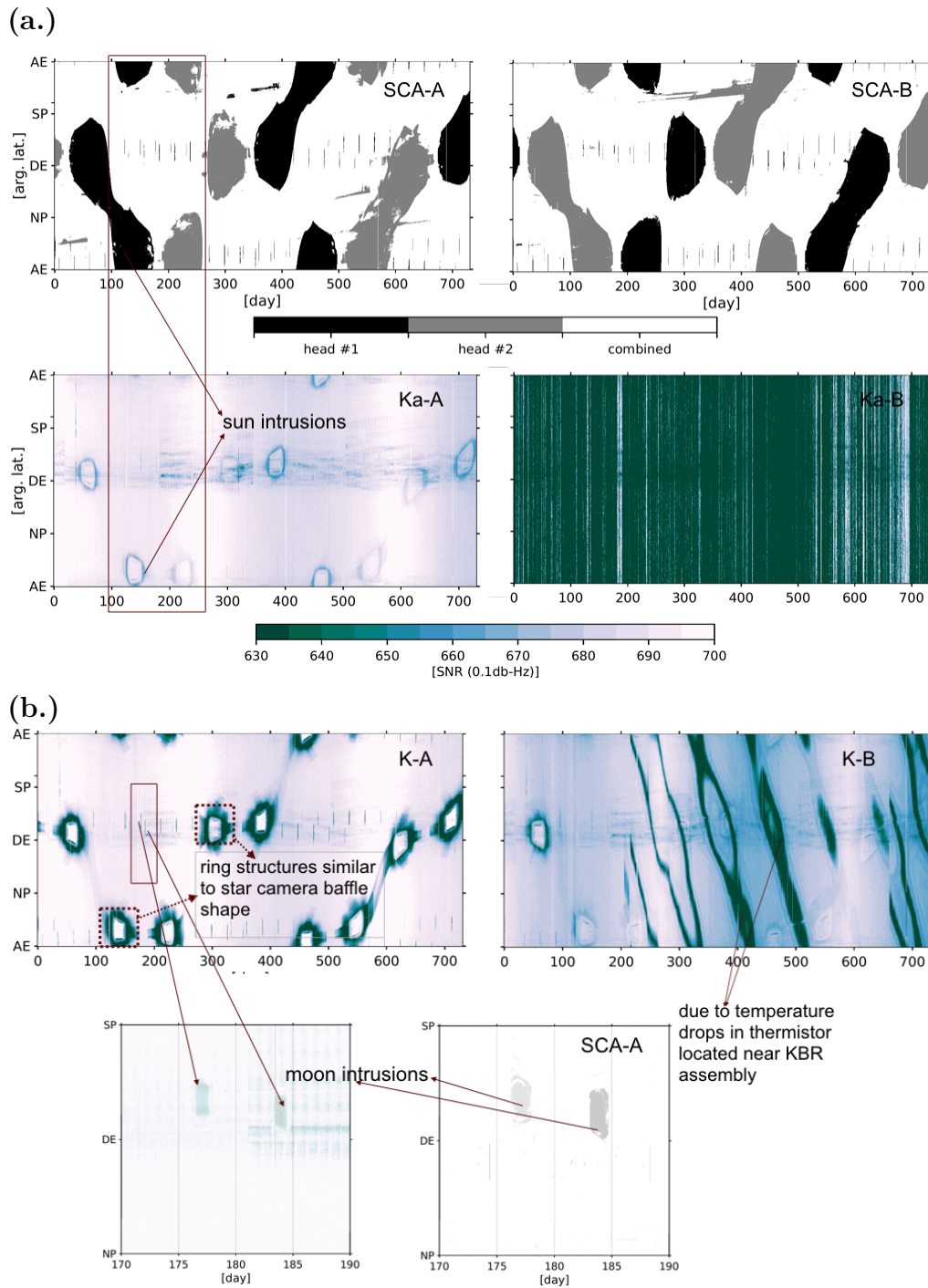
Figure 4.4: (a.) Correlations between the system noise and the post-fit range-rate residuals for 18 hours of December 1, 2008. (b.) Box plots showing the correlations between the individual SNRs and the post-fit range-rate residuals for December 2008.

Another approach is to correlate individual SNRs (or phase errors) and the high-frequency post-fit range-rate residuals to study the presence of system noise in the residuals. Here, high correlations (correlation coefficient upto 0.5) existed with the

SNRs of the K-band frequency of GRACE-B (cf. Fig. 4.4 (b.)). The high correlations of the post-fit residuals with the K-band SNR of GRACE-B shows that the residuals contain system noise which is largely contributed by one of the three non-anomalous SNRs. Now, in order to find the source of the noise and study their characteristics in detail, the SNRs and the range-rate residuals are analyzed using the argument of latitude and time plots. Such plots reveal the systematic errors present in the observations which can not be explained by using a statistical analysis. SNRs on such plots should show their systematic behaviour, similar for the residuals. Also, the cause of correlations between the residuals and the K-band SNR of GRACE-B can be explained then.

The analysis of the SNR values reveals the following characteristics:

1. All three valid SNRs (K-A, K-B, Ka-A) experienced drops during *Sun and Moon intrusions* into the star camera (cf. Fig. 4.5). The strength of these effects was different for the different SNRs (Goswami and Flury, 2016). Harvey et al. (2017) suggested the hypothesis that, since the K-band microwave ranging assembly is located near the IPU where star camera data processing takes place onboard, the star camera data processing may cause electromagnetic interferences with the K-band ranging system. Based on this hypothesis, interferences cause drops in the SNR leaving a ring-type structure (in argument of latitude plots) during the Sun intrusions which may represent the star camera baffle structure. These ring-type structures in the SNR are highlighted in the panel K-A of Fig. 4.5 (b.). The Sun intrusions in the star cameras are shown in the panels SCA-A and SCA-B of Fig. 4.5 for GRACE-A & GRACE-B, respectively. To compare it with the shape of the rings in the SNRs, the star camera baffle shape is shown in Fig. 4.6 with the star camera baffle structures. Also, there exist differences in the strength of sun intrusion related effects in the SNRs. For example, a drop in the K-band SNR of GRACE-A is larger than a drop in the K-band SNR of GRACE-B, see panels K-A, Ka-A and K-B in Fig. 4.5 for comparison. The differences may be due to the different KBR microwave ranging assemblies used on the two spacecraft. The KBR assembly used in GRACE-A was the redundant one and not the primary one. Therefore, the sun intrusion effects on the SNRs of GRACE-A were stronger than of GRACE-B. And, the influence on the K-band SNR was stronger which might be related to



the differences in the two frequencies. The K-band transmitted frequency is exactly three-quarters of the Ka-band.

Due to the similarity of these two phenomena (Sun and Moon intrusions) and their similar influence on the SNRs, corresponding conclusions can be drawn for Moon-related effects (Goswami et al., 2018a).

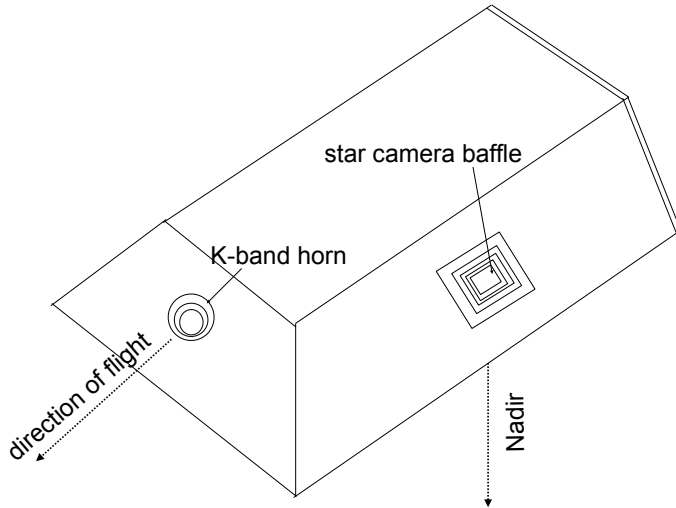


Figure 4.6: *Star camera baffle structure on the GRACE spacecraft after Harvey et al. (2017)*

2. The K-band SNR of GRACE-B not only experienced a drop during the intrusions into the star cameras, but they are also influenced by temperature drops in the instrument (Fig. 4.5). Goswami and Flury (2016) showed that the drops in the K-band SNR of GRACE-B depend on the fluctuations in the sensor unit temperature of the accelerometer (cf. Fig. 4.7). For example, the temperature-dependent bands started to appear from day 204 (23 July 2007) with a sudden drop in the temperature of the accelerometer sensor unit. This drop was 5°C . When it was rising back between days 204 and 214, there was a band of SNR with a slight drop in its values. The band appears between descending equator (DE) and north pole (NP). When temperature increased further, the SNR bands became stronger over the full orbit. Such effects were also investigated

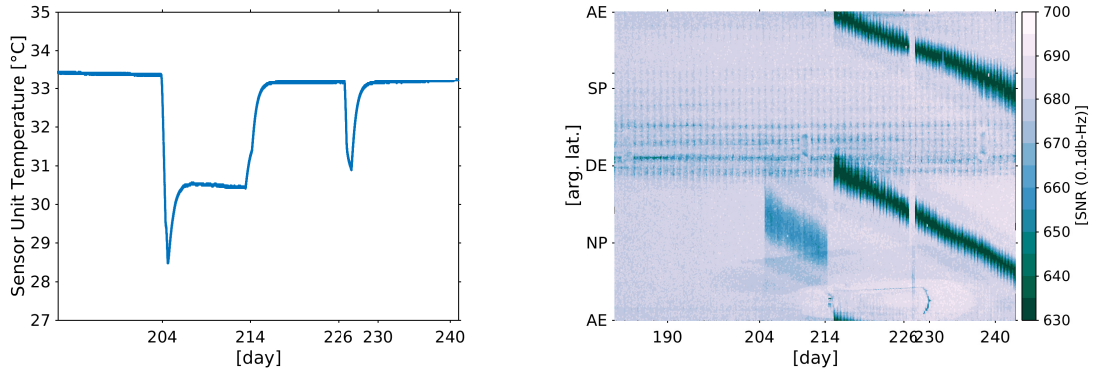
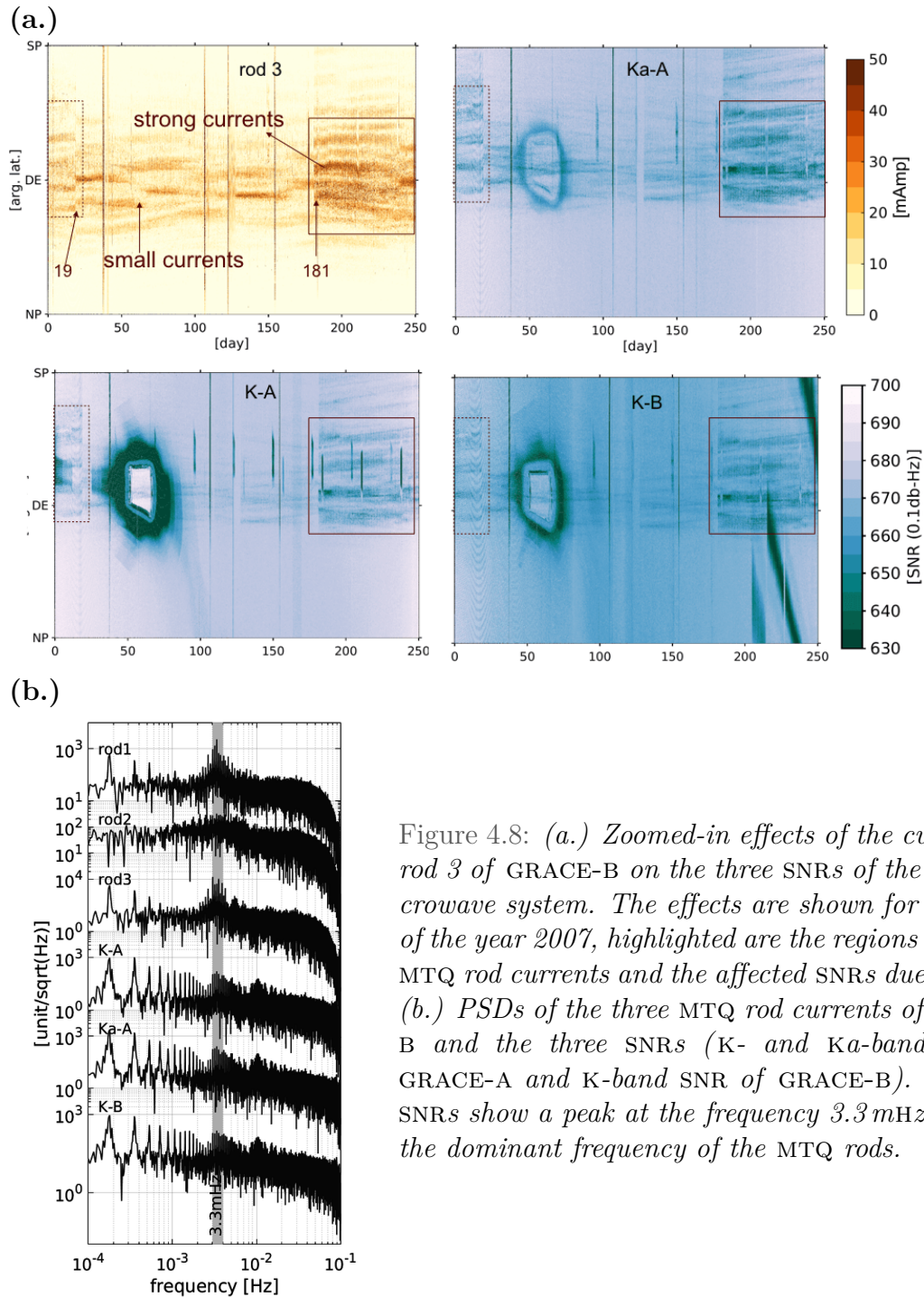


Figure 4.7: *Left panel: Fluctuations in ACC Sensor Unit temperature. Right panel: drops in the K-band SNR of GRACE-B in July and August 2007. The effects dependent on the temperature dips can be seen clearly, specially around day 204, 214 and 226.*

by Harvey et al. (2017). They showed that the fluctuations in one of the thermistors located near the KBR assembly were responsible for the drops in the K-band SNR of GRACE-B. These drops are also visible in the panel K-B of Fig. 4.5 for a period of two years.

3. Besides intrusions and temperature dependent effects, SNRs are also affected by variations in the currents flowing through the magnetic torquer rods (MTQs). The three non-anomalous SNRs (Ka-A, K-B, K-A) are affected by the currents in the MTQ rods of GRACE-B. They vary with the currents flowing through rod 2 and 3 of GRACE-B. In Fig. 4.8 (a), similar variations in the currents of MTQ rod 3 of GRACE-B and the three SNRs are shown for 250 days of the year 2007. The currents were smaller between days 19 to 180 as opposed to the days from 181 to 250. It is because the working star camera head during the days 19 and 180 was *head#2* and beyond that it was *head#1* on GRACE-B (see Fig. 4.5 for the active star camera heads). More details about the MTQ current variations and their dependence on active star camera heads are discussed in Chapter 3. During the period of strong currents flowing through rod 3 of GRACE-B, their effect on the SNRs is obvious in all three SNR plots as opposed to the period when small currents were flowing through the torquer rods (see highlighted region in Fig. 4.8 (a)).

The PSDs of the three valid SNRs also show the signatures of the frequency



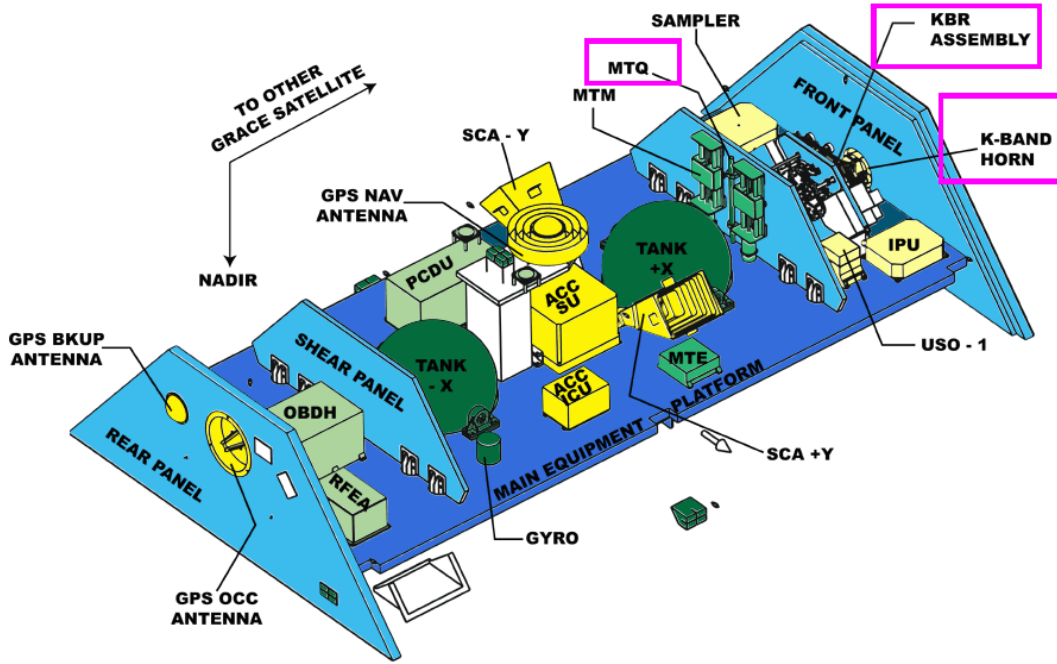


Figure 4.9: Internal view of GRACE showing the location of the MTQs near the front panel where the KBR assembly is mounted © <https://directory.eoportal.org/web/eoportal/satellite-missions/g/grace>

corresponding to the rod currents of GRACE-B (cf. Fig. 4.8 (b)). The frequency 3.3 mHz has earlier been found to be associated with the magnetic torquer rod currents of the GRACE spacecraft (Bandikova et al., 2012).

The KBR assembly is located near one MTQ rod as shown in Fig. 4.9. It is possible that the currents flowing through the rod cause an electromagnetic interference which affects the KBR assembly. Thus, MTQ current related variations in the SNRs are seen as a result of that. However, this hypothesis has to be studied further. Investigations related to MTQ rod current effects on the primary sensors (accelerometer, star-trackers, KBR assembly) are going on at JPL, NASA (personal communication, Gerhard L. Kruizinga on 10 Oct. 2017).

Despite of the fact that SNRs are affected by the MTQ rod currents, no drops below the mission requirements (630 (0.1)db-Hz) are observed during any of the alternate 161 d cycles of the MTQ currents (Goswami et al., 2018a).

Now in order to investigate the post-fit residuals for the presence of system noise related errors, they are analyzed w.r.t. the argument of latitude and time

series, similar to the SNR analysis. The analysis of the post-fit residuals obtained from the ITSG-2014 gravity field models revealed that the temperature-dependent effects, which are present in the SNR of the K-band of GRACE-B, start to appear at frequencies above 9 mHz. They dominate in the frequencies above 20 mHz. The post-fit range-rate residuals are filtered by applying the high-pass filters designed using LTPDA toolbox (Hewitson, 2007). The high-pass filtered post-fit range-rate residuals, with cut-off frequency at 20 mHz, are denoted as (\hat{e}_{HP}) and are plotted in Fig. 4.10. The amplitude of the residuals is extremely high (by a factor of 10) for those specific epochs where the SNR of the K-band of GRACE-B suffers due to temperature drops in the thermistor. Besides temperature-dependent effects, the post-fit residuals are also affected by the Sun intrusion dependent effects in the SNRs. These effects are very small as compared to the temperature-dependent effects and can not be easily identified. That is why they are shown here after zooming-in to the regions where Sun intrusions occur in the SNRs (cf. lower panel of Fig. 4.10).

So far, it has been shown that the post-fit residuals contain system noise at high frequencies (>20 mHz). The main contributors of system noise are identified as temperature effects in the K-band phase observations of GRACE-B and Sun intrusion effects in the phase observations. The analysis of the SNRs showed that the K-band SNRs of GRACE-A (K-A) experience a stronger drop in its values as compared to the other two. The dropped SNRs (K-A) reach down to 550 - 580 (0.1)dB-Hz, similar to the drop in the magnitude of the K-band SNR of GRACE-B during temperature fluctuations (cf. Fig. 4.10). The other two SNRs (i.e. K-B, Ka-A) do not drop below the mission requirements, i.e. 630 (0.1)dB-Hz. Therefore, it is obvious that the sun intrusion dependent errors in the residuals are largely coming from the drops in the K-band SNR of GRACE-A. These effects are propagated to the range-rate observations and correspondingly to their residuals via the phase observations.

When comparing the strength of the two identified effects with each other, one realizes that the temperature-dependent effects are stronger in the post-fit residuals than the Sun intrusion effects. Although, one of the SNRs (K-A) even drops below the mission requirements during Sun intrusions, its effects on the post-fit residuals is very small. The concern here is, if these intrusion dependent errors are not in the post-fit residuals, are they absorbed by the estimated parameters during gravity field modeling?

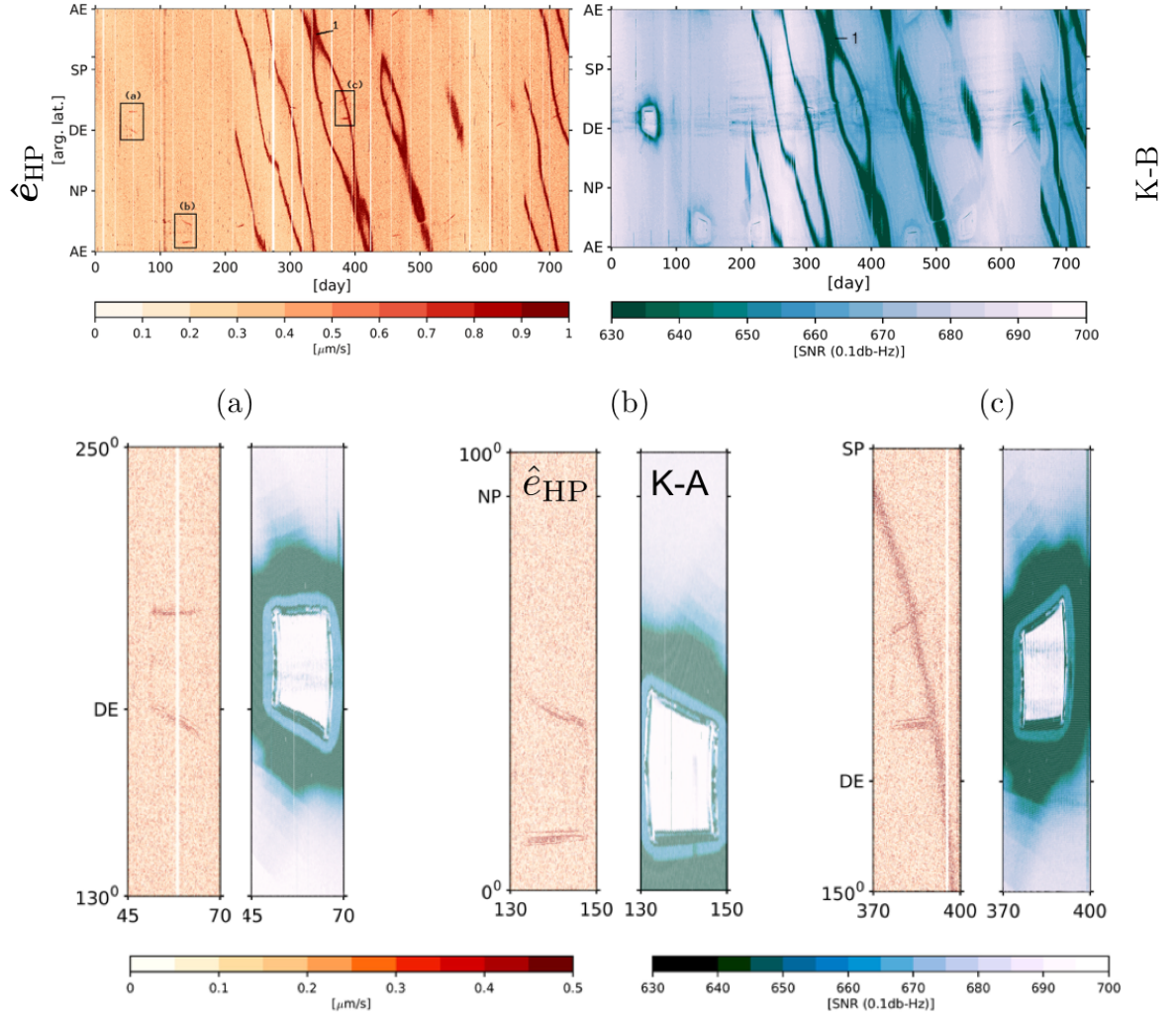
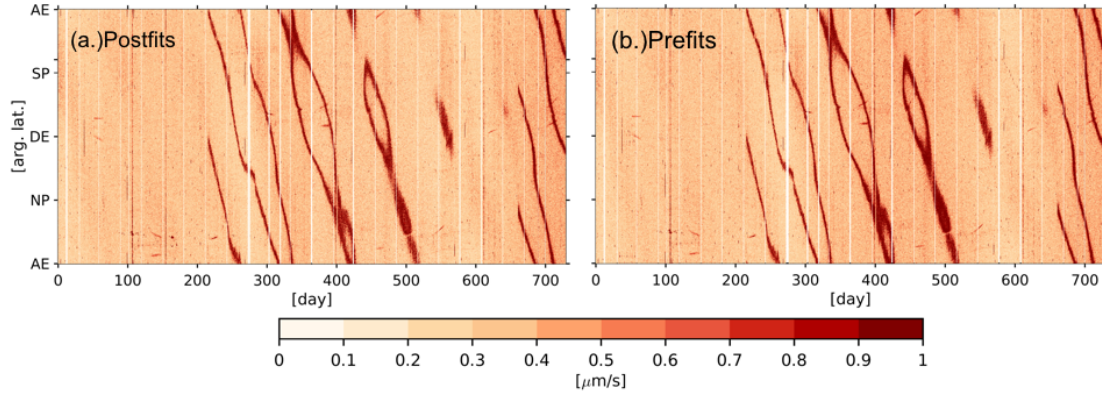


Figure 4.10: Upper panel: (left) High-frequency post-fit residuals (\hat{e}_{HP}) plotted for the years 2007 and 2008, (right) K-band SNR of GRACE-B. Temperature dependent bands are marked as '1' in the upper panels, and '(a)', '(b)', '(c)' in the upper left panel are the effects related to the Sun intrusions (zoom-in view in the lower panels); Lower panels: Zoomed-in picture of the residuals correlated with the Sun intrusion effects in the K-band SNR of GRACE-A.

In order to find an answer to this question, the *pre-fit residuals* (see section 2.4

(1.)



(2.)

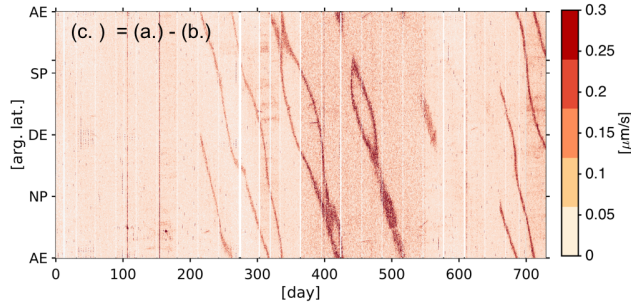


Figure 4.11: (1.) Comparison of the absolute values of high-frequency postfits and prefits.

(2.) Absolute of the differences between the prefits and postfits shown in (1.).

for the definition of pre-fit residuals) are investigated. The pre-fit residuals are the observations obtained after removing all the perturbations which affect the range-rates. These are then used in the gravity field modeling. If the errors related to Sun intrusions are high in these pre-fit residuals and smaller in the post-fit residuals, it indicates that these errors are absorbed into the estimated parameters. Small amplitudes of these errors in the high-frequency filtered prefits indicate small effects on the range-rates. The investigation of the high-frequency prefits shows that the sun intrusion dependent errors are smaller than the temperature-dependent errors in them (cf. Fig. 4.11 (b.)).

The strength of both, the temperature and the Sun intrusion effects in the SNRs looks almost similar in the pre-fit and post-fit residuals. However, the differences between high-frequency pre-fit and high-frequency post-fit residuals show the amount of high-frequency noise which may propagate into the estimated parameters. The differences shown in Fig. 4.11 (c.) are almost a factor 10 smaller than the magnitude of the post-fit residuals. The differences shown in Fig. 4.11 (c.) indicate that a

maximum of 30 % of high-frequency noise may map onto the estimated parameters. This maximum value applies to the epochs where temperature dependent errors are high, otherwise the percentage is as small as 1 - 2 %. This small percentage indicates that the high-frequency errors mainly end up in the post-fit residuals without affecting estimated parameters (Goswami et al., 2018a).

4.4 Impact of high-frequency errors on the gravity field solutions

The analysis presented in the previous section focused on the errors in the high-frequency post-fit range-rate residuals. In an ideal scenario, these high-frequency (> 20 mHz or 111 CPR) errors shall only have an impact on the degrees > 110 approximately (Thomas, 1999). In this thesis, the ITSG-2014 gravity field is estimated up to degree and order 60 which should not be largely affected by high-frequency noise in the range-rate observations. But, this noise could alias into the gravity field coefficients up to degree 60. Such possible aliasing of this noise is studied via simulations.

In order to analyze the impact of the identified systematic errors on the gravity field solution, the following simulation scenarios are considered. The monthly gravity field solutions are computed up to degree and order 60 for each month of the two years 2007 and 2008.

Case 1: Gravity field solutions are computed with noise (ϵ) added to the noise-free range-rate observations ($\dot{\rho}$). The range-rate observations ($\dot{\rho}_1$) are computed as follows: First, the simulated pink noise representing the noise of the accelerometer is used to integrate the orbit. Then, the range-rates are computed from the integrated orbit. Simulated violet noise is added to the range-rates. The violet and the pink noise are derived by differentiating and double differentiating the white noise using the Charge Routing Network (CRN-) filter. White noise of the star camera is added via the simulated antenna center offset corrections. From the simulated orbits, kinematic orbits are derived by adding 3 cm positioning noise to each axis. The simulated noise in each case reflects the errors integrated over the relevant frequency bandwidth. Thus, the total noise ϵ contains the noise of orbit, star camera, ranging and the accelerometer noise. Hence the range-rate observations containing noise ϵ

Table 4.1: *Description of the noise added to the observations in the simulation scenarios.*

Noise	noise type	magnitude of noise (σ)	units
orbit (\mathbf{r})	white noise	0.03	m
accelerometer	pink noise ($\sim 1/f$)		
	along-track	3×10^{-10}	m/s ²
	across-track	3×10^{-9}	m/s ²
	radial	3×10^{-10}	m/s ²
K-band ranging	violet noise ($\sim f$)	2.5×10^{-7}	m/s
star camera	white noise	5×10^{-5}	mrad

are represented as

$$\dot{\boldsymbol{\rho}}_1 = \dot{\boldsymbol{\rho}} + \boldsymbol{\epsilon}. \quad 4.3$$

Case 2: The range-rate observations ($\dot{\boldsymbol{\rho}}_1$) computed in Eq. 4.3 for each month and the monthly set of high-pass filtered post-fit range-rate residuals are added together as

$$\dot{\boldsymbol{\rho}}_2 = \dot{\boldsymbol{\rho}}_1 + \hat{\mathbf{e}}_{\text{HP}}. \quad 4.4$$

Case 3: In order to determine the noise floor, the different noise realizations were simulated which are denoted here as $\boldsymbol{\epsilon}'$ for all noise sources mentioned in Table 4.1. The gravity field solutions are computed from the range-rate observations ($\dot{\boldsymbol{\rho}}_1$) containing different noise realizations each time,

$$\dot{\boldsymbol{\rho}}'_1 = \dot{\boldsymbol{\rho}} + \boldsymbol{\epsilon}', \quad 4.5$$

where $\boldsymbol{\epsilon}$ and $\boldsymbol{\epsilon}'$ are obtained from the same noise distribution. Differences between the gravity field solutions computed from different realizations define the noise floor which is plotted in *red* color in the right panel of Fig. 4.12.

In all cases, Stokes coefficients are estimated along with initial orbital state

parameters $(\mathbf{r}, \dot{\mathbf{r}})$.

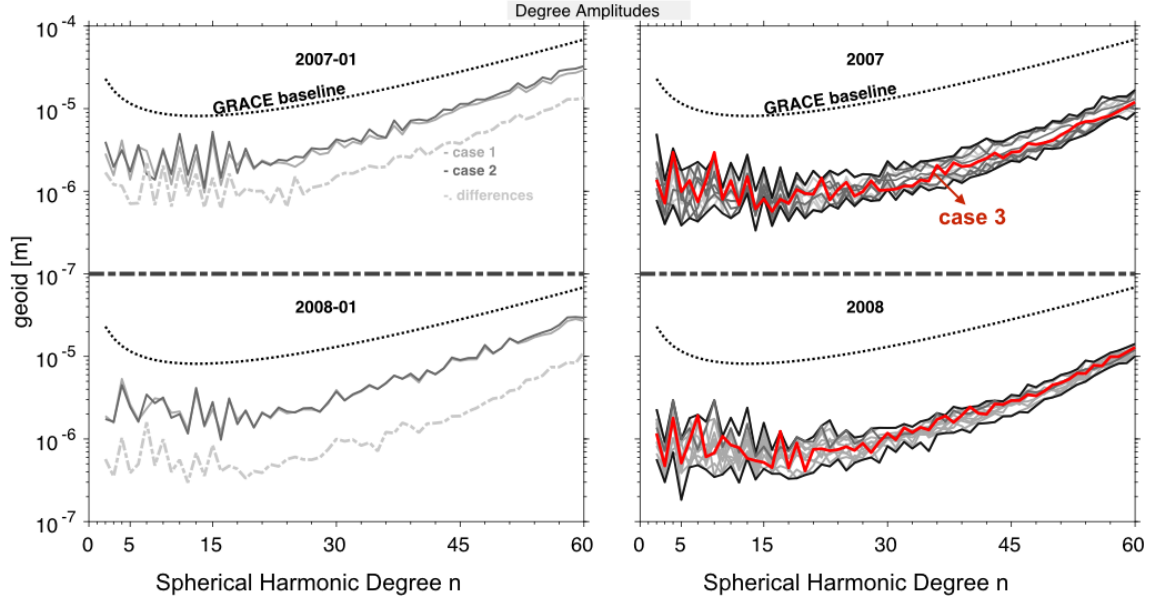


Figure 4.12: *Left: Degree amplitudes of the gravity field solutions from case 1 and case 2 and their differences. Right: Differences between the monthly solutions, i.e. case 1 - case 2, are shown in terms of degree amplitudes for all months of 2007 and 2008. Case 3 represents the noise floor.*

Overall, the impact of the identified errors on the gravity field is very small, they are still below the GRACE baseline (cf. Fig. 4.12). The contributions studied in case 1 and case 2 are also one order of magnitude below the baseline which shows that errors due to high-frequency noise in the range-rate observations are not the major errors propagating to the gravity field solutions.

For January 2007 and 2008, small differences are observed in the geoid degree amplitudes (see left panel of Fig. 4.12) which is due to the added high-frequency post-fit residuals in case 2. The differences are almost one order of magnitude below the GRACE baseline. As the differences in the two solutions (case 1 and case 2) are purely due to the added high-frequency noise, they could be the effect of different noise realization. This hypothesis is proved using case 3. Case 3 is obtained by differences in the solutions computed using different noise realizations. It has a similar behavior as the differences between solutions obtained from case 1 and case 2. Thus, the differences seen in the monthly solutions (left panel of Fig. 4.12) could indeed be the result of different noise realizations.

4.5 Summary

In this chapter, the ranging errors are revisited in the real GRACE satellite observations. As Kim (2000) mentioned, there are different sources of ranging errors. They directly propagate to the gravity field solutions through the range-rate observations. The analysis of the range-rate residuals shows that the KBR system noise is the dominating error source among all ranging errors (system noise, multipath noise and oscillator noise). Multipath (1 - 3 mHz) and oscillator noise (> 3 mHz) are almost impossible to analyze at the current achieved precision level. It is simply because accelerometer errors and geophysical background errors dominate in the low frequencies. In future, the use of more precise accelerometers and improved geophysical error models may make it feasible to analyze those errors which are several orders of magnitude less than the current accelerometer noise level in the range-rate observations (cf. Fig. 4.2). Among all ranging errors, the KBR system noise is the highest noise present in the range-rate residuals of the GRACE mission.

Furthermore, an extensive analysis of the KBR system noise revealed that the SNRs of the K-band phase observations can be used directly to analyze the system noise. The combined system noise was not helpful in providing detailed information due to the anomalous Ka-band SNR of GRACE-B (cf. Fig. 4.4 (a.)). Analyzing the SNRs of the K-band phase observations revealed that the temperature, Sun and Moon intrusions into the star cameras and the magnetic-torquer rod currents affect the K-band microwave assembly (cf. Fig. 4.5 & 4.8). Analysis of the range-rate residuals reveal that they are highly affected by the temperature effects present in the K-band phase observations. Sun intrusion effects also affect the range-rate observations, but they are not as strong as the temperature effects (cf. Fig. 4.10). Both effects are the part of high-frequency spectrum (> 10 mHz). The contribution of these in high-frequency range-rate observations can be up to 30% of the total noise. Note that this happens only when the noise due to temperature is higher in the observations, otherwise it can be smaller, up to 1 - 2%. The investigated system noise does not reveal any significant impact on the gravity field solutions computed up to degree and order 60.

Chapter 5: Accelerometer errors in range-rate residuals

5.1 GRACE accelerometer

The STAR (Space Three-axis Accelerometer for Research), an ultra-sensitive space accelerometer is based on the electrostatic levitation of a parallelepiped proof mass. STAR measures the non-gravitational accelerations perturbing the orbit of a spacecraft flying in low altitude.

The STAR, a 3-axis accelerometer, provides the three linear accelerations along the instrument axes and three angular accelerations about these axes. The measurement resolution of STAR is $3 \times 10^{-9} \text{ m/s}^2$ for the y - and z -axis, $3 \times 10^{-8} \text{ m/s}^2$ for x -axis within a measurement bandwidth of 0.01 - 100 mHz (Touboul et al., 1999a). The measurement resolution of the axes is given in the instrument reference frame, i.e. the Accelerometer Frame (AF) of Reference. The definition of three axes (x_{AF} , y_{AF} and z_{AF}) of the STAR accelerometer in orbit are shown in Fig. 5.1.

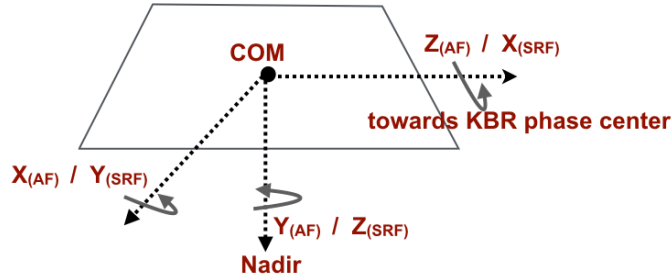


Figure 5.1: Characterization of the three axes of the GRACE accelerometers. The direction of the three axes in the instrument frame which is the accelerometer frame are marked with subscript AF. The three axes in the Science Reference Frame are marked with subscript SRF (Bettadpur, 2012).

There are two main applications of these ultra-sensitive accelerometers in the field of Earth observation from space (Touboul et al., 1999a):

1. The measurement of surface forces acting on the satellite provides the information about the atmospheric density variations and the high-altitude winds.
2. They measure the influence of solar radiation pressure acting on all surfaces of a low-altitude satellite. The accelerometer precision is crucial for the orbit

control maneuvers and the accuracy of the gravity field derived from the orbit observations.

For low Earth orbit satellites such as GRACE, the precision of the gravity field solutions highly depends on the precision of the non-gravitational forces obtained from the accelerometers. Any errors in the accelerometer observations may have a direct impact on the gravity field solutions. By analyzing the range-rate residuals, the characteristics and sources of errors propagating through accelerometer observations can be investigated. The understanding of the error contributions will then be helpful in improving the data pre-processing strategies and better modeling of those errors in the gravity field parameter estimation chain.

In order to analyze the residuals with focus on the accelerometer errors, it is necessary to revisit the characteristics of the GRACE accelerometers and investigate the errors that exist in their observations. Hence, in the following sections, firstly the error characteristics of the accelerometer is discussed. Secondly, an analysis of the range-rate residuals is carried out with focus on the errors propagated through the accelerometers.

5.2 Errors and characteristics of GRACE accelerometer observations

Each GRACE satellite is equipped with one accelerometer mounted at the center of mass of the satellite. The accelerometer measures the non-gravitational forces acting along the three axes of the spacecraft. Due to the importance of their precision in the gravity field modeling, they have been one of the interesting research topic since the launch of GRACE (Bezdek, 2010; Calabria et al., 2015; Flury et al., 2012, 2008; Hudson, 2003; Jean et al., 2017; Klinger and Mayer-Gürr, 2016; Peterseim, 2014; Peterseim et al., 2012). Specifically, the large accelerometer errors in the low-frequency regime (below 10 mHz) are crucial to study (cf. Fig. 5.2) because they contribute to the low-degree spherical harmonic coefficients. And, the precision of the low-degree spherical harmonic coefficients is crucial in order to analyze the time-variable gravity field of the Earth.

As mentioned above, the two accelerometers measure the non-gravitational sig-

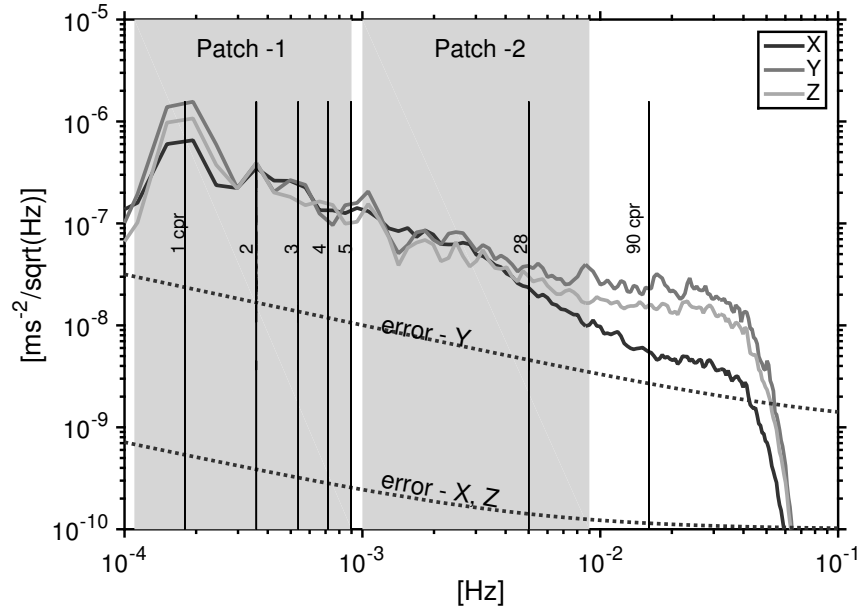


Figure 5.2: *PSD of the calibrated linear accelerations (x –, y – and z –axis) and their error models in units $\text{ms}^{-2}/\sqrt{(\text{Hz})}$ (Stanton et al., 1998). The accelerometer errors are large at low frequencies, i.e. up to 7 - 8 mHz in all three axes.*

nals sensed by the satellite. In order to study their signal characteristics, the measurements can be compared either with the available models of the individual forces or by investigating their dependence with auxiliary GRACE datasets. One such comparison is presented here and is shown in Fig. 5.3 for linear accelerations in the x –axis of GRACE-B.

The content of Fig. 5.3 is described followed by the explanation of wind and solar radiation effects analyzed in the linear accelerations. Fig. 5.3 (1) represents the duration for which the spacecraft was either in the shadow or in the sunlight. The shadow is modeled as described by Montenbruck and Gill (2000). The linear accelerations (x –axis) are shown on Fig. 5.3 (2). They are taken from the ACC1B dataset provided by JPL, NASA. Fig. 5.3 (3) represents the horizontal wind velocities. These velocities are modeled for the GRACE spacecraft using the HWM14 wind model. The velocities are downloaded from <http://thermosphere.tudelft.nl/accelldrag/data.php>. Fig. 5.3 (a) represents the temperature differences between front and rear panel of the satellite. Similarly, Fig. 5.3 (b) represents the temperature differences between port and starboard panel of the satellite. Fig. 5.3 (c) shows the temperature due to radiations incident on

the nadir panel of the satellite. The details about the panels of the satellite are explained in Appendix A. Temperatures of the satellite panels are provided in the telemetry dataset which is referred to as THCE product. The THCE product was provided by Tamara Bandikova in 2016. Details about the panels for which differences are calculated are also given in Table 5.1. The accelerations along y - and z -axis are shown in Fig. 5.4. The observations shown in Figs. 5.3 & 5.4 are for the year 2008.

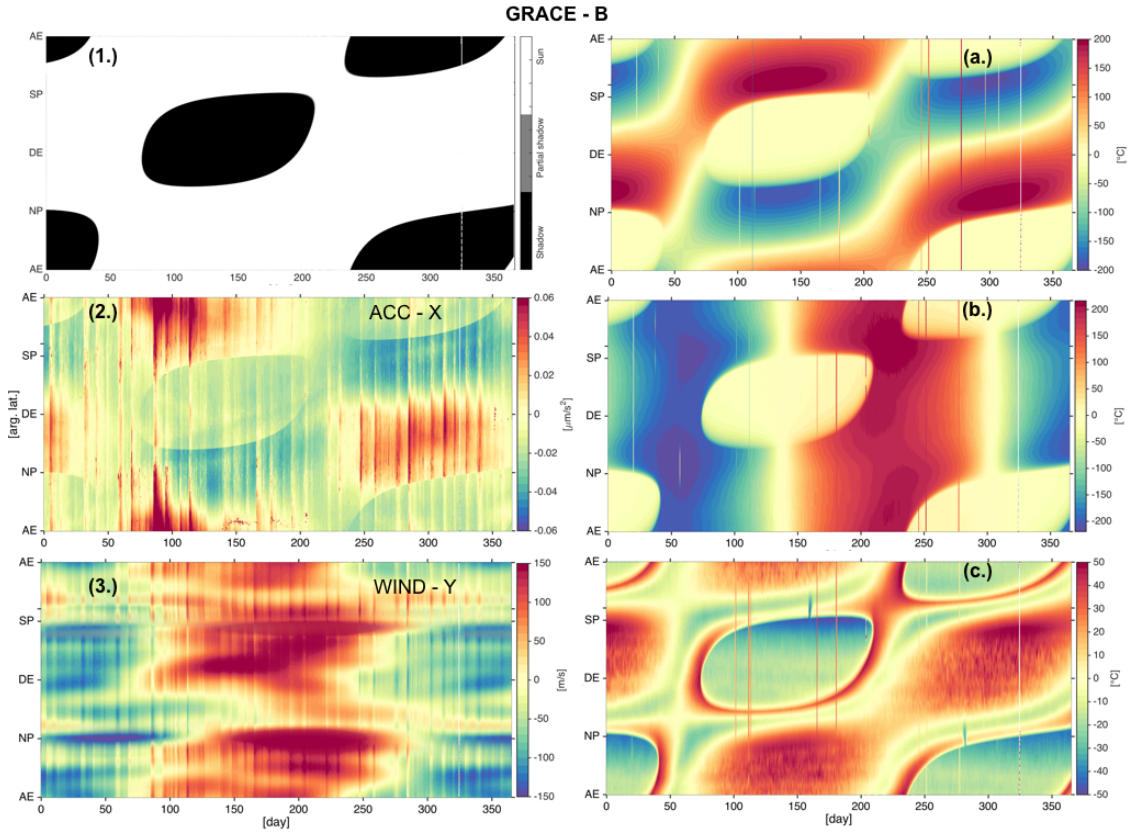


Figure 5.3: (1.), (2.), (3.) show the shadow state of GRACE-B, linear accelerations in the x -axis and the y -component of wind acting on the spacecraft, respectively. (a.), (b.), (c.) shows the temperature differences computed from the CESS data (THCE dataset of GRACE-B). The details about the CESS temperature plot panels are given in Table 5.1

It is interesting to observe the dependence of the linear accelerations on the transition of the spacecraft into and out of sun shadow. The linear accelerations experience a noticeable increase in their magnitude while transitioning from shadow

Table 5.1: *Temperature details of CESS (Coarse Earth and Sun Sensors) data plotted in Fig. 5.3 in panels (a.), (b.) and (c.).*

Panel number in Fig. 5.3	Details
(a.)	temperature differences between front and rear panel
(b.)	temperature differences between port and starboard panel
(c.)	temperature of nadir panel

GRACE-B

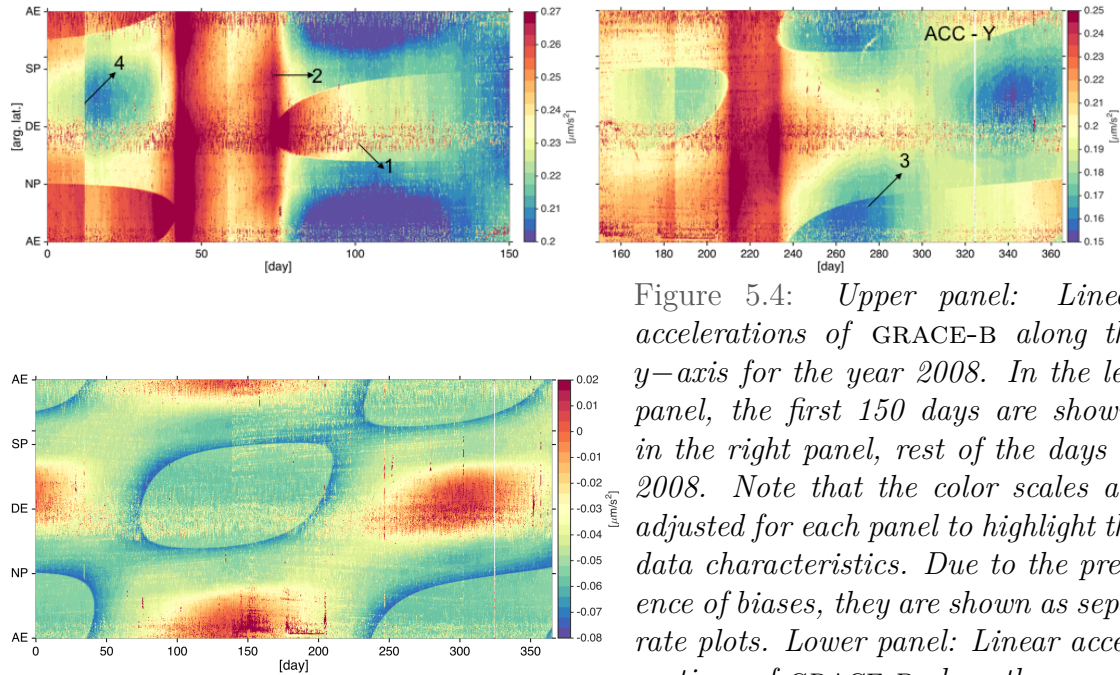


Figure 5.4: *Upper panel: Linear accelerations of GRACE-B along the y -axis for the year 2008. In the left panel, the first 150 days are shown, in the right panel, rest of the days of 2008. Note that the color scales are adjusted for each panel to highlight the data characteristics. Due to the presence of biases, they are shown as separate plots. Lower panel: Linear accelerations of GRACE-B along the z -axis are shown for 2008.*

to the full sun orbit. It leaves signatures of the full shadow state in the accelerations (see Fig. 5.3 (1) and (2)). Fig. 5.3 (1) shows the duration for which the spacecraft was either in the full sun or in shadow during 2008. Fig. 5.3 (2) shows changes in the linear accelerations. Similarly, the high-altitude winds are also sensed by the accelerometers. An example of strong dependent effects is seen by comparing Fig. 5.3 (2) and (3). Around day 100, when the velocity of the winds increases (see Fig. 5.3 (3)), these changes are experienced by the linear accelerations (in Fig. 5.3 (2)). The effects of the usual changes in the wind velocity appear as vertical stripes along full orbits.

Changes in the accelerations due to radiation pressure acting on the satellite panels can be compared with measured temperature differences, see Fig. 5.3 (a), (b) & (c). One can model the radiation pressure incident on each panel of the satellite in order to do the analysis but here we use the GRACE THCE dataset to study the dependency of one effect on the other. Since the temperature is directly proportional to the amount of radiations incident on the satellite panels, it can be used to study the effects of radiation pressure acting on the satellite. The linear accelerations of the x -axis depend on the temperature differences shown in Fig. 5.3 (a). When the spacecraft transits into the shadow, small temperature differences observed between front and rear panel correspond to the small magnitude of accelerations along the x -axis. The magnitude of accelerations increases when the spacecraft moves out of the shadow. It also depends on the increase in the temperature differences between front and rear panels (Fig. 5.3 (a)). Similar effects are also observed for the nadir panel. When the spacecraft is in full sun orbit, the temperature of the nadir panel increases due to the more amount of radiations incident on it. This temperature increase causes an increase in the accelerations. For example, from days 250 to 300 near north pole and descending equator, dependencies are obvious (compare Fig. 5.3 (2) & (c)). More effects due to radiations incident on the nadir panel are observed by the accelerations along the z -axis which is illustrated in the lower panel of Fig. 5.4.

Similarly, dependencies between the temperature differences in Fig. 5.3 (b) and accelerations in upper panels of Fig. 5.4 are high. Fig. 5.3 (b) shows the temperature differences between the starboard and the port panel of the spacecraft. Transition between the large to small magnitudes of temperature differences is clearly depen-

dent on the beta prime angle¹(β'). For example, the temperature differences are negative during the days from 1 to 160 and then the differences are positive after day 160 to ~ 310 . It is because, during the first β' cycle which is of 161 days, the starboard panel received more radiations as compared to the port panel, since it was facing the sun. During the second β' cycle, the position of the two panels w.r.t. the sun reversed. Hence, their differences vary periodically with a period of 161 days. The time period when temperature differences are more than $\sim 300^\circ\text{C}$, a strong bias in the accelerations along the y -axis (an example is shown in the upper panel of Fig. 5.4 marked with '2') is caused. With the comparison between plots (a, b, c) and (2) of Fig. 5.3 it is shown that the accelerations are sensitive to the radiations incident on different panels of the satellite, hence the force is sensed by the accelerometer due to radiation pressure.

Up to here, the temperature differences between different satellite panels directly affecting the magnitude of accelerations were discussed. Similarly, effects due to changing wind velocities on the measured accelerations are observed. So far it has been discussed that the observed non-gravitational signals represent the forces acting on the satellite due to changes in the environmental conditions of the satellite such as wind, its position w.r.t sun, β' angle, etc. However, sometimes these observations are affected by other disturbances. Such disturbances or errors again affect the precision of observations. In the following, these errors or disturbances are discussed along with the expected accuracy of the accelerometers.

Before the launch of the mission, the accuracy requirements of the two accelerometers were described by Stanton et al. (1998) and Kim (2000). Later, Frommknecht (2007) and Flury et al. (2008) also discussed the error models of the GRACE accelerometers in the frequency domain in terms of Power Spectral Density and explained it in units of $\text{m}^2/\text{s}^4/\text{Hz}$ as

$$\begin{aligned} E_{y_{\text{ARF}}, z_{\text{ARF}}}(f) &= (1 + 0.005/f) \times 10^{-20}, \\ E_{x_{\text{ARF}}}(f) &= (1 + 0.1/f) \times 10^{-18}. \end{aligned} \tag{5.1}$$

Note that, differences in the three axes exist due to the design of the instrument. The along-track (z_{AF}) and the radial axis (y_{AF}) are high-sensitive, whereas the cross-track

¹The beta prime angle is the angle between the orbit plane and the vector between the Earth to the Sun (Clawson, 1991). It varies between $\pm 90^\circ$.

(x_{AF}) axis of both accelerometers is less-sensitive. As the instrument is tested on ground, the x -axis is less accurate to make it operable under one g gravity (Touboul et al., 1999a).

One of the main challenges of the GRACE accelerometers is the determination of precise *scale* factors and *bias* parameters. The observations of the two accelerometers along the three axes suffer from different *scale* factors and time-dependent *bias* parameters. These factors are also different for the two satellites. Bettadpur (2009) provided the initial *scale* factors and *bias* parameters to correct the accelerometer ACC1B product as follows

$$\mathbf{a} = \mathbf{S} \mathbf{a}_{\text{ACC1B}} + \mathbf{B} + \boldsymbol{\epsilon}, \quad 5.2$$

where \mathbf{S} is the diagonal *scale* factor matrix. A diagonal matrix is used assuming that the linear accelerations of the three accelerometer axes are orthogonal to each other and there is no cross-talk factor present between them (Kim, 2000). \mathbf{B} contains the *bias* components in all three directions. $\mathbf{a}_{\text{ACC1B}}$ are the linear accelerations provided in the standard ACC1B data. The symbol $\boldsymbol{\epsilon}$ represents random noise of the observations. The differences between the raw and calibrated linear accelerations of GRACE-A are, as example, shown in Fig. 5.5.

The calibrated ACC1B product is used for global gravity field recovery. Besides initial corrections of *scale* and *bias*, these parameters are also estimated periodically during the orbit determination and gravity field parameter estimation steps. It is done to accomodate sudden changes that occur in the *bias* parameter because of disturbances from satellite orbit control and other maneuvers, and environmental conditions. For example, one such effect causing a change in the bias is shown for the y -axis in Fig. 5.4, upper panels. There, a strong bias marked with ‘2’ is caused by changes in the temperature incident on the satellite panels. Similarly, periodic changes in the shadow state of the spacecraft can induce smaller biases in the observations. Thus calibration factors are estimated during gravity field recovery to account for these small biases as well. In ITSG-2014 solutions, the *scale* factors and *bias* parameters are estimated every three hours, i.e. for every arc, during orbit determination and full gravity field parameter estimation.

Kim (2000) mentioned that, besides the instrument design and environmental

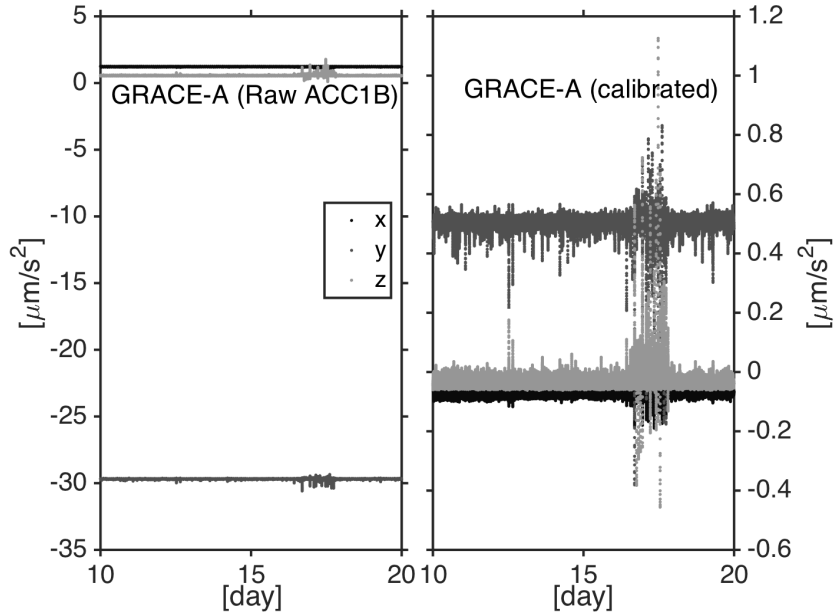


Figure 5.5: *Depiction of the raw accelerations from the ACC1B dataset (left) and after calibration (right). Observations are shown for 10 days of December 2008.*

factors, the thermal instability of the instrument could also be responsible for sudden *bias* changes in the accelerometer observations. Thus, the GRACE accelerometers were made thermally insulated to minimize temperature effects. Insulation to the accelerometer parallelepiped cage is controlled by the two units called Sensor Unit (SU) and Instrument Control Unit (ICU) attached to it. To maintain the inner conditions of the accelerometer cage, changes in the temperature or voltage of SU and ICU are required. These changes also affect the accelerometer observations. The accelerometers, specifically cross-track accelerations (y -axis), are highly sensitive to these sudden changes. For example in Fig. 5.6 (b), effects in the accelerations for 10 days of January 2007 are due to the temperature changes in the SU and ICU. Those effects happen more often in the accelerometer observations since April 2011 because active thermal control is switched-off due to reduced battery capacity (Herman and Steinhoff, 2012). When the satellites approach small beta-prime angles (β'), the GRACE instruments are shut-off because in shadow, batteries can not provide enough power. When β' approaches the full-sun orbit ($>70^\circ$), science data is collected by turning the instruments on. The investigations of the accelerometer data for a long-term time period has been published in Klinger and Mayer-Gürr

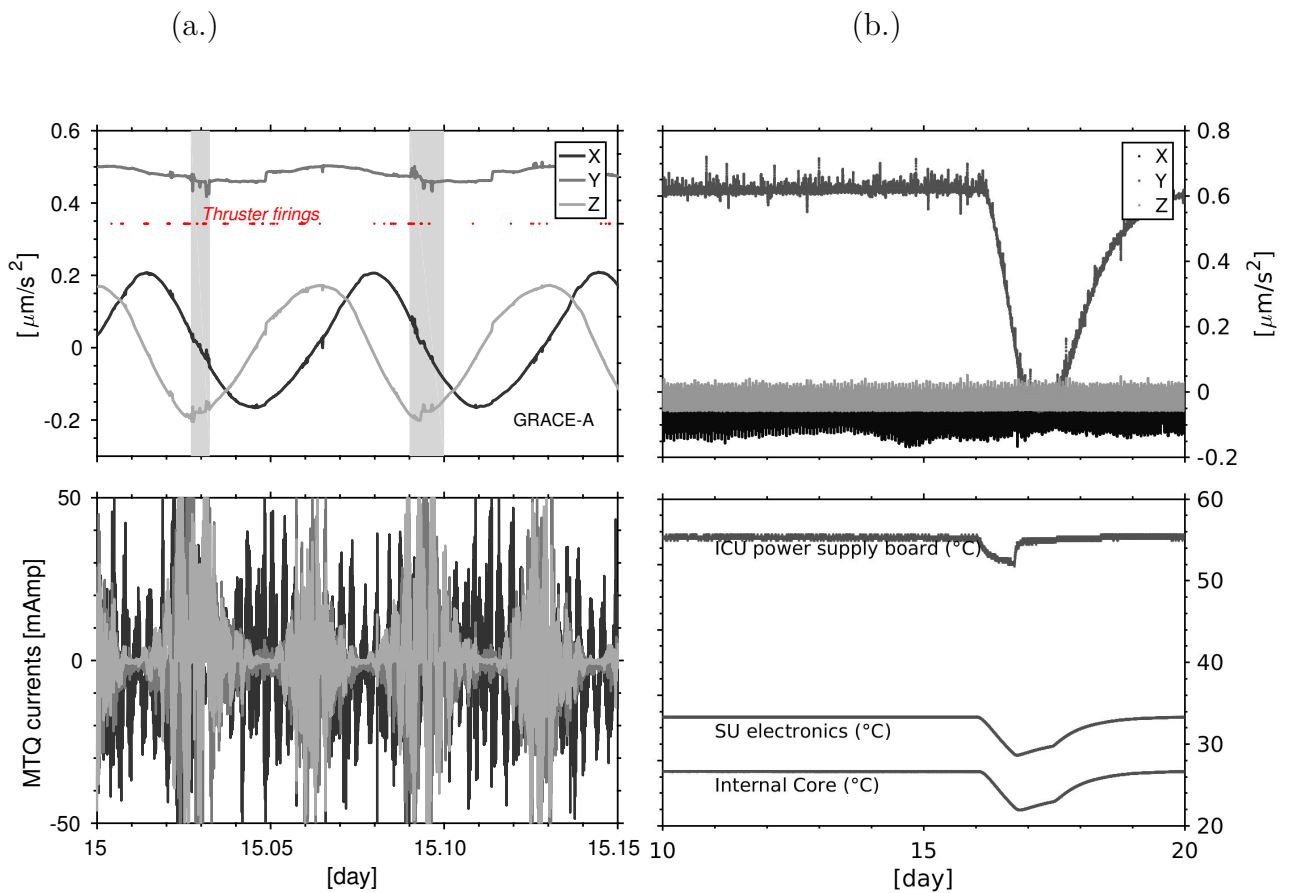


Figure 5.6: (a) Upper panel: Linear accelerations along three axes and the spikes in them due to thruster firings. Lower panel: Magnetic torquer rod (MTQ) currents. Large changes in them disturb the accelerations. Observations are plotted for December 15, 2008. (b) Upper panel: Accelerations sensitive to temperature changes in SU and ICU which are given below. Time period shown is 10 days of January 2007.

(2016) where they presented the more frequent effects of the temperature changes on the accelerometers after 2011. Such disturbances are responsible for the problems in the current accelerometer calibration approaches, ultimately affecting the precision of the gravity field solutions. Therefore, a number of studies have been published focusing on the calibration of the accelerometers and the impact of the calibration approach on the gravity field solutions (Bezdek, 2010; Calabria et al., 2015; Dong et al., 2009; Jean et al., 2017; Klinger and Mayer-Gürr, 2016). The asymmetry of the spacecraft causes another problem which is the difference between the center of proof-mass and the center of gravity of the satellite (Kim, 2000).

Besides these problems, disturbances in the linear accelerations caused by the *orbit and attitude control actuators* lead to sudden spikes in the observations. For example, as shown in the upper panel of Fig. 5.6 (a), the thruster firings actuated to control the inter-satellite pointing and the force due to applied thrust as sensed by the linear accelerations is visible as sudden spikes. Similarly, large currents in the magnetic torquer (MTQ) rods cause spikes in the linear accelerations (see lower panel of Fig. 5.6 (b)). Most of the time, attitude thruster firings and large currents in MTQ rods are actuated simultaneously which makes it difficult to attribute such spikes to just one effect. In the raw level ACC1A dataset, these spikes especially dominate in the direction of the z -axis as shown by Frommknecht (2007). Most of these spikes are related to high frequencies and are filtered when the CRN digital filter is applied with a low-pass filter frequency of 0.035 mHz (Wu et al., 2006). As a result of low-pass filtering, the so-called *twang* signals are also filtered as these effects are also present in high frequencies. According to Touboul et al. (2004), these *twang* signals do not represent surface forces acting on the satellite. They are induced by the satellites' not fully rigid structure. However, the quest of studying the phenomenon of *twangs* was continued by Flury et al. (2008); Hudson (2003) and Peterseim (2014).

Since most of these *twang* signals are filtered using the CRN-digital low-pass filter, their impact on the gravity field solutions is negligible. But a considerable amount of the accelerometer errors still remains in the low frequencies. Examples are effects related to the activation of attitude control sensors as well as temperature and voltage differences of the SU and ICU. Their effects in the cross-track direction (y -axis) are high as compared to the along-track and radial directions. In Fig. 5.4,

the linear accelerations along the cross-track and radial directions as provided in the ACC1B are shown w.r.t. the argument of latitude and time in days for the year 2008. The accelerations are shown for one year in order to highlight the systematic and environmental effects present in the accelerometer data. The effects along the equator which are marked as ‘1’ (cf. Fig. 5.4, upper panel) are due to the thruster firings along the roll axis. Similarly, the effects related to the thruster firings along the yaw axis can be seen in the linear accelerations along the radial direction starting from day 140 near the “bottom” ascending equator (AE) in Fig. 5.4, lower panel. The sudden increase in the cross-track accelerations (marked as ‘2’ in the upper panel of Fig. 5.4) is dependent on the temperature differences shown in Fig. 5.3 (b.). Sudden changes in the cross-track accelerations marked with ‘4’ in the upper panel are due to the Center Of Mass (COM) calibrations in GRACE-B. More systematics in the two accelerometers are shown in panels (a) & (b) of Figs. 5.7 & 5.8 for the years 2007 and 2008. They are further discussed while analyzing the range-rate residuals in the following section.

5.3 Range-rate residual analysis with focus on accelerometer errors

Accelerometer observations do not only represent surface accelerations, but they are also very sensitive to other systematic effects. Such systematics can be due to inner and outer changes in the environment of the spacecraft. Since the accelerometer characteristics are more prominent at the low frequencies, their inaccuracies can directly affect the low degrees of the recovered global gravity field solutions. The accelerometer errors can easily get coupled into the inter-satellite range-rate observations during the reduction of non-gravitational forces which is done as

$$\delta\dot{\rho} = \dot{\rho}_{KBR} - \dot{\rho}_{acc} - \dot{\rho}_{others}, \quad 5.3$$

where $\dot{\rho}_{KBR}$ are the KBR range-rate observations, $\dot{\rho}_{acc}$ represent the contribution of the non-gravitational forces, $\dot{\rho}_{others}$ from the rest of the forces mentioned in Table 2.2 which are reduced from the range-rate observations.

Through the analysis of the range-rate residuals, the errors affecting the gravity

field solutions can be studied. The knowledge of the factors which cause such errors is critical to model or re-calibrate them precisely. This section provides the analysis of the range-rate residuals with focus on systematic errors contributed by the accelerometers. The residuals are computed after estimating the gravity field parameters. Note that the parameters are estimated using the ITSG-2014 processing chain. There also, the GRACE level 1B accelerometer data is adjusted for initial scale and bias parameters using Eq. 5.2. Then the accelerometer data is rotated into the ECI frame of reference using Eq. 3.2. The rotation matrix is computed from the attitude quaternions. The range-rate observations are one-dimensional along-track observations. In order to correct the effects of non-gravitational forces, the forces are reduced from the range-rates during the non-linear orbit integration step.

During reduction, errors in all three axes get coupled to the range-rate observations. Since the observations are used as input for gravity field modeling, the errors are likely to propagate into the estimated parameters. Because the errors partially end up in the residuals, the residuals are analyzed to identify such errors and their source. Since the periodic scale and bias parameters are also estimated during the gravity field recovery, it is possible that the residuals may not reflect most of the errors in the accelerometer data. Hence by analyzing the residuals, it is of interest to identify the errors which are still present.

Referring to Fig. 5.2 which shows the error models of the three accelerometer axes, it is clear that the accelerometer errors are large in the low-frequency regime, i.e. 0.1 - 10 mHz. Their magnitude varies by several orders in different frequency bands. For example, the error curves of the three accelerometer axes are several orders of magnitude larger in the frequency range 0.1 - 0.9 mHz as compared to the frequency range 1 - 10 mHz. Thus, it becomes necessary to consider the errors in different bandwidths distinctly. Therefore, a band-pass filter is applied to analyze the residuals in frequencies between 0.1 - 0.9 mHz and 1 - 9 mHz separately (refer to patch '1' and '2' shown in Fig. 5.2 for the two frequency bands). The band-pass filters are constructed using the LTPDA toolbox (Hewitson, 2007). Only frequencies until 9 mHz are considered in this analysis because beyond that, the KBR system noise starts to dominate which can lead to an incorrect interpretation of the error characteristics. A two-year long time-series is analyzed and its error characteristics are presented in the following sections. First, the error analysis is presented in

the time domain. Second, the filtered residual are studied along the *argument of latitude* and time in days, to discuss the systematics which may not be visible in the time-series plots.

Time-series analysis of the errors in the range-rate residuals

To analyze the range-rate residuals in the time domain, they are filtered in three frequency bands which are

- 0.1 - 0.9 mHz (1 - 5 CPR) – panel (c.) of Figs. 5.7 & 5.8
- 1 - 5 mHz (6 - 28 CPR) – panel (d.) of Figs. 5.7 & 5.8
- 5 - 9 mHz (28 - 56 CPR) – panel (e.) of Figs. 5.7 & 5.8

The patch ‘2’ of Fig. 5.2 is divided into two frequency bands because of the interest in understanding the characteristics of even the smallest errors. Thus, the patch ‘2’ of Fig. 5.2 corresponds to the panels (d.), (e.) in Figs. 5.7 & 5.8.

In Fig. 5.7 (c.), the post-fit residuals in the frequency bandwidth of 0.1 - 0.9 mHz are shown on a time-series for the year 2007. Similarly, in Fig. 5.8 (c.), the post-fit residuals for the same frequency band are shown for 2008. The linear accelerations of the two accelerometers (of GRACE-A and GRACE-B) along the three axes are also plotted in panels (a.) & (b.) in both figures, i.e. Figs. 5.7 & 5.8. In the time-series, it is clearly seen that the linear accelerations in the cross-track and the radial directions are disturbed more than in the along-track direction. As they all couple to the range-rates, the errors in the range-rate residuals are caused by all three axes of accelerometers. The disturbances due to the Disabling of Supplemental Heater Lines (DSHL) events are large in the cross-track direction. The DSHL events are activated to maintain the inner temperature of the satellite with respect to the temperature of the outer space. These events are also called low voltage events because they are used to reduce the power load with lower temperature settings in the heaters (Beerer and Massmann, 2007). Such events are activated for the duration of one to two days. They lead to large errors in the range-rate residuals. These errors last for even a longer duration compared to the duration when the DSHL events occur in the accelerometers. The amplitude of the range-rate residuals due to such

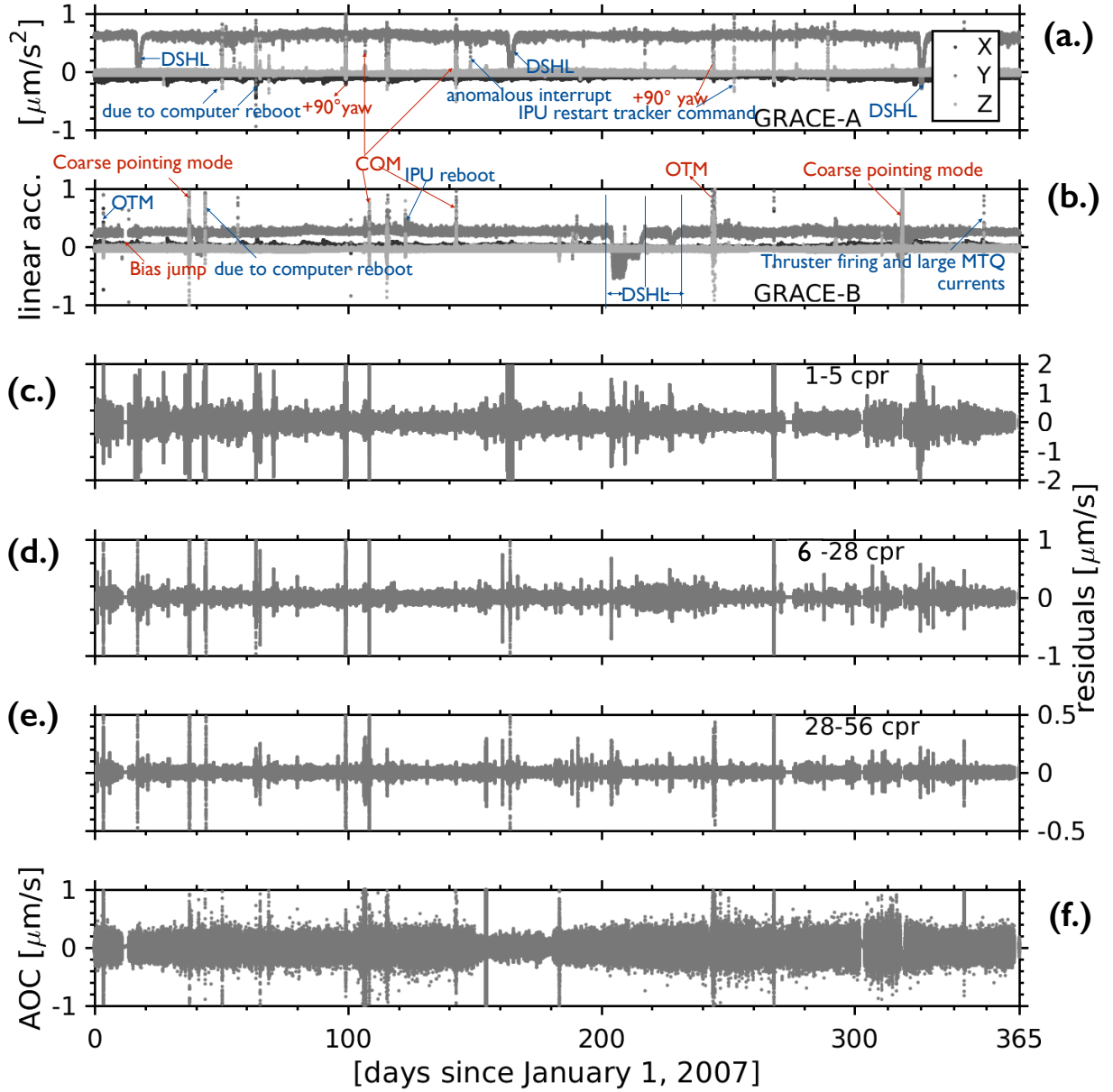


Figure 5.7: The linear accelerations of GRACE-A & B are shown in panel (a) and (b). The range-rate residuals decomposed into various frequency bands are shown in panel (c, d, e). Panel (f) shows the antenna offset corrections (AOC) for the year 2007.

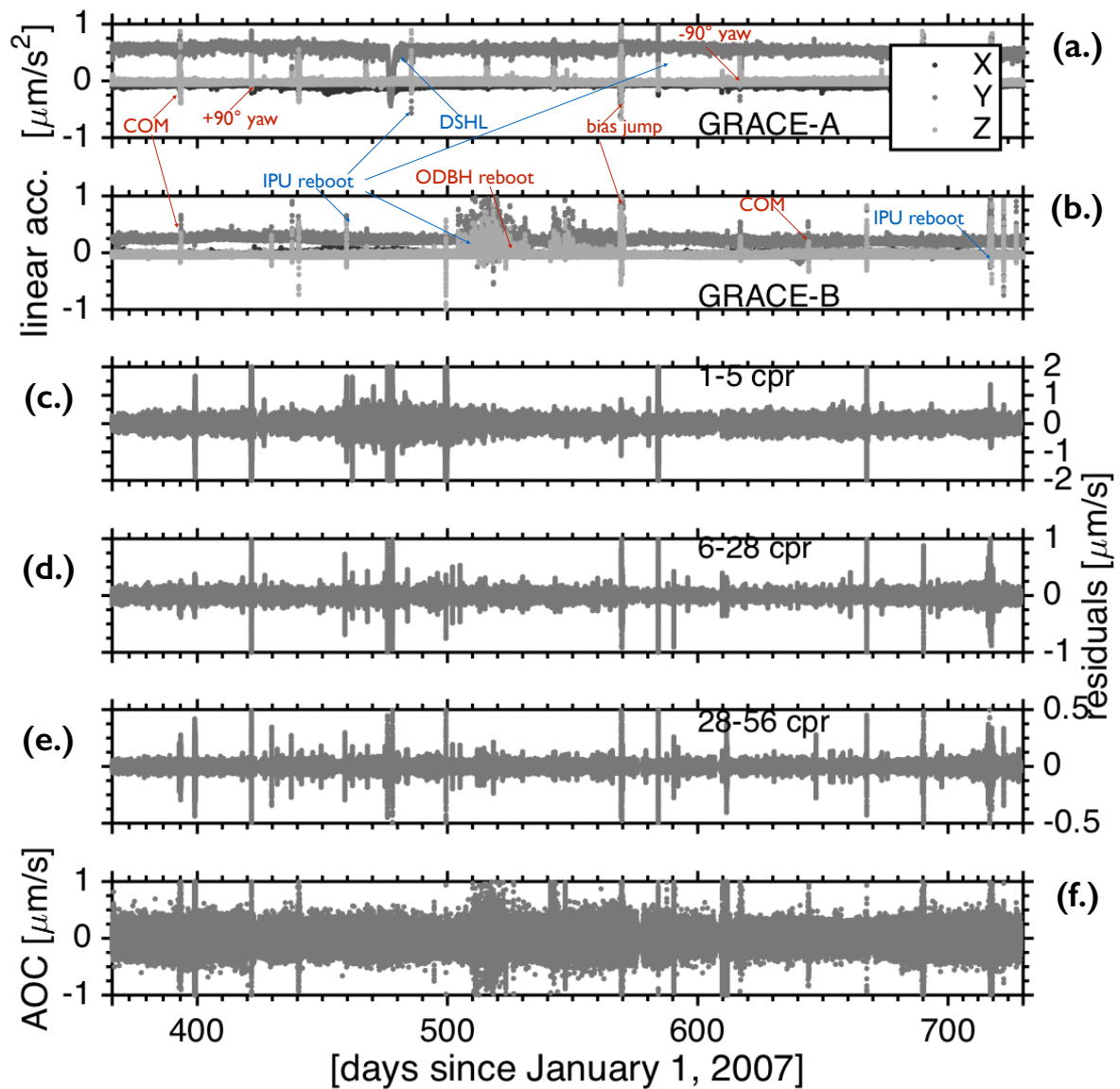


Figure 5.8: The linear accelerations of GRACE-A & B are shown in panel (a) and (b). The range-rate residuals decomposed into various frequency bands are shown in panel (c, d, e). Panel (f) shows the antenna offset corrections (AOC) for the year 2008.

systematic effects reaches up to $\pm 2.5 \mu\text{m/s}$ every time when such disturbances occur in the accelerometer data.

Another large error contributor in the residuals is the Center of Mass (COM) calibration maneuvers. The COM calibrations are required to minimize the offset between the accelerometer's proof mass and the COM of the spacecraft which is a consequence of the spacecraft's geometry. Large offsets can lead to significantly large errors in the accelerometer observations. Studies of Wang (2003) have shown that the effects of large offsets can be significant in the gravity field solutions if they are not treated properly. That is why, in the real mission, first the offset is determined then the center of mass trim assembly is used to minimize that offset. Such calibration maneuvers can lead to big jumps in the accelerometer data due to the high-sensitive nature of the instrument. Due to their improper or no treatment in the gravity field determination process, jumps related to these events are present in the range-rate residuals. The presence of such jumps in the residuals shows that the range-rate observations are affected by such maneuvers and may leave an impact on the gravity field solutions.

The presence of these errors in the range-rate residuals indicate the need to improve the existing data pre-processing strategies to prevent the propagation of systematic errors related to temperature effects, heating control mechanisms and calibration maneuvers into the gravity field solutions. If such errors are handled properly in gravity field processing, either they would not appear at all or the amplitude of the residuals due to such errors would be within the precision limits of the range-rate observations. In addition to calibration maneuvers, IPU (Instrument Processing Unit) restart commands lead to sudden glitches in the accelerometer observations. Sometimes the IPU restarts due to unknown reasons. The effects caused by such glitches are also reflected in the post-fit residuals. The amplitude of the residuals due to these errors is mainly within the range of $\pm 1 \mu\text{m/s}$, but sometimes it reaches up to $\pm 2 \mu\text{m/s}$. The desired noise level in range-rate residuals is $\pm 1 \mu\text{m/s}$. The maneuvers performed to save cell and battery life on the spacecraft such as yaw turns of the satellite also lead to spikes in the residuals which can be again up to $\pm 2 \mu\text{m/s}$ in amplitude.

Note that in the ITSG-2014 data pre-processing scheme, attempts were made to filter such effects by applying a threshold based outlier detection method on the

accelerometer time-series. As discussed in the previous section, the bias parameters and scale factors keep changing with time. Hence, the threshold based outlier detection can not be an effective strategy. That is why still existing errors in range-rate observations are reflected in their residuals.

The main findings are:

Firstly, the range-rate residuals contain the errors from all three axes altogether. The linear accelerations are used in the orbit integration step where they are used to compute the reference orbit. Then reference range-rate observations are computed from the reference orbit. The presence of systematic effects of three axes is obviously expected in the range-rate observations and in the parameters estimated from those observations. As shown in Figs. 5.7 & 5.8 (panels (a.) & (b.)), most of the accelerometer disturbances affect the cross-track and radial direction. Accelerations in the along-track direction are comparably smoother than the other two, but range-rate observations are affected by the disturbances in all three axes.

Secondly, the errors in the range-rate residuals, due to the above mentioned systematic effects in the accelerometer data, are present at all frequencies (cf. panels (c.), (d.) & (e.) of Figs. 5.7 & 5.8). Here, systematic effects are caused by temperature fluctuations, satellite orbit control maneuvers, other small maneuvers. In other words, their power is distributed over the entire measurement bandwidth. Their amplitudes are large at low frequencies (0.1 - 0.9 mHz *or* 1 - 5 CPR) and small at high frequencies (1 - 5 mHz & 5 - 9 mHz). These errors are deterministic in nature which means, their epochs can be determined and they can be eliminated during data pre-processing.

Thirdly, the above discussed periodic systematic effects do not only affect the accelerometer observations but also the attitude observations. Thus, the source of the systematic errors seen in the range-rate residuals is not limited to the accelerometers. For example, most of the orbit control and the mass calibration maneuvers also affect the ranging observations which can be seen in the range-rate antenna offset phase center (AOC) variations shown in panel (f.) of Figs. 5.7 & 5.8. As also discussed in Chapter 3, range-rate residuals in the frequency band 3 - 9 mHz are affected by the attitude errors propagating through the AOC observations. Thus, it is obvious that the AOC are another source of systematic errors at these frequencies. This makes it complicated to separate the errors solely due to the accelerometer

behavior in the range-rate residuals and investigate their impact.

Another problem is that the errors in the geophysical background models are also present in the same frequency bandwidth as the accelerometer errors. In order to show the overlap of errors from the background models, the errors in one of the models are analyzed in the following.

The biggest error contributors of all background models are ocean tides and the atmosphere and ocean dealiasing (AOD) model (Ditmar et al., 2012). In the ITSG-2014 gravity field processing scheme, the EOT11a model has been used to reduce the ocean tides (Savcenko and Bosch, 2012). The AOD1B rl05 product (Dobslaw et al., 2013a) is used to reduce the non-tidal high-frequency atmospheric and oceanic mass variations from the range-rates. Inaccuracies in them also increase the errors in the range-rate observations and, hence, in the gravity field solutions.

To identify the errors related to the AOD model in the residuals, two releases of AOD1B products are taken, i.e. AOD1B rl04 and AOD1B rl05. A monthly gravity field solution without considering the AOD1B in the ITSG-2014 gravity field processing chain has also been computed and its residuals (denoted as (c) in top panel of Fig. 5.9) are compared along with the other two sets of residuals (denoted as (a) and (b) in the top panel of Fig. 5.9). The three sets of residuals are computed after parameter estimation where only the AOD1B product has been changed every time in the ITSG-2014 processing chain. The frequency band 0.4 - 6 mHz is largely affected every time due to the difference in the AOD1B product as shown in the top panel of Fig. 5.9. The differences between the sets of residuals also indicate the same. That is, in low frequencies, the differences between the residual sets are small as compared to the differences in the frequency band 0.4 - 6 mHz. Differences between set (a)-(c) and (b)-(c) are roughly two orders of magnitude above than the accelerometer noise model along x -, z - axes in this frequency band. The differences between (a)-(b), though small are still several factors above the desired noise level. It clearly indicates that errors in the geophysical background models are also dominant in these frequencies and overlap with the accelerometer sensor errors. The region where background model errors are large, can be clearly seen when the residuals are represented along the orbit (ascending arc only) as shown in the bottom panel of Fig. 5.9. It shows the distribution of the ocean tides (Savcenko and Bosch, 2012) and AOD1B product errors (Dobslaw et al., 2013b) on the globe. The inseparable

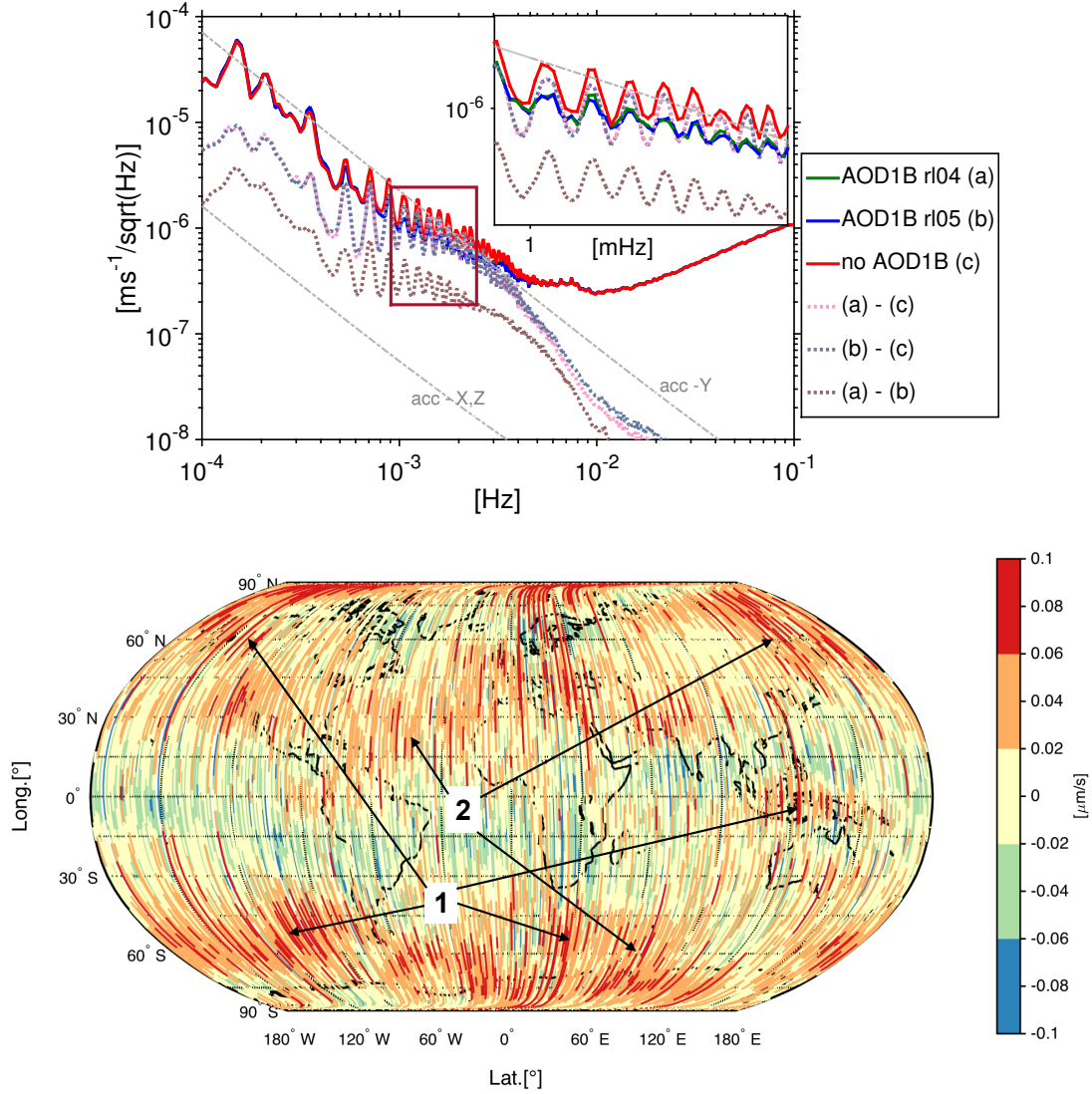


Figure 5.9: Top panel: PSDs of range-rate residuals computed using different AOD products are compared together with the differences between them. Tiny differences are shown as zoom-in plot in the upper right corner of the PSD plot. Bottom panel: Residuals (b) in the frequency band 0.4 - 6 mHz are plotted along the ascending arc for July 2007. ‘1’ – errors in the AOD1B rl05 model; ‘2’ – errors in the ocean tide model.

errors due to both background models are present in these frequencies. A detailed analysis of the geophysical background model errors in the range-rate residuals is beyond the scope of this thesis.

The coupling of such errors in the interested frequency band for accelerometer data analysis makes it even more complicated to separate the errors specifically due to one single source and quantify them.

In the time-series representation, very large systematic errors in the range-rate residuals can be analyzed well, but small systematic errors are hard to detect. For example, residuals along the orbit (bottom panel of Fig. 5.9) reflect the error characteristics which vary geographically. Thus, the orbit information is also an important factor to be used for a detailed analysis. Therefore, the residuals are further investigated in the *argument of latitude* and time representation in the following section.

Analyzing the error variations w.r.t orbit and time

Analyzing the range-rate residuals in the *argument of latitude* (AOL) versus time domain is helpful for identifying smaller systematic errors and finding their possible sources. Here, the residuals are analyzed in two frequency bands individually shown as patch ‘1’ & ‘2’ in Fig. 5.2.

Patch 1 (0.1-0.9 mHz or 1-5 CPR)

In this frequency band, most of the large systematic errors are present. The errors due to the temperature changes, DSHL events, COM calibration events, thruster firings are highly visible as vertical stripes in Fig. 5.10. The color scale is adjusted to highlight other small errors which were hard to identify in the time-series analysis. In Fig. 5.10, such errors are marked as ‘1’.

The box highlighted in the region near the poles is marked as ‘2’. It shows high amplitudes of residuals changing periodically. These are the errors from the geophysical background models which are also shown in the bottom panel of Fig. 5.9. The vertical stripes marked with number ‘3’ appear when the currents in the magnetic torquer rods change after the 161 d period depending on the accuracy of the active star camera head for the attitude determination. It has been discussed in Section 5.2 that the attitude control actuators affect the linear accelerations (cf.

Fig. 5.6). Earlier, Peterseim et al. (2012) have also studied the magnetic torquer induced signals in the accelerometers of the GRACE satellites. Such effects in the post-fit residuals can be attributed to signals present in the accelerometer data which are induced by magnetic torquer rod currents. At the same time, the pitch and yaw angles show variations depending upon the active star camera head. Thus, these vertical stripes come from the attitude variations and the accelerometers. Similarly, the vertical stripes of high residual values marked as ‘4’ are due to signals induced by the strong magnetic torquer rod currents during the times when strong attitude control was required. The effects in the residuals due to high currents are very random in nature. For example, for some days the amplitude of the residuals are high only for the duration when the high currents were flowing. But for other days, the duration is a little longer (stays for one whole orbit) than the duration in which the currents were activated. The source of such effects are again the accelerometers and the attitude observations together as they both are affected by the high currents in the magnetic torquer rods.

In Section 5.2, the dependencies of across-track linear accelerations on the temperature differences between the starboard and the port panel have been discussed. Such differences in temperature cause a periodic bias in the accelerations. This occurs every 161 days due to its dependence on the beta prime angle. It corresponds to the band of large residuals that are observed every 161 days. For example, the solid box shown in blue color and marked with number ‘5’ in Fig. 5.10 indicates the large amplitude of the residuals for a number of days during the entire orbit. There are also other bands near day ~ 160 and ~ 320 present in the range-rate residuals where the amplitudes of the residuals are large and seem to depend on the same factors. Although bias parameters are estimated every three hours, the errors in the range-rate residuals are still large during such strong transitions in radiation pressure. Another important point is that such periodic patches of high amplitudes of the residuals occur only when the differences in temperatures shown in panel (b.) of Fig. 5.3 change from negative to positive scale.

Patch 2 (1-9 mHz *or* 6-56 CPR)

This part of the error spectrum is one of the most entangled ones of the GRACE. The GRACE community is especially interested in disentangling this frequency band

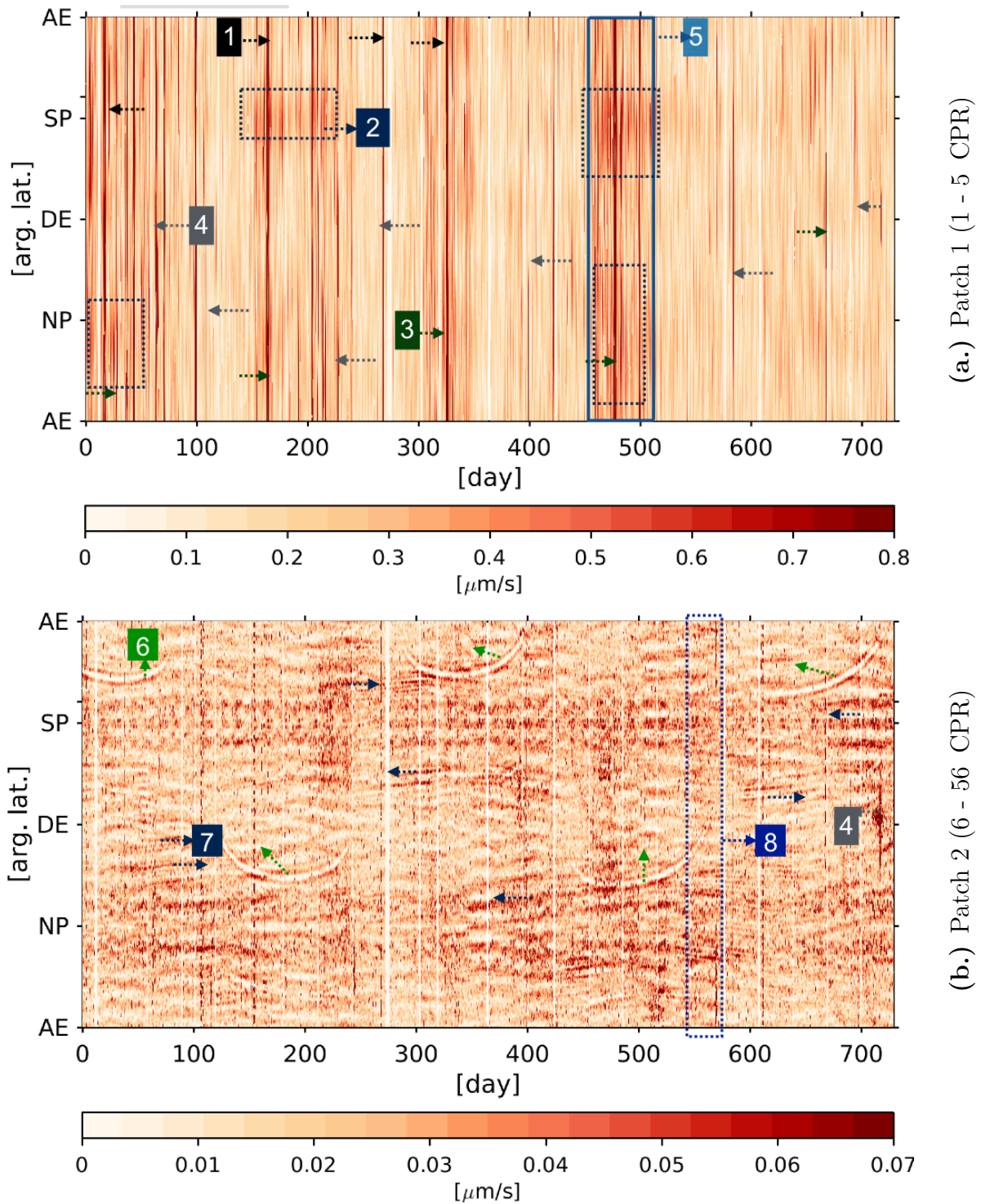


Figure 5.10: Plots (a.) & (b.) represent the residuals of two years in the two frequency bands shown as patch ‘1’ & ‘2’ in Fig. 5.2. The different errors in the residuals are marked with different colors. The arrows marked with the same color represent similar error causes.

because a major part of the gravity field signal lies in this range, i.e. in the spherical harmonic degrees ≈ 5 to 60. The errors in this frequency range are very important to be known, because there, the accuracy of the gravity field solutions is still an order of magnitude smaller than the GRACE baseline. Therefore, this frequency band has always been the topic of discussion. The main question is *the source of errors contributing to this part of the spectrum*. Earlier, the group of researchers at TU Delft (Ditmar et al., 2012) attempted to provide a GRACE error budget and modeling of the noise in different frequencies. For the frequency band 1 - 9 mHz, a noise model was developed based on the spectral characteristics, but responsible error sources were not identified. The efforts continued and an analysis of the star camera errors was presented by Inácio et al. (2015). They showed that the pointing errors are one of the many error sources in the frequency band of 1 - 9 mHz.

It has been shown in Chapter 3, that pointing errors highly dominate in the frequencies between about 5 and 10 mHz which is a part of the frequency range 1 - 10 mHz. In the time-series analysis, it is shown that the range-rate residuals in this frequency band contain errors from the attitude data and the accelerometers. When the residuals are considered on the *argument of latitude* and time, more systematic errors are revealed. In Fig. 5.10 (b.), residuals in the frequency band patch ‘2’ are shown. The residuals in these frequencies contain attitude errors visible as horizontal bands which are due to the varying relative attitude of the two satellites. They are related to the pitch and yaw angle variations of the spacecraft. Pitch angle variations are shown in panel (2) of Fig. 3.4. The pitch and yaw dependent horizontal bands are present in the entire two-year long time-series. The amplitudes of the residuals in these horizontal bands are high at certain places, see, for example the dark blue arrows numbered ‘7’ in Fig. 5.10 (b.), around day 200 (near DE) and day 700 (near SP). They are caused by the activation of strong magnetic torquer rod currents to control the attitude. Thrusters are also fired at the same time.

There is a distinguished patch marked with number ‘8’. The errors in this patch are contributed partly by the effects of magnetic torquer rod currents in the accelerometers and partly by the sudden bias jump occurred on this day in the along-track axis of GRACE-B (cf. Fig. 5.4, day 182).

When the satellite transits from the Sun into the shadow, a small bias is induced in the linear accelerations. The errors related to the bias change appear partially as the

signature of shadow in the residuals (mark ‘6’ in Fig. 5.10). In Section 5.2, we found that the linear accelerations increase due to the increased temperature differences between front and rear panels. The accelerations decrease when the temperature differences are small. Shadow signatures are obtained in the residuals when there is an increase in the magnitude of the accelerations. On the other hand, no signatures related to shadow are seen when the magnitude of the linear accelerations decrease. One possible explanation is that the shadow effects are partially absorbed by the accelerometer scale and bias parameters which are estimated during the least-squares parameter estimation. Another possibility is that they are absorbed by the global spherical harmonic coefficients and thus reduce the precision of the gravity field solutions. Those investigations are out of scope of this work.

5.4 Summary

In this chapter, the GRACE accelerometers and the characteristics of the linear accelerations are discussed. The ACC1B dataset is used to describe the characteristics of accelerometer data. The ACC1B data is different from the ACC1A data in a way that ACC1A is low-pass filtered (cut-off frequency 35 mHz) using the CRN digital filter and is time-tagged to match the GPS receiver time (Wu et al., 2006).

The main problems in the accelerometer data are scale factor and bias parameters. The precise calibration of these scale and bias parameters is still a problem today. The unknown scales and biases are already present in the raw accelerometer observations. In addition, they experience sudden changes due to temperature and voltage changes in the spacecraft (cf. Fig. 5.6). The linear accelerations experience disturbances continuously from the attitude control actuators. Effects of high magnetic torquer rod currents can be seen in the linear accelerations in cross-track and radial direction (cf. Fig. 5.4). The satellite orbit control maneuvers such as calibration of the COM or yaw axis turns also lead to sudden jumps in the linear accelerations.

In section 5.3, the analysis of the residuals is presented with focus on the errors contributed by the accelerometers. The analysis of the post-fit residuals revealed that they contain strong signatures of the temperature and orbit control maneuvers dependent errors which affect the accelerometer observations. The signatures of the errors related to sudden bias changes in the linear accelerations have also been iden-

tified in the range-rate residuals. This clearly indicates the need to further improve the accelerometer calibration strategy for gravity field processing. The presence of such errors in the range-rate residuals at low frequencies (0.1 - 0.9 mHz) is also an indication that these errors affect the quality of the global gravity field solutions. The impact on the gravity field can be small because accelerations are partly absorbed by scale and bias parameters determined during parameter estimation.

First, the results of analysis of residuals are presented in the time domain, and second, with respect to the *argument of latitude* and time. The range-rate residuals are analyzed by filtering them in different frequency bands. The frequency bands are selected on the basis of differences in the noise power of the range-rate residuals. The time-series analysis of the range-rate residuals is carried out in three frequency bands, 0.1 - 0.9 mHz, 1 - 5 mHz and 5 - 9 mHz.

Systematic errors due to temperature variations and satellite maneuvers affect the entire frequency spectrum which can be seen in the filtered residuals in different frequency bandwidths (cf. Figs. 5.7 & 5.8). The residuals are decomposed into two frequency bands (cf. Patch ‘1’ & ‘2’ of Fig. 5.2). The large errors due to the magnetic torque actuation are found in the range-rate residuals. The cross-track and radial linear accelerations are mainly responsible for such errors. The errors from the geophysical background models such as AOD1B and ocean tide EOT11a model were also considered. They overlap in the same frequency band where the accelerometer errors are present. Strong signatures of the changes in linear accelerations in shadow areas are present in the frequency band 1 - 9 mHz. The attitude errors are another big error source in this frequency band.

Systematic errors present in the accelerometer observations can be reduced in the range-rate observations by adopting an extensive approach of accelerometer data preprocessing. Similarly, periodic bias changes can be reduced by improving the accelerometer calibration strategy. An adoption of improved data preprocessing and a precise calibration approach can be helpful in improving the gravity field accuracy, thus reducing the amplitudes of the residuals. As a result of the continuous ongoing efforts, Klinger and Mayer-Gürr (2016) described and modeled the systematics present in the accelerometer data. Significant improvements have been achieved in the gravity field solutions after careful handling of the accelerometer data. The improved gravity field solutions are released as ITSG-2016 models. They also showed

the significant improvement in the degree 2 coefficients. However, still better strategies are needed to be developed in the near future.

III

Conclusions

This study provides a comprehensive analysis of the range-rate residuals which is an absolutely necessary step to improve the estimation chain of gravity field parameters. With this analysis, it is shown that the residuals contain a large number of systematic errors. Their sources are investigated and widely explained in this work. Due to their deterministic behavior, it is possible to reduce them from the range-rate observations. The reduction of such effects is important to avoid their propagation into the gravity field parameters. So far, studies have mainly been published on the accuracy assessment of recovered gravity field solutions. Analyzing the range-rate residuals gave new insight about the contribution of various errors. The sources of such errors have been investigated by analyzing the satellite observations, studying their propagation to the range-rate observations and understanding the systematics reflected in the post-fit residuals.

In order to identify individual effects in observations and residuals, we used various methods such as correlation analysis or pattern matching, analysis of causal factors of the errors by investigating further related datasets, etc. The satellite observations and the residuals, both contain many systematic effects together.

The major findings of our analyses are:

- Analysis of range-rate residuals with focus on the attitude errors reveals large errors in the residuals computed using the star camera only attitude product as opposed to the fused attitude product. These results are consistent with the previous studies, e.g., Mayer-Gürr et al. (2014) where it has been shown that the fused attitude product performs better than the star camera only product.

The differences in the accuracy of the two star camera heads affect the performance of the fused datasets. When the more accurate star camera head was active, an improved performance of the fused attitude data (star cameras + angular accelerations) was not significant, whereas, when the less accurate star camera head was active for attitude determination, the fused attitude data was more precise.

From the residual analysis of the noise present in the GRACE attitude datasets, it is deduced that the fused attitude dataset obtained by combining the data

from star cameras, angular accelerations and IMUs should be used in comparison to the star camera only attitude. These findings are consistent with the previous analysis studies done by Bandikova (2015) and Inácio et al. (2015).

- The analysis of the range-rate residuals for the attitude errors revealed that the major amount of the attitude errors propagate through the antenna phase center offset corrections (AOC) which are added to the range-rate observations. The errors propagated via AOC are predominantly due to high pitch and yaw errors. Thus in future, the precision of inter-satellite pointing along the pitch and yaw axes must be improved in order to minimize the attitude errors in the GRACE range-rate observations.
- The most dominating ranging errors in the range-rate residuals are due to the KBR system noise which is present at the high frequencies of the GRACE error spectrum. The KBR system noise comprises of the phase errors of the four frequencies used to measure the range changes. The phase errors of one of the four frequencies lead to very high systematic noise in the range-rate observations which again appears in the residuals. The noise in the phase observations is caused by temperature variations in the instrument and by star camera intrusions. The mitigation of these errors is required either at the instrument level or in the gravity field modeling.
- The analysis of the range-rate residuals for accelerometer errors revealed that these errors are highly dominated by the errors in the linear accelerations along the cross-track axis. Additionally, the errors in the accelerations along the radial axis are noticeable in the residuals.
- We understand that the accelerometer errors can be reduced in the range-rate observations by adopting improved data preprocessing and calibration strategies. This would minimize the range-rate residuals. Improved modeling of those effects during gravity field recovery increases the precision of the estimated gravity field parameters. One of the recent examples is given by Klinger and Mayer-Gürr (2016). Similar strategies can be adopted for GRACE Follow-On.
- The GRACE twin satellites were supposed to be identical in terms of their

payload performance. But we realized that there are differences in the performance of the two payloads, which is well reflected in the range-rate residuals.

The future *potential* of this study is:

- ▷ There remains a scope of refinement of the analysis strategies, such as the implementation of better signal separation methods or the use of better filters applied on the residuals.

In future, including the analysis of orbit residuals and empirical parameters seems promising. Those measures would help in better realizing the mapping of various errors in the gravity field parameters.

- ▷ Post-fit residual analysis for GRACE Follow-On: The mission uses a similar measurement principle but with two ranging instruments, i.e. KBR microwave assembly and Laser Ranging Interferometer. Since the gravity field models will then be computed from two types of ranging instruments, their residual analysis will contain the systematics due to each type of observations. Both data can be used for cross-checks and separating related error sources. The artefacts or systematic errors can then further be corrected by improving the data processing strategies or by implementing dedicated maneuvers.

Besides this, the level 1A data of the satellites will be published for the first time after the commissioning phase (as announced by Dr. Gerhard Kruizinga in GRACE Science Team Meeting, UT Austin, Texas). Since level 1B data are processed from level 1A observations, it is possible to identify the data characteristics in level 1A and to understand how they propagate to the range-rate residuals. Thus, availability of the level 1A data will be helpful in enhancing the current analysis methods.

Appendices

Appendix **A**: Inter-satellite pointing angles and the satellite panels

A.1 Computation of GRACE inter-satellite pointing angles

Pointing variations in a spacecraft are defined as the rotations about its roll, pitch and yaw axes. The corresponding roll, pitch and yaw angles (see Fig. 3.1) are also called Euler angles or inter-satellite pointing angles in GRACE. The pointing angles analyzed in chapter 3 are computed in the GRACE line of sight reference frame. Ideally, the line of sight should coincide with the GRACE antenna phase center but in reality it is not the case. There is a slight deviation between the line joining the satellite's centre of mass (COM) and the antenna phase center, and the GRACE line of sight. Therefore, there is a rotation involved to transform from the K-Frame of which the x-axis is the line joining the satellite's centre of mass and the K-band horn or antenna phase center to the line of sight (LOS) frame. To compute the pointing variations about the LOS, 3-step approach is followed.

The direction cosine matrix which is computed from the rotation matrices obtained from the roll (ψ), pitch (Θ) and yaw (ϕ) angles is defined as

$$\mathbf{R} = \mathbf{R}_1(\psi) \mathbf{R}_2(\Theta) \mathbf{R}_3(\phi)$$

$$\mathbf{R} = \begin{pmatrix} c_\Theta c_\phi & c_\Theta s_\phi & -s_\Theta \\ -c_\psi s_\phi + s_\psi s_\Theta c_\phi & c_\psi c_\phi + s_\psi s_\Theta s_\phi & s_\psi c_\Theta \\ s_\psi s_\phi + c_\psi s_\Theta c_\phi & s_\psi c_\phi + c_\psi s_\Theta s_\phi & c_\psi c_\Theta \end{pmatrix} \quad \text{A.1}$$

where,

$$\begin{aligned} c_\Theta &= \cos(\Theta) & s_\Theta &= \sin(\Theta) \\ c_\phi &= \cos(\phi) & s_\phi &= \sin(\phi) \\ c_\psi &= \cos(\psi) & s_\psi &= \sin(\psi) \end{aligned} \quad \text{A.2}$$

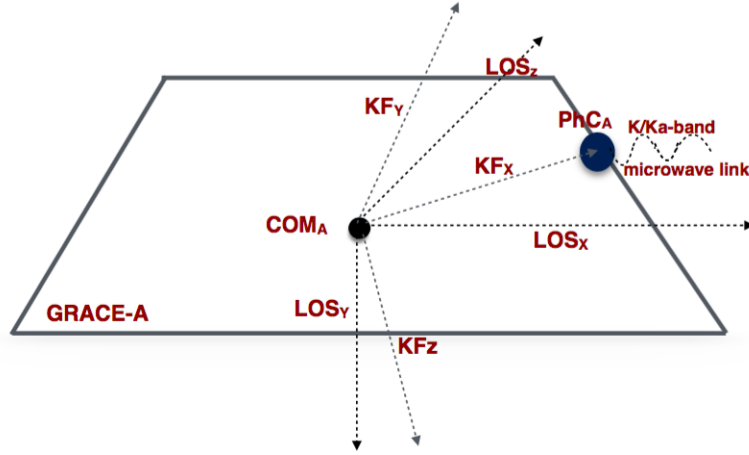


Figure A.1: Representation of LOS frame and K-Frame for GRACE-A satellite. The K-Frame of reference is the instrument frame of the K-band ranging instrument, the LOS frame represents the virtual frame of reference, the x-axis of which should be pointing along the line of sight (LOS).

The roll (ψ), pitch (Θ) and yaw (ϕ) angles can be obtained from matrix \mathbf{R} as

$$\begin{aligned}\psi &= -\arctan\left(\frac{\mathbf{R}_{23}}{\mathbf{R}_{33}}\right) \\ \Theta &= -\arcsin\left(\mathbf{R}_{13}\right) \\ \phi &= -\arctan\left(\frac{\mathbf{R}_{12}}{\mathbf{R}_{11}}\right)\end{aligned}\tag{A.3}$$

The rotation matrix \mathbf{R} is obtained from the dot product of other two matrices

$$\mathbf{R} = \mathbf{R}_{\text{ECI}}^{\text{KF}} \cdot \left(\mathbf{R}_{\text{ECI}}^{\text{LOS}}\right)^{\text{T}}\tag{A.4}$$

where, $\mathbf{R}_{\text{ECI}}^{\text{KF}}$ and $\mathbf{R}_{\text{ECI}}^{\text{LOS}}$ are the matrices rotating from Earth-Centered Inertial (ECI) frame to the K-Frame of reference and the LOS frame of reference, respectively. The dot product of these two matrices gives a matrix rotating from the K-Frame to the LOS frame of reference. Therefore, \mathbf{R} can also be written as $\mathbf{R}_{\text{KF}}^{\text{LOS}}$. For the definition of the K-Frame and LOS frame of reference see Fig. A.1. The 3-step approach is as follows (Bandikova et al., 2012):

1. Computation of $\mathbf{R}_{\text{ECI}}^{\text{KF}}$

The matrix $\mathbf{R}_{\text{ECI}}^{\text{KF}}$ is computed from the calibrated antenna phase center (\mathbf{pc}_j) which is provided as VKB1B data and quaternions from the SCA1B data.¹

$$\mathbf{R}_{\text{ECI}}^{\text{KF}} = \begin{pmatrix} \left(\mathbf{R}_{\text{SRF}}^{\text{ECI}} \right)^{\text{T}} \frac{\mathbf{pc}_j}{|\mathbf{pc}_j|} \\ \mathbf{z}_{\text{KF}_j} \times \mathbf{x}_{\text{KF}_j} \\ \mathbf{x}_{\text{KF}_j} \times \mathbf{y}_{\text{SRF}_j} \end{pmatrix} \quad \text{A.5}$$

where \mathbf{x}_{KF_j} , \mathbf{y}_{KF_j} and \mathbf{z}_{KF_j} are the axes realizations of the K-band ranging instrument frame for spacecraft j . \mathbf{pc}_j is the position of the antenna phase center of a spacecraft j . $\mathbf{R}_{\text{SRF}}^{\text{ECI}}$ (matrix rotating from Science Reference Frame (SRF) to ECI frame of reference) is computed from the SCA1B quaternions as -

$$\mathbf{R}_{\text{SRF}}^{\text{ECI}} = \begin{pmatrix} 2q_0^2 - 1 + 2q_1^2 & 2q_1q_2 + 2q_0q_3 & 2q_1q_3 - 2q_0q_2 \\ 2q_1q_2 - 2q_0q_3 & 2q_0^2 - 1 + 2q_2^2 & 2q_2q_3 + 2q_0q_1 \\ 2q_1q_3 + 2q_0q_2 & 2q_2q_3 - 2q_0q_1 & 2q_0^2 - 1 + 2q_3^2 \end{pmatrix} \quad \text{A.6}$$

$\mathbf{y}_{\text{SRF}_j}$ can be taken from row 2 of $\mathbf{R}_{\text{SRF}}^{\text{ECI}}$.

2. Computation of $\mathbf{R}_{\text{ECI}}^{\text{LOS}}$

$$\mathbf{R}_{\text{ECI}}^{\text{LOS}} = \begin{pmatrix} \mathbf{x}_{\text{LOS}_j} \\ \mathbf{x}_{\text{LOS}_j} \times \frac{\mathbf{r}_A}{|\mathbf{r}_A|} \\ \mathbf{x}_{\text{LOS}_j} \times \mathbf{y}_{\text{LOS}_j} \end{pmatrix} \quad \text{A.7}$$

where, $\mathbf{x}_{\text{LOS}} = \frac{\mathbf{r}_A - \mathbf{r}_B}{|\mathbf{r}_A - \mathbf{r}_B|}$;

subscript A and B refer to GRACE-A and GRACE-B and the subscript LOS refers to the GRACE line of sight. \mathbf{r}_A refers to the position of GRACE-A in ECI frame of reference. The matrix $\mathbf{R}_{\text{ECI}}^{\text{LOS}}$ corresponds to the line of sight along GRACE-A.

3. Computation of the roll, pitch and yaw angles

After obtaining the two matrices, the matrix $\mathbf{R}_{\text{KF}}^{\text{LOS}}$ can be obtained from Eqn. A.4.

¹Quaternions is a set of four unitless quantities represented as q_0, q_1, q_2, q_3 . Here, q_0 denotes the scalar part and q_1, q_2, q_3 refer to the angular part.

A.2 Satellite panels

In chapter 5 (cf. Fig. 5.3), the data of Coarse Earth and Sun Sensors (CESS) are used to study the temperature variations on the different panels of the satellite. The different panels of the satellite with their names (Bettadpur, 2012) are introduced here. This naming convention has been used while discussing the CESS data of the GRACE satellites.

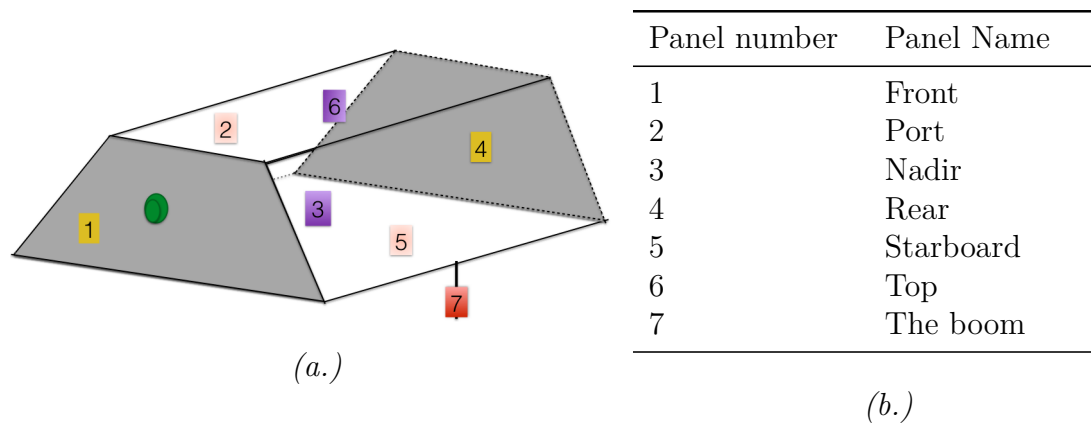


Figure A.2: (a.) View of the different panels of the GRACE satellites, (b.) Names of the panels.

- Adhikari, S., Ivins, E.R., 2016. Climate-driven polar motion: 2003–2015. *Science Advances* 2. doi:10.1126/sciadv.1501693.
- Bandikova, T., 2015. The role of attitude determination for inter-satellite ranging. Ph.D. Thesis. Institute of Geodesy, Leibniz University Hannover, Germany. URL: https://dgk.badw.de/fileadmin/user_upload/Files/DGK/docs/c-758.pdf.
- Bandikova, T., Flury, J., 2014. Improvement of the GRACE star camera data based on the revision of the combination method. *Advances in Space Research* 54, 1818–1827. doi:10.1016/j.asr.2014.07.004.
- Bandikova, T., Flury, J., Ko, U.D., 2012. Characteristics and accuracies of the GRACE inter-satellite pointing. *Advances in Space Research* 50, 123–135. doi:10.1016/j.asr.2012.03.011.
- Barthelmes, F., Köhler, W., 2016. International Centre for Global Earth Models (ICGEM). The Geodesists Handbook 2016, *Journal of Geodesy*. doi:10.1007/s00190-016-0948-z.
- Beerer, J.G., Massmann, F.H., 2007. Status GRACE Mission Operations, GRACE Science Team Meeting. GFZ Potsdam, Germany.
- Bettadpur, S., 2009. Recommendation for a-priori Bias and Scale Parameters for Level-1B ACC data (ver. 2). Technical Report 2. Center of Space Research, University of Texas Austin, US. URL: ftp://podaac.jpl.nasa.gov/allData/grace/docs/TN-02_ACC_CalInfo.pdf.
- Bettadpur, S., 2012. Gravity Recovery And Climate Experiment Product Specification Document. Technical Report GRACE 327-720. CSR, University of Texas Austin. URL: ftp://podaac.jpl.nasa.gov/allData/grace/docs/ProdSpecDoc_v4.6.pdf.
- Bezdek, A., 2010. Calibration of accelerometers aboard GRACE satellites by comparison with POD-based nongravitational accelerations. *Journal of Geodynamics* 50, 410–423. doi:10.1016/j.jog.2010.05.001.

- Bode, A., Biancale, R., 2006. Mean Annual and Seasonal Atmospheric Tide Models Based on 3-hourly and 6-hourly ECMWF Surface Pressure Data. Scientific Technical Report STR06/01. Deutsches GeoForschungsZentrum GFZ. URL: 10.2312/GFZ.b103-06011.
- Boening, C., Willis, J.K., Landerer, F.W., Nerem, R.S., Fasullo, J., 2012. The 2011 La Niña: So strong, the oceans fell. *Geophysical Research Letters* 39. doi:10.1029/2012GL053055.
- Bonin, J.A., Chambers, D.P., 2011. Evaluation of high-frequency oceanographic signal in GRACE data: Implications for de-aliasing. *Geophysical Research Letters* 38. doi:10.1029/2011GL048881.
- Calabia, A., Jin, S., Tanzer, R., 2015. A new GPS-based calibration of GRACE accelerometers using the arc-to-chord threshold uncovered sinusoidal disturbing signal. *Aerospace Science and Technology* 45, 265–271. doi:10.1016/j.ast.2015.05.013.
- Chambers, D.P., Bonin, J.A., 2012. Evaluation of Release-05 GRACE time-variable gravity coefficients over the ocean. *Ocean Science Discussions* 8, 859–868. doi:10.5194/os-8-859-2012.
- Chinnasamy, P., Maheshwari, B., Prathapar, S., 2015. Understanding Groundwater Storage Changes and Recharge in Rajasthan, India through Remote Sensing. *Water* 7, 5547–5565. doi:10.3390/w7105547.
- Clawson, J.F., 1991. Thermal Environments. Jet Propulsion Laboratory, NASA, USA.
- Curtis, H.D., 2005. *Orbital Mechanics for Engineering Students*. Number 0 7506 6169 0 in Elsevier Aerospace Engineering Series. 1 ed., Elsevier Butterworth-Heinemann Linacre House, Jordan Hill, Oxford.
- Ditmar, P., da Encarnação, J.T., Farahani, H.H., 2012. Understanding data noise in gravity field recovery on the basis of inter-satellite ranging measurements acquired by the satellite gravimetry mission GRACE. *Journal of Geodesy* 86, 441–465. doi:10.1007/s00190-011-0531-6.

- Ditmar, P., Klees, R., Liu, X., 2006. Frequency-dependent data weighting in global gravity field modeling from satellite data contaminated by non-stationary noise. *Journal of Geodesy* 81, 81–96. doi:10.1007/s00190-006-0074-4.
- Dobslaw, H., Flechtner, F., Bergmann-Wolf, I., Dahle, C., Dill, R., Esselborn, S., Sasgen, I., Thomas, M., 2013a. Simulating high-frequency atmosphere-ocean mass variability for dealiasing of satellite gravity observations: AOD1B RL05. *Journal of Geophysical Research: Oceans* 118, 3704–3711. doi:10.1002/jgrc.20271.
- Dobslaw, H., Flechtner, F., Bergmann-Wolf, I., Dahle, C., Dill, R., Esselborn, S., Sasgen, I., Thomas, M., 2013b. Simulating high-frequency atmosphere-ocean mass variability for dealiasing of satellite gravity observations: AOD1B RL05. *Journal of Geophysical Research: Oceans* 118, 3704–3711. doi:10.1002/jgrc.20271.
- Dong, F., Liao, H., Jia, C., Xia, X., 2009. Calibration and adjustment of center of mass (COM) based on EKF during in-flight phase. *Science in China Series E: Technological Sciences* 52, 1446–1449. doi:10.1007/s11431-009-0142-0.
- Dunn, C., Bertiger, W., Franklin, G., Harris, I., Kruizinga, G., Meehan, T., Nandi, S., Nguyen, D., Rogstad, T., Thomas, J.B., Tien, J., 2002. The Instrument on NASA's GRACE Mission: Augmentation of GPS to Achieve Unprecedented Gravity Field Measurements, Proceedings of the 15th International Technical Meeting of the Satellite Division of The Institute of Navigation (ION GPS 2002), Oregon Convention Center Portland, OR, US. URL: <https://trs.jpl.nasa.gov/bitstream/handle/2014/10401/02-2372.pdf?sequence=1&isAllowed=y>.
- Ellmer, M., Mayer-Gürr, T., 2016. High precision dynamic orbit integration for spaceborne gravimetry, Institute of Geodesy, Graz University of Technology, Austria. American Geophysical Union, San Francisco, US.
- Famiglietti, J.S., 2014. Epic California Drought and Groundwater: Where Do We Go From Here? URL: <https://blog.nationalgeographic.org/2014/02/04/epic-california-drought-and-groundwater-where-do-we-go-from-here/>.
- Flechtner, F., 2000. GRACE Payload. URL: <http://op.gfz-potsdam.de/grace/payload/payload.html>.

- Flechtner, F., Dobsław, H., Fagiolini, E., 2015. Gravity Recovery and Climate Experiment, AOD1B Product Description Document for Product Release 05. 2015. GeoForschungsZentrum, GFZ, Potsdam, Germany. URL: ftp://podaac.jpl.nasa.gov/allData/grace/docs/AOD1B_PDD_v4.4.pdf.
- Flury, J., Bandikova, T., Matschke, J., Apelbaum, G., Peterseim, N., Schlicht, A., 2012. Unexpected signals on GRACE from platform and environmental processes, European Geophysical Union, Vienna.
- Flury, J., Bettadpur, S., Tapley, B.D., 2008. Precise accelerometry onboard the GRACE gravity field satellite mission. *Advances in Space Research* 42, 1414–1423. doi:10.1016/j.asr.2008.05.004.
- Folkner, W., Williams, J., Boggs, H., 2009. The Planetary and Lunar Ephemeris DE 421. IPN Progress Report. URL: https://ipnpr.jpl.nasa.gov/progress_report/42-178/178C.pdf.
- Förste, C., Bruinsma, S., Abrikosov, O., Lemoine, J., Schaller, T., Götze, H., Ebbing, J., Marty, J., Flechtner, F., Balmino, G., Biancale, R., 2014. EIGEN-6C4 the latest combined global gravity field model including GOCE data up to degree and order 2190 of GFZ Potsdam and GRGS Toulouse, ICGEM, Potsdam, Germany. 5th GOCE User Workshop, Paris, 25. – 28.11.2014. URL: <http://icgem.gfz-potsdam.de/Foerste-et-al-EIGEN-6C4.pdf>.
- Frommknecht, B., 2007. Integrated Sensor Analysis of the GRACE Mission. Ph.D. Thesis. TU Munich, Germany.
- GeoForschungsZentrum, 2018. Geo Research Satellite GFZ-1. URL: <https://www.gfz-potsdam.de/en/section/global-geomonitoring-and-gravity-field/projects/abgeschlossene-projekte/geo-research-satellite-gfz-1/>.
- Goswami, S., Devaraju, B., Weigelt, M., Mayer-Gürr, T., 2018a. Analysis of GRACE range-rate residuals with focus on KBR instrument system noise. *Advances in Space Research* 62, 304–316. doi:10.1016/j.asr.2018.04.036.
- Goswami, S., Flury, J., 2016. Detecting the signatures of sensor errors in GRACE range-rate residuals, GRACE Science Team Meeting, Potsdam, Germany.

- Goswami, S., Klinger, B., Weigelt, M., Mayer-Gürr, T., 2018b. Analysis of Attitude Errors in GRACE Range-Rate Residuals – A Comparison Between SCA1B and the Fused Attitude Product (SCA1B + ACC1B). *IEEE Sensor Letters* 2. doi:10.1109/LSENS.2018.2825439.
- Han, S.C., Jekeli, C., Shum, C.K., 2004. Time-variable aliasing effects of ocean tides, atmosphere, and continental water mass on monthly mean GRACE gravity field. *Journal of Geophysical Research: Solid Earth* 109. doi:10.1029/2003JB002501. b04403.
- Harvey, N., 2016. GRACE star camera noise. *Advances in Space Research* 58, 408–414. doi:10.1016/j.asr.2016.04.025.
- Harvey, N., Dunn, C.E., Kruizinga, G.L., Young, L.E., 2017. Triggering Conditions for GRACE Ranging Measurement Signal-to-Noise Ratio Dips. *Journal of Spacecraft and Rockets* 54, 327–330. doi:10.2514/1.A33578.
- Heinzel, G., Rüdiger, A., Schilling, R., 2002. Spectrum and spectral density estimation by the Discrete Fourier Transform (DFT), including a comprehensive list of window functions and some new flat-top windows. Technical Report. Max-Planck-Institut für Gravitationsphysik, Leibniz University Hannover, Germany. URL: https://holometer.fnal.gov/GH_FFT.pdf.
- Heiskanen, Moritz, H., 1967. *Physical Geodesy*. Springer, Vienna. doi:10.1007/978-3-211-33545-1.
- Herman, J., Presti, D., Codazzi, A., Belle, C., 2004. Attitude Control for GRACE, in: 18th International Symposium on Space Flight Dynamics, p. 27. URL: <http://adsbit.harvard.edu/full/2004ESASP.548...27H/0000027.000.html>.
- Herman, J., Steinhoff, M., 2012. Balancing, turning and saving: Special AOCS operations to extend the GRACE mission, SpaceOps 2012, Stockholm Sweden. URL: <https://arc.aiaa.org/doi/pdf/10.2514/6.2012-1275114>.
- Hewitson, M., 2007. LTPDA - a MATLAB toolbox for accountable and reproducible data analysis. URL: <https://www.elisascience.org/ltpda/usermanual/help toc.html>.

- Horwath, M., Lemoine, J.M., Biancale, R., Bourgogne, S., 2011. Improved GRACE science results after adjustment of geometric biases in the Level-1B K-band ranging data. *Journal of Geodesy* 85, 23–38. doi:10.1007/s00190-010-0414-2.
- Hsu, C., Velicogna, I., 2017. Detection of sea level fingerprints derived from GRACE gravity data. *Geophysical Research Letters* 44, 8953–8961. doi:10.1002/2017GL074070.
- Hudson, D.G., 2003. In-Flight Characterization and Calibration of the SuperSTAR Accelerometer. Master Thesis. Center of Space Research, University of Texas, Austin.
- Inácio, P., Ditmar, P., Klees, R., Farahani, H.H., 2015. Analysis of star camera errors in GRACE data and their impact on monthly gravity field models. *Journal of Geodesy* 89, 551–571. doi:10.1007/s00190-015-0797-1.
- Jean, Y., Meyer, U., Arnold, D., Bentel, K., Jäggi, A., 2017. Effect of the improved accelerometer calibration method on AIUB's GRACE monthly gravity field solution, EGU, General Assembly, Vienna, University of Bern, Switzerland.
- Jekeli, C., 1999. The determination of gravitational potential differences from satellite-to-satellite tracking. *Celestial Mechanics and Dynamical Astronomy* 75, 85–101. doi:10.1023/A:1008313405488.
- Kanzow, T., Flechtner, F., Chave, A., Schmidt, R., Schwintzer, P., Send, U., 2005. Seasonal variation of ocean bottom pressure derived from Gravity Recovery and Climate Experiment (GRACE): Local validation and global patterns. *Journal of Geophysical Research* 110. doi:10.1029/2004JC002772.
- Kaula, W., 1967. Theory of statistical analysis of data distributed over a sphere. *Review in geophysics* 5. doi:10.1029/RG005i001p00083.
- Keshner, M., 1982. 1/f noise. *Proceedings of IEEE* 70, 212–218. doi:10.1109/PROC.1982.12282.
- Kim, J., 2000. Simulation study of a low-low satellite-to-satellite tracking mission. Ph.D. Thesis. Center of Space Research, University of

- Texas, Austin. URL: https://geodesy.geology.ohio-state.edu/course/refpapers/Kim_diss_GRACE_00.pdf.
- Kim, J., Tapley, B.D., 2002. Error analysis of a low-low satellite-to-satellite tracking mission. *Journal of Guidance, Control, and Dynamics*, AIAA 25, 100–1106. doi:10.2514/2.4989.
- Klinger, B., Mayer-Gürr, T., 2014. Combination of GRACE star camera and angular acceleration data: impact on monthly gravity field models, Institute of Theoretical Geodesy and Satellite Geodesy, TU Graz, Austria. GRACE Science Team Meeting, Potsdam, Germany.
- Klinger, B., Mayer-Gürr, T., 2016. The role of accelerometer data calibration within GRACE gravity field recovery: results from ITSG-2016. *Advances in Space Research* 58, 1597–1609. doi:10.1016/j.asr.2016.08.007.
- Klinger, B., Mayer-Gürr, T., Behzadpour, S., Ellmer, M., Kvas, A., Zehentner, N., 2016. The new ITSG-Grace2016 release, Institute of Theoretical and Satellite Geodesy, Graz University of Technology, Austria. European Geophysical Union, General Assembly, Vienna.
- Knudsen, P., Andersen, O., Khan, S.A., Høyer, J., 2001. Gravity, Geoid and Geodynamics, Springer, Berlin, Heidelberg. volume 123 of *International Association of Geodesy Symposia*. chapter Ocean tide effects on GRACE gravimetry, pp. 159–164. doi:10.1007/978-3-662-04827-6_27.
- Ko, U.D., 2008. Analysis of the characteristics of the GRACE dual one-way ranging system. Ph.D. Thesis. Center of Space Research, University of Texas, Austin. URL: <http://hdl.handle.net/2152/17977>.
- Ko, U.D., Eanes, R., 2015. Improvement of Earth Gravity Field maps after pre-processing upgrade of the GRACE satellite's star trackers. *Korean Journal of Remote Sensing* 2. URL: <http://advances.sciencemag.org/content/2/4/e1501693>.
- Ko, U.D., Tapley, B.D., Ries, J.C., Bettadpur, S.V., 2012. High-Frequency noise in the Gravity Recovery and Climate Experiment Intersatellite Ranging System. *Journal of Spacecraft and Rockets* 49, 1163–1173. doi:10.2514/1.A32141.

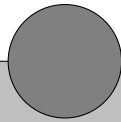
- Koch, K.R., 1990. Bayesian Inference with Geodetic Applications. volume 1. Springer, Berlin, Heidelberg. doi:10.1007/BFb0048699.
- Koch, K.R., Kusche, J., 2002. Regularization of geopotential determination from satellite data by variance components. *Journal of Geodesy* 76, 259–268. URL: <https://link.springer.com/article/10.1007/s00190-002-0245-x>.
- Kruizinga, G., 2004. GRACE Technical Note 03: Sequence of Events (SOE) format description. Report. Jet Propulsion Laboratory, NASA, US.
- Kuo, C.Y., Shum, C., yi Guo, J., Yi, Y., Braun, A., Fukumori, I., Matsumoto, K., Sato, T., Shibuya, K., 2008. Southern Ocean mass variation studies using GRACE and satellite altimetry. *Earth Planets Space* 60, 477–485. doi:10.1186/BF03352814.
- Landerer, F.W., Jungclauss, J.H., Marotzke, J., 2008. El Niño–Southern Oscillation signals in sea level, surface mass redistribution, and degree-two geoid coefficients. *Journal of Geophysical Research* 113, 2156–2202. doi:10.1029/2008JC004767.
- Liu, X., 2008. Global Gravity Field Recovery from satellite-to-satellite tracking data with the acceleration approach. Ph.D. Thesis. TU Delft, Netherlands.
- Mayer-Gürr, T., 2006. Gravitationsfeldbestimmung aus der Analyse kurzer Bahnbögen am Beispiel der Satellitenmissionen CHAMP und GRACE. Ph.D. Thesis. Institute of Theoretical Geodesy, Bonn Germany. URL: <http://hss.ulb.uni-bonn.de/2006/0904/0904.pdf>.
- Mayer-Gürr, T., 2007. ITG-Grace03s: The latest GRACE gravity field solution computed in bonn, Institute for Theoretical Geodesy, University of Bonn. Joint International GSTM and DFG SPP Symposia. URL: http://mt.dgfi.tum.de/typo3_mt/fileadmin/20071015-17-Potsdam/mo_1050_06_mayer.pdf.
- Mayer-Gürr, T., 2015. Insights in the deterministic and stochastic modeling of the GRACE observations, Leibniz University Hannover, Germany. Global gravity field from satellite-to-satellite tracking, Geo-q Autumn School, Bonn.
- Mayer-Gürr, T., Eicker, A., K.H. Ilk, 2006. ITG-GRACE02s: a GRACE gravity field derived from short arcs of the satellite's orbit URL:

- https://www.researchgate.net/publication/268341518_ITG-Grace02s_a_GRACE_gravity_field_derived_from_range_measurements_of_short_arcs.
- Mayer-Gürr, T., Zehentner, N., Klinger, B., Kvas, A., 2014. ITSG-Grace2014: a new GRACE gravity field release computed in Graz, Institute of Theoretical and Satellite Geodesy, Graz University of Technology, Austria. GRACE Science Team Meeting, GFZ Potsdam, Germany.
- Meyer, U., Jäggi, A., Jean, Y., Beutler, G., 2016. AIUB-RL02: an improved time-series of monthly gravity fields from GRACE data. *Geophysical Journal International* 205, 1196–1207. URL: <http://ieeexplore.ieee.org/stamp/stamp.jsp?arnumber=8189140>.
- Montenbruck, O., Gill, E., 2000. *Satellite Orbits*. Springer-Verlag Berlin Heidelberg. doi:10.1007/978-3-642-58351-3.
- Pail, R., 2004. GOCE quick look gravity field analysis: Treatment of gravity gradients defined in the gradiometer reference frame, Second International GOCE User Workshop, Frascati. European Space Agency, Noordwijk, The Netherlands.
- Pail, R., Goiginger, H., Schuh, W.D., Höck, E., Brockmann, J.M., Fecher, T., Gruber, T., Mayer-Gürr, T., Kusche, J., Jäggi, A., Rieser, D., 2010. Combined satellite gravity field model GOCO 01S derived from GOCE and GRACE. *Geophysical Research Letters* 37. doi:10.1029/2010GL044906.
- Peterseim, N., 2014. TWANGS High-Frequency Disturbing Signals in 10 Hz Accelerometer Data of the GRACE Satellites. Ph.D. Thesis. Ingenieur fakultät Bau Geo Umwelt (BGU), TU München, Germany. URL: <http://nbn-resolving.de/urn/resolver.pl?urn:nbn:de:bvb:91-diss-20140714-1197563-0-6>.
- Peterseim, N., Flury, J., Schlicht, A., 2012. Magnetic torquer induced disturbing signals within GRACE accelerometer data. *Advances in Space Research* 49, 1388–1394. doi:10.1016/j.asr.2012.02.013.
- Petit, G., Luzum, B., 2010. IERS Conventions. Technical Report 179. Paris- Central Bureau of IERS - Observatoire de Paris. Frankfurt am Main: Verlag des Bundesamts für Kartographie und Geodäsie. URL: <https://www.iers.org/IERS/EN/Publications/TechnicalNotes/tn13.html?nn=94912>.

- Press, W., Teukolsky, S., Vetterling, W., Flannery, B., 1992. Numerical Recipes in C. 2nd ed.. Cambridge University Press.
- Reigber, C., 1989. Theory of satellite geodesy and gravity field determination. volume 25. Lecture Notes in Earth Sciences, Springer, Berlin.
- Rodell, M., Famiglietti, J.S., 2002. The potential for satellite-based monitoring of groundwater storage changes using GRACE: the High Plains aquifer, Central US. *Journal of Hydrology* 263, 245–256. doi:10.1016/S0022-1694(02)00060-4.
- Rodell, M., Velicogna, I., Famiglietti, J.S., 2009. Satellite-based estimates of groundwater depletion in India. *Nature* 460, 999–1002. doi:10.1038/nature08238.
- Romans, L., 2003. Optimal combination of quaternions from mutiple star cameras. Technical Report. URL: ftp://podaac.jpl.nasa.gov/allData/grace/docs/quaternion_memo.pdf.
- Savcenko, R., Bosch, W., 2012. EOT11a - empirical ocean tide model from multi-mission satellite altimetry. DGFI Report 89. Deutsches Geodätisches Forschungsinstitut (DGFI). Alfons-Goppel-Str. 11, D-80539 München, Germany. URL: http://epic-reports.awi.de/36001/1/DGFI_Report_89.pdf.
- Seeber, G., 2003. Satellite Geodesy. 2nd ed., Walter de Gruyter, Berlin, NewYork.
- Sneeuw, N., 2000. A semi-analytical approach to Gravity field analysis from satellite observations. Ph.D. Thesis. Institut für Astronomische und Physikalische Geodäsie, TU Munich. URL: <https://mediatum.ub.tum.de/doc/601028/>.
- Stanton, R., Bettadpur, S., Dunn, C., Renner, K.P., Watkins, M., 1998. GRACE Science and Mission Requirement Document. Technical Report. URL: http://geodesy.geology.ohio-state.edu/course/refpapers/Grace_smr.pdf.
- Steitz, D.E., O'Donnel, F., Buis, A., Chandler, L., Baguio, M., Weber, V., 2002. GRACE Launch Kit. Technical Report. URL: https://www.jpl.nasa.gov/news/press_kits/gracelaunch.pdf.
- Tapley, B.D., Bettadpur, S., Watkins, M., Reigber, C., 2004a. The Gravity Recovery and Climate Experiment: Mission overview and early results. *Geophysical Research Letters* 31. doi:10.1029/2004GL019920.

- Tapley, B.D., Schutz, B., Born, G., 2004b. Statistical Orbit Determination. Springer. URL: http://www.ebook.de/de/product/15169756/bob_schutz_byron_tapley_george_h_born_statistical_orbit_determination.html.
- Thomas, J., 1999. An analysis of gravity field estimation based on intersatellite dual 1 way biased ranging. Technical Report 98-15. Jet Propulsion Laboratory. Pasadena, California.
- Touboul, P., Foulon, B., Rodrigues, M., Marque, J., 2004. In orbit nano-g measurements, lessons for future space missions. *Aerospace Science and Technology*, 431-441 doi:10.1016/j.ast.2004.01.006.
- Touboul, P., Foulon, B., Willemenot, E., 1999a. Electrostatic space accelerometers for present and future missions. *Acta Astronautica* 45, 605-617. doi:10.1016/S0094-5765(99)00132-0.
- Touboul, P., Willemenot, E., Foulon, B., Josselin, V., 1999b. Accelerometers for CHAMP, GRACE and GOCE space missions: synergy and evolution. *BOLLETTINO DI GEOFISICA TEORICA ED APPLICATA* 40, 321-327. URL: http://www3.ogs.trieste.it/bgta/pdf/bgta40.3.4_TOUBOUL.pdf.
- Wang, F., 2003. Study on center of mass calibration and K-band ranging system calibration of the GRACE mission. Ph.D. Thesis. Center for Space Research, University of Texas Austin, US.
- Wu, S.C., Kruizinga, G., Bertiger, W., 2006. Algorithm Theoretical Basis Document for GRACE Level-1B Data Processing V1.2. Technical Report 327-741. California Institute of Technology, Jet Propulsion Laboratory, Pasadena, US.
- Xianping, Q., Yanc-Yuanxi, 2005. Evaluation of CHAMP Satellite orbit with SLR measurements. *Geo-spatial information science* 8, 209-213. doi:10.1007/BF02826823.
- Xu, P., Qiang, L., Bian, X., Dong, P., Ju, P., Gao, W., Gong, X., Luo, Z., Shao, M., Tang, W., Wan, X., Lau, Y.K., 2015. A preliminary study of level 1A data processing of a low-low satellite to satellite tracking mission. *Journal of Geodesy and Geodynamics* 6, 333-343. doi:10.1016/j.geog.2015.07.005.

- Zehentner, N., 2016. Kinematic orbit positioning applying the raw observation approach to observe time variable gravity. Ph.D. Thesis. Graz University of Technology, Austria. doi:10.13140/RG.2.2.33916.33927.
- Zhang, Q., Schwarz, K.P., 1996. Estimating double difference GPS multipath under kinematic conditions. Position Location and Navigation Symposium , 285–291doi:10.1109/PLANS.1996.509090.



Curriculum Vitae

Personal Information

Name	Sujata Goswami
Date of Birth	16 July 1990
Place of Birth	Modinagar, India
Nationality	Indian

Educational Background

Ph.D. candidate at Institute of Geodesy, Faculty of Civil Engineering and Geodetic Science, Leibniz Universität Hannover, Germany	since October 2014
Master of Technology in Geomatics Engineering, Faculty of Civil Engineering, Indian Institute of Technology Roorkee, India	July 2012 – July 2014
Bachelor of Technology in Computer Science & Engineering, Uttar Pradesh Technical University (UPTU), Lucknow, India	July 2007 – July 2011
Senior Secondary School (12 th), CBSE Board, New Delhi, India	May 2007
Higher Secondary School (10 th), CBSE Board, New Delhi, India	May 2005
